Title
Reduced-Order Modeling of Mechanical Interactions Between Material Bodies

Author
Raisi Sofi, Ardalan

Publication Date
2021

Peer reviewed|Thesis/dissertation

Reduced-Order Modeling of Mechanical Interactions Between Material Bodies

By

ARDALAN RAISI SOFI
DISSERTATION

Submitted in partial satisfaction of the requirements for the degree of

DOCTOR OF PHILOSOPHY

in

Mechanical and Aerospace Engineering

in the

OFFICE OF GRADUATE STUDIES

of the

UNIVERSITY OF CALIFORNIA

DAVIS

Approved:

_____

Bahram Ravani, Chair

_____

Barbara Linke

_____

Masakazu Soshi

Committee in Charge

2021

Abstract

The material and geometric characteristics of every particle in a system of two or more particles affect the mechanical interaction between them and consequently affect the mechanical behavior of the entire system. The Finite Element Method (FEM) or the Discrete Element Method (DEM) are two popular strategies for numerical evaluation of the mechanical behavior of the system of particles. However, both of these numerical techniques are computationally expensive or can be difficult to implement in some practical applications. This dissertation utilizes methods from Deep Learning (DL) to extensively reduce the computational time of two different problems associated with mechanical interactions between similar and dissimilar particles. In the first problem, two different Convolutional Neural Network (CNN) models are used for the sub-second prediction of thermo-mechanical interaction between particles in powder beds used in Selective Laser Sintering (SLS) Additive Manufacturing (AM) process. In the second problem, an Artificial Neural Network (ANN) model is developed for the sub-second evaluation of the dynamic response of structures to the reaction force that arises during the collision of dissimilar material bodies.

Physical modeling of the transient temperature throughout the SLS manufacturing process is critical for determining the quality of Additively Manufactured structure (AM structure). Conventional numerical models for simulating the thermal field of AM structures, however, are time-consuming and cannot be easily applied to the development of a real-time simulation system. In this dissertation, a sophisticated existing conventional physics-based simulation is utilized to generate a dataset with thousands of two-dimensional (2D) position-time representations of the laser head with various process parameters and their associated heat-map of AM structures for DL training purposes. This dataset is used to train a deep encoder-decoder CNN model capable of sub-

second prediction of the heat-map of AM structure. It is shown that, on average, the proposed DL model is more than 41,000 times faster than the physics-based model.

The physical modeling of powder-based AM structures aims to relate the macroscopic effective mechanical properties of these structures quickly and accurately to their microscopic structural features. For DL training purposes, the DEM simulation is used to simulate powder particle interactions and evaluate macro-level elastic properties of hundreds of AM structures. In this dissertation, an accurate CNN model for predicting the effective elastic properties of SLS manufactured structures is introduced, with an average error of less than 4%. The sub-second level computational time of this CNN model may be viewed as a step toward in developing a real-time system capable of predicting the effective properties of powder beds.

A comprehensive understanding of the nonlinear compliance behavior of colliding bodies throughout the collision process is required to assess the dynamic behavior of many multi-body granular systems such as powder-based AM processes, pharmaceutical manufacturing processes, and mineral operations. However, the conventional numerical models for evaluating the nonlinear force-displacement behavior of dissimilar colliding material bodies often use time-consuming iterative algorithms, which may considerably slow down multi-body granular simulations with a high number of colliding material bodies. In this dissertation, a time-consuming nonlinear lumped parameter model based on the strain-hardening power law is utilized to create a dataset with thousands of force-displacement curves for colliding bodies with different material and geometrical properties and various relative impact velocities. The generated dataset is used to train an ANN model for sub-second prediction of force-displacement behavior of colliding material bodies during elastoplastic impact. The ANN model results in lowering the computational cost of multi-body dynamic analysis and granular flow simulations significantly.

Acknowledgments

I would first like to express my sincere gratitude to my advisor Professor Bahram Ravani for suggesting the topics of this dissertation and for his consistent support and guidance throughout this work. Without his wisdom, guidance, and insightful feedback, this work would not have been achievable. Not only did I benefit from his academic guidance throughout my Ph.D., but I also learned many real-life lessons from him, for which I am indebted.

I would like to thank Prof. Barbara Linke and Prof. Masakazu Soshi for their unwavering support throughout my Ph.D. program and for agreeing to serve on the dissertation committee. I would also like to acknowledge the opportunities and funding provided by the University of California-Davis during my graduate study at the Department of Mechanical and Aerospace Engineering.

There is no way to express how much it meant to me to have been a member of the Advanced Highway Maintenance and Construction Technology Research Center (AHMCT). I would like to thank all my friends and colleagues who inspired me over the many years and made our lab environment my second home.

Deepest thanks to my uncles Mehdi and Majid, who keep me grounded, remind me of what is important in life, and have been always supportive of my adventures. Finally, I would also like to thank my parents, whose constant love and support keep me motivated and confident. My accomplishments and success are because they have believed in me.

Table of Contents

List of Tables

List of Figures

Chapter 1. Introduction, Objective, and Contributions

1.1 Introduction and Background

This dissertation studies two different problems, both involving mechanical interactions between material particles. The first involves thermo-mechanical interactions between material particles in powder beds used in Additive Manufacturing (AM) processes, but the second problem only considers elastoplastic interactions of individual particle bodies in lumped parameter modeling of particle collisions used in dynamic analysis. Application of modern Deep Learning (DL) techniques is investigated in this dissertation to develop reduced-order predictive models of interactions of material particles both in powder beds used in AM as well as elastoplastic collision of material particles. The aim is to develop computationally more efficient models than physics-based models that can be used for real-time applications.

Additive Manufacturing has evolved into one of the most promising manufacturing technologies thanks to robust research and development in the past few decades. Unlike traditional subtractive manufacturing processes, AM works with the layer-by-layer transformation of materials into three-dimensional workpiece. As a result, AM processes do not necessarily require fixtures, cutting machines, or any other specialized tooling equipment. Powder Bed Fusion (PBF), in which a laser is used to melt and fuse micro-powders into the Additively Manufactured structure (AM structure), is one of the most popular AM techniques for manufacturing sophisticated metallic structures. Physical modeling of the thermomechanical behavior of the powder beds during the PBF process leads to a better understanding of the complex phenomena involved in the AM processes, and it allows for the characterization of the final product based on process parameters.

The two popular numerical methods for the thermomechanical analysis of powder beds in AM processes are the Finite Element Method (FEM) and the Discrete Element Method (DEM) [1]-[2]-[3]-[4]. However, due to the substantial computational costs of FEM and DEM numerical methods, a real-time process control system for the evaluation of the thermomechanical behavior of AM structures could not be directly developed from these numerical techniques. In this dissertation, alternative methods using DL techniques are considered for predicting the thermal field of AM structures and evaluating their aggregate elastic properties. A deep encoder-decoder Convolutional Neural Network (CNN) is developed and used to extract and encode sets of patterns from the laser trajectory (the position-time representation of the laser head) and decode them back to the heat-map of AM structure. Moreover, using a conventional CNN technique, the appropriate set of patterns are extracted from the pixelated AM structure by convolving a weighted filter across the whole structure. The subsequent layers of CNN then combine these features to detect higher-order features, and finally, the last fully connected (FC) layer at the end of the network is used to predict the elastic properties of aggregate. These combinations of the CNN techniques provide for a unique Machine Learning (ML) algorithm appropriate for thermomechanical interactions in solids and AM.

Non-thermal interactions occur between solid objects, for example, in inelastic collisions. In such impacts, kinetic energy is lost due to the permanent internal deformation of colliding bodies. This loss of kinetic energy leads to different normal force-displacement behavior of the contact region during indentation and restitution periods. In the majority of lumped parameter models of impact mechanics, the collision of dissimilar bodies is evaluated based on linear contact stiffness. In this dissertation, a strain-hardening nonlinear constitutive relation is developed for the lumped parameter modeling of such inelastic impacts of dissimilar bodies (results are published here [5]).

This mechanistic modeling technique results in closed-form expressions for the work done by contact force on colliding bodies during compression and restitution phases. Obtaining the compliance curve using this modeling technique requires the use of a numerical scheme such as the Newton-Raphson iterative algorithm. However, putting this algorithm into practice is time-consuming, especially for large-scale granular flow simulations. This dissertation utilizes methods from DL to train a novel Artificial Neural Network (ANN) model capable of sub-second prediction of compliance curve of colliding bodies during inelastic impact given the relative impact velocity and material properties of both colliding bodies, including their strain-hardening coefficients. The resulting sub-second level computational time for evaluation of the force-displacement behavior of the inelastic impact of dissimilar bodies could drastically reduce the computational cost of rigid body dynamic analysis codes and granular flow simulations.

1.2 Areas of Coverage and Scope

The material and geometric properties of every particle in a system of two or more particles affect the mechanical interaction between particles and consequently affect the thermomechanical behavior of the entire system. Using traditional computational methods to evaluate the thermomechanical behavior of these discrete structures is time-consuming, expensive, and it may not provide a sub-second prediction of the effective properties of the system. Data-driven Artificial Intelligence (AI) techniques such as ML and DL are powerful tools to reduce the computational time of the traditional methods. This dissertation is organized into six chapters. Chapter 1 (current chapter) introduces the problems explored in this dissertation and presents a comprehensive literature review and gap analysis on these problems. In Chapter 2, the literature on the uses of ML and DL methods for mechanical design and manufacturing is extensively reviewed. In the following three chapters, the use of ML and DL methods in three different problems associated

with mechanical interaction between similar and dissimilar bodies are studied.

The aim of Chapter 3 is to reduce the computational time of the physics-based simulations of the thermal field of powder beds during the Selective Laser Sintering (SLS) manufacturing process. In Chapter 3, a time-consuming physics-based simulation is used to create a dataset for training a DL model capable of sub-second prediction of the thermal field of powder beds in AM processes. In Chapter 4, the discrete force-displacement model of powder-based AM structures is used to evaluate the macro-level continuum-mechanical state variables. Furthermore, the effective macro-level elastic properties of the aggregate of AM structures are estimated using a conventional numerical model. The developed model is then used to create a dataset including hundreds of AM structures with their corresponding elastic properties. Using the created dataset, a CNN model is trained to predict the effective elastic properties of the aggregate in a fraction of the time needed compared to the conventional numerical methods. The Deep Learning models developed for chapters 3 and 4 could be used for the real-time optimization of process parameters during the SLS manufacturing process. In Chapter 5, a DL model is developed, which is capable of sub-second prediction of the force-displacement behavior of colliding bodies during inelastic impact. The lower computing cost of the proposed model relative to the traditional numerical method would be beneficial for granular flow simulations with a large number of particles. The final chapter (Chapter 6) includes the conclusions of the works done in this dissertation and recommendations for future works.

1.3 Literature Review and Gap Analysis

1.3.1 Prediction of the Thermomechanical Behavior of Powder Beds

Prediction of the thermomechanical behavior of powder beds during the AM process is vital for determining the quality and structural integrity of AM structures. Manufacturing process

parameters (scanning strategy, scanning speed, laser power, etc.) have a significant impact on the effective properties of the final product; therefore, optimization of the process parameters is essential for the manufacturing of high-quality parts. The process parameters of subtractive manufacturing methods have been widely researched and optimized in the past. In the case of AM, however, optimization of process parameters has just been recently begun [6]. The relationship between process parameters and mechanical characteristics of AM structures has been investigated experimentally in several research studies. For example, Levkulich *et al.* [7] experimentally studied the relationship between manufacturing process parameters such as substrate overhang, laser power, and scanning speed with residual stress formation in the Laser PBF (L-PBF) manufacturing process. Kumar *et al.* [8] looked into how component orientation and laser power affected the geometrical precision and hardness of AM structures made using the SLS manufacturing process by performing numerous experiments. Heigel and Lane [9] discovered that the length of the melt pool has a direct relationship with laser intensity using an advanced experimental setup for high-speed temperature monitoring of powder-based AM processes. Criales *et al.* [10] used an in-situ thermal camera to investigate the size of the melt pool and heating rates during the AM processing of nickel alloy powders, demonstrating that the melt pool has a variable geometry as the laser scans through the metal powders. The experimental investigation of AM processes is costly and time-consuming, making them relatively impractical for generating large datasets that are needed is for neural network training. Experimental results, however, can be used to validate numerical and simulation models, which can then be used to generate large datasets for neural network training.

In recent years, the FEM numerical methods have been commonly used to numerically model and analyze the thermomechanical behavior of powder beds as a continuum configuration

to analyze their structural properties and temperature distribution. Yang *et al.* [11] used the SIMULIA AM Scenario App, based on Abaqus finite element solver to investigate the residual elastic strain formation in a cantilever structure with a large finite element size and they verified their numerical results with X-ray diffraction experimental data. Singh and Srinivasa [12] developed a FEM model to estimate temperature and density distribution in a single layer of powder and optimized the manufacturing process parameters to achieve the desired density. Fu *et al*. [1] created a heat transfer FEM model to investigate the influence of laser power and scanning speed on the absorption mechanism of powders during the PBF process. Fu *et al.* discovered that the instantaneous absorption drops more significantly with increasing laser power at a high scanning velocity than at a low velocity. Liu *et al.* [2] proposed a linear "Tri-Prism" FEM model for heat transfer analysis of the Selective Electron Beam Melting (SEBM) manufacturing process and demonstrate that the temperature gradient is significantly reduced as the melting phase of metal powder begins during the SEBM process. All continuum models of the powder-based AM structures described above used FEM with relatively large meshes, resulting in low computational costs. The continuum models with large mesh, unfortunately, are not accurate enough for simulation of the thermomechanical behavior of powder-based AM processes at the microscale. Yang *et al.* [13] investigated the relationship between the microstructure of SLS manufactured parts and AM process parameters using the Multiphysics Object-Oriented Simulation Environment (MOOSE) using FEM simulation. In order to improve the accuracy of the finite element model, Yang *et al.* used a small finite element mesh, but the analysis domain was kept small, and an adaptive meshing method was used to cut down on computational costs.

The material and geometrical properties of all particles within the manufacturing domain play a significant role in the fabrication of AM structures with outstanding mechanical properties

using PBF techniques. Hence, a particle-based numerical simulation tool that accounts for inter-particle forces and interactions is needed to accurately evaluate the thermomechanical behavior of the powder beds during the AM process [14]. The Discrete Element Method is the most well-known particle-level numerical method for investigating powder particle interactions during AM process [15]. Depending on the goal of the DEM simulation of AM process, various constitutive behaviors such as collision models, heat transfer models, the ability to form or break inter-particle bonds, and the ability to respond to external fields might be considered between existing particles in the analysis domain [3]. In this thesis, the DEM is used to investigate the SLS manufacturing process, in which particles are heated to the point that they are fused together but not melted.

Xin *et al.* [16] investigated the scattering phenomenon of the laser beam on polymer powder beds during the SLS manufacturing process using a hybrid of the Monte Carlo method and DEM simulation. Using both FEM and DEM methods, Xin *et al.* modeled the energy distribution during the AM process and found that DEM is more accurate than FEM for simulating the thermal history of powder beds. Haeri *et al.* [17] investigated the influence of powder bed thickness and the translational velocity of powder spreading devices on the surface roughness of the final products using DEM simulations. Moser *et al.* [5] studied the impact of some modeling parameters on the effective thermal conductivity of powder beds using a DEM heat transfer model. Moser *et al.* found that gas and temperature conductivity have a significant impact on the effective thermal conductivity of powder beds. Gobal and Ravani [18]-[4] established a dynamic coupling algorithm that moves the simulation between coarse elements and particle-level elements to reduce the computational costs of the thermal field simulation during the SLS manufacturing phase while still taking advantage of the microstructure accuracy of the particle-level models. The DEM may also be used to analyze the elasticity of continuous structures. Gao *et al.* [19], for example, used DEM

to simulate a continuous structure by converting it to a non-continuum discrete form.

Data-driven AI techniques have shown to be highly effective in conducting complex regression for various aspects of AM, including quality control, process parameter optimization, and defect detection [20]-[21]. Many studies have been conducted over the last decade to enhance the defect detection and classification performance in AM process control systems by coupling different neural network architectures with computer-vision hardware. Zhang *et al.* [22] designed a CNN-based porosity monitoring system for the direct laser deposition of metallic powders using coaxial image data obtained by high-speed cameras under various laser powers and scanning speed. Scime *et al.* [23] developed a Dynamic Segmentation CNN (DSCNN) model for the real-time anomaly classification during the PBF manufacturing process. Yuan *et al.* [24] developed a monitoring framework and successfully implemented semi-supervised CNNs for SLM in-situ monitoring, which included data collection, partial data labeling, model training, and verification. During the L-PBF manufacturing process, interactions between the re-coater blade and the powder bed may result in re-coater hopping, super-elevation defects, and other issues. Using the transfer learning method, Scime and Beuth [25] retrained the already developed AlexNet CNN architecture to enhance the detection process of mentioned spreading anomalies.

In addition to the application of the ML technique in computer-vision problems for AM, there has been little work in the application of ML to predict the thermal behavior of AM structures. For the powder-based AM processes with a wide range of process parameters, Mozaffar *et al.* [26] suggested a stacked Recurrent Neural Network (RNN) structure for the thermal analysis of powder beds. Paul *et al.* [27] used the FEM simulation dataset to train an ensemble of bagged decision trees as the regression algorithm to predict the temperature field of the melt pool in AM process. There does not seem to exist any particle-level simulation of powder-based AM structure combined

with DL algorithms capable of predicting the heat-map of powder beds at any stage of the manufacturing process or capable of evaluating the effective elastic properties of AM structures. This is the problem related to powder beds in AM that is addressed in this dissertation.

1.3.2 Inelastic Impact of Dissimilar Bodies

Developing an analytical solution that can precisely describe the dynamic response of structures to the reaction force that arises during the collision of dissimilar bodies is challenging due to the complexity in the mathematical modeling of plastic deformations. Many researchers have used theoretical, computational, and experimental approaches to investigate collisions between deformable structures. The mechanical behavior of colliding bodies and kinetic energy dissipation during elastic-plastic impact has been extensively studied by neglecting the inertial effects. Du *et al.* [28] developed a theoretical model for the dynamical pattern of elastoplastic normal impact of two spherical bodies with low relative impact velocity. Big-Alabo [29] investigated the compliance response of spherical colliding bodies during normal elastic and elastoplastic impact using the Force Indentation Linearization Method (FILM). Wu *et al.* [30] investigated the influence of plastic deformation on the rebound behavior of spheres colliding against half-space using FEM numerical solution. The impact modeling of colliding bodies with identical yield stresses can be simplified by ignoring inertial effects; Such models, however, would not be effective in simulating the collision of two dissimilar bodies with significantly different yield stresses.

There have been limited studies on the modeling and analysis of collision between dissimilar bodies (with different material and geometrical properties). In addition, most of the available studies in the literature in this area are limited to some particular collision scenarios. Mesarovic *et al.* [31] established the force-displacement relationship for the impact of two

spherical colliding bodies with strain-hardening material, where the material properties of the colliding bodies are different except for their identical hardening coefficient. Based on elastoplasticity theory, Vu-Quoc and Zhang [32] - [33] studied the collision between spherical colliding bodies and developed a displacement-driven and a force-driven numerical model for their normal force-displacement behavior. Big-Alabo [34] developed a relatively simple theoretical model of the collision for the elastoplastic impact of two dissimilar spheres using the equivalent impact system approach.

One of the most fundamental input parameters to the granular flow and multi-body dynamic simulations is the coefficient of restitution (COR). In its classical one-dimensional form for either collinear or frictionless impact configuration, the kinematic COR can be defined as the ratio of the relative impact velocity after the collision to the relative impact velocity before the collision [35]-[36]. Moreover, the energetic definition of the COR depends on the work done by the normal component of contact force on both colliding bodies. Thornton *et al.* [37] used a partially latching spring model to calculate the COR and study the plastic behavior of a spherical body colliding obliquely against a target wall, taking into account both normal and tangential contact forces. Using a system of linear springs based on the Hertzian theory of contact, Coaplen *et al.* [38] (see also Stronge and Ravani [39]) proposed an energetic COR, which represents the energy dissipated during the inelastic impact of dissimilar colliding bodies. Stronge, Sofi, and Ravani [36] extend the previous work of Coaplen *et al.* by developing the nonlinear analytical equations for the work during indentation and restitution of colliding bodies using strain-hardening power-laws and used the resulting nonlinear equations to compute the energetic COR. Their analytical method might be used to model the inelastic collision between dissimilar bodies considering situations when impact energy causes at least one of the colliding bodies to be

compressed beyond its yield stress while the other colliding body could remain in the elastic region. Furthermore, using the Newton-Raphson iterative method, Stronge, Sofi, and Ravani [36] proposed a piecewise nonlinear lumped parameter model to estimate the compliance curve (the normal force-displacement curve) numerically for the inelastic collinear collisions of dissimilar bodies. However, implementation of this iterative algorithm is a time-consuming process; Therefore, using this algorithm in multi-body dynamics codes could significantly raise the computational costs. There does not seem to exist any published research on using ML or DL algorithms to approximate the normal force-displacement behavior in inelastic collisions between dissimilar bodies made of strain-hardening material. Multi-body dynamic analysis codes and granular flow simulations could be benefited from training an ANN model capable of sub-second prediction of the compliance curve of the colliding bodies during inelastic impact. This is another problem that is addressed in this dissertation.

Chapter 2. Machine Learning and Deep Learning for Design and Manufacturing

The field of mechanical design and manufacturing is at a historic transition point. The increase in computational power, improvements in physics-based simulations, and access to advanced industrial sensors allow engineers to collect a massive amount of data [40]. This obtained data from the manufacturing processes and physics-based simulations provides a useful medium for learning about complicated phenomena associated with manufacturing processes and enabling engineers to achieve optimal designs. However, the implementation of traditional statistical methods to extract meaningful information from big data could be extremely time-consuming or even impossible since they require a deep understating of input modeling parameters. Many ML and DL models, on the other hand, are capable of performing complex predictions without having interpretable input parameters.

ML and DL methods can revolutionize mechanical design by detecting trends in design data, identifying the optimum design, developing physics-based surrogate models, and introducing a higher level of autonomy to mechanical design [41]-[42]-[43]. The design and modeling of a complex engineering system with traditional statistical design techniques might be challenging due to high-dimensional input parameters and complex physical constraints. On the other hand, for a sufficiently large dataset, an ML or DL algorithm may be successfully trained on high-dimensional design data to identify regularities in the dataset and generalize them to previously unseen data from the same distribution.

2.1 Machine Learning Methods

One of the most important steps toward implementing ML and DL algorithms for

mechanical design and manufacturing problems is choosing the suitable ML algorithm based on the characteristics of the dataset, necessary speed, and required precision of the final model. In general, ML and DL methods can be categorized into supervised learning, unsupervised learning, semi-supervised learning, imitation learning, and reinforcement learning [4]. Figure 1 shows different types of ML and DL techniques used in the field of mechanical design and manufacturing. In this section, the main idea of the application of these techniques in mechanical design and manufacturing is briefly discussed.

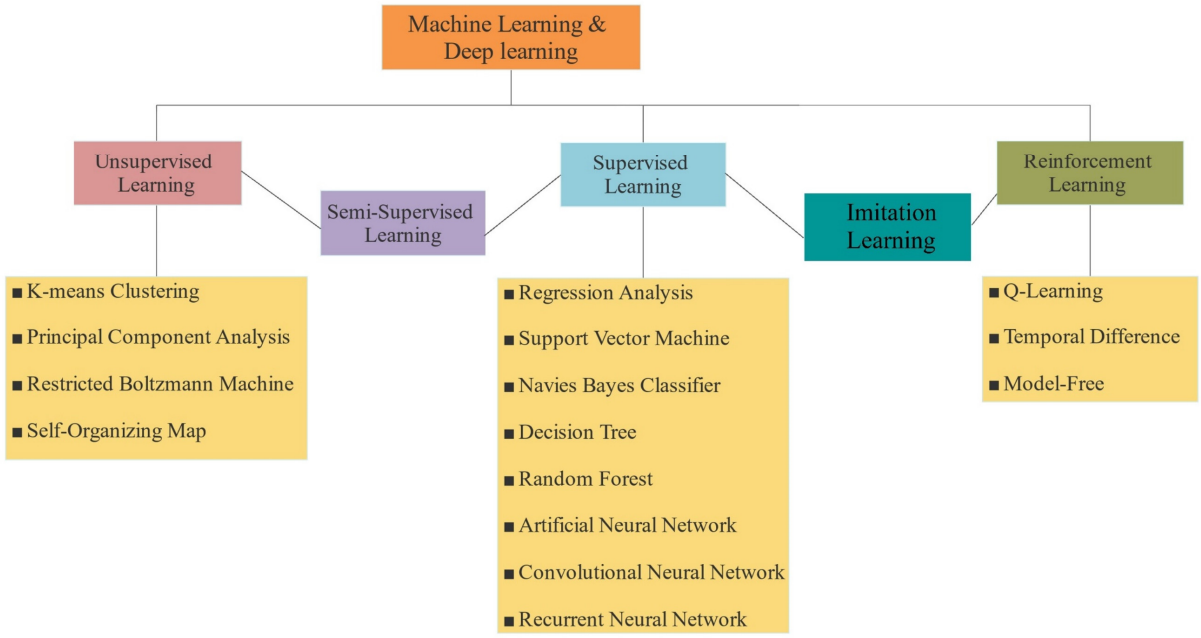

Figure 1: Different types of ML and DL methods used in mechanical design and manufacturing.

2.1.1 Supervised learning

Supervised learning involves generating a mapping relationship between a series of known input variables X and output variables Y and using the generated mapping function to approximate the outputs for unseen input data [45]. Figure 2 illustrates the supervised learning process for the classification problem, where the supervisor labels the training data, and the algorithm learns from this labeled data and tries to categorize the unseen data into the right group.

Generally, when engineers are trying to implement ML and DL algorithms to automate the design process or develop a reduced-order manufacturing process model, they usually deal with a supervised learning problem. These models are data-hungry, and their precision and accuracy are heavily dependent on the amount of available labeled data, which can be challenging to obtain in many situations due to costly laboratory experiments or time-consuming computational models. Supervised learning methods such as regression, Support Vector Machine (SVM), Navies Bayes classification, Decision Tree, Random Forest, ANN, CNN, and RNN have shown to be highly effective at performing complex regression and classification in the area of mechanical design and manufacturing.

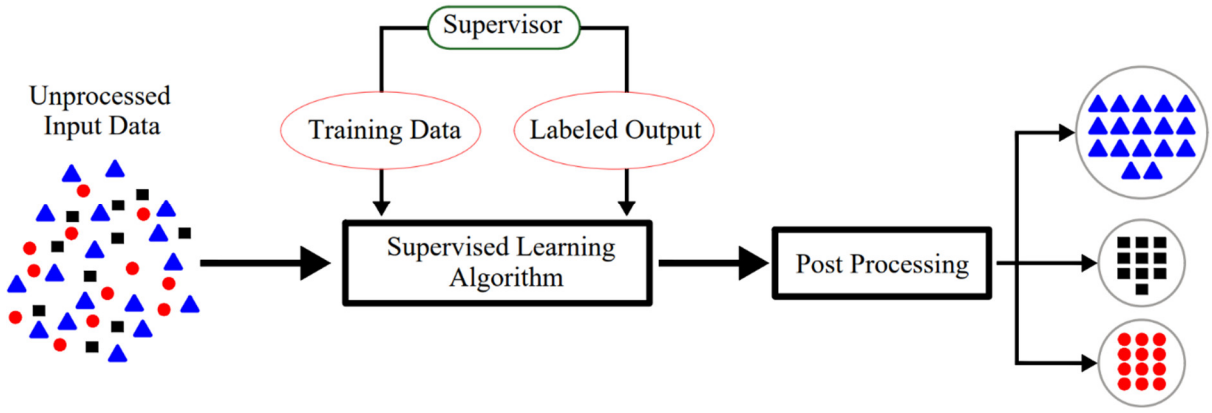

Figure 2: Schematic depicting the supervised learning process for the classification task.

2.1.1.1 Regression Analysis

Regression analysis is one of the oldest predictive techniques for analyzing the relationship between response variables and predictors. The regression analysis creates an equation to map the independent (input) variables to dependent (output) variables. The most basic and widely used supervised ML algorithms are linear regression and logistic regression. Jiang *et al*. [46] developed a logistic regression predictive model to study the visual detectability of fiber and delamination damages in composite structures that had been exposed to low-speed impact. In Additive

Manufacturing, Baturynska and Martinsen [47]-[48] used linear regression and nonlinear statistical models like multilayer perceptron for the estimation of dimensional features of the AM structure. They demonstrated that a simple linear regression model is more accurate than a complex multilayer perceptron for predicting some specific dimensional features.

2.1.1.2 Support Vector Machine (SVM)

The SVM algorithm aims to find a decision boundary in an N-dimensional feature space that has much lower dimensionality compared to the input features. SVM is one of the most used supervised learning techniques for classification and regression. Based on experimental data, Sivaprakash *et al.* [49] developed an SVM system to approximate the heat transfer rate in a shell and tube heat exchanger. Aoyagi [50] demonstrated a method for generating AM process maps using an SVM model. Aoyagi's SVM model could be used to optimize process parameters to fabricate AM structures with low pore density.

2.1.1.3 Navies Bayes classifier

Bayesian networks are a type of probabilistic graphical approach in which a directed graph is used to represent a set of variables and their dependencies. In both supervised and unsupervised settings, Bayesian networks can be trained for a wide variety of tasks, including prediction, decision making, and anomaly detection [51]. The Naive Bayes probabilistic classifier is a Bayesian network with a specific graph structure, which assumes that predictors are independent. Since each node represents an independent variable, Bayesian models are more interpretable than classical neural networks. Moreover, the independence of variables would make it possible to integrate prior knowledge into the Bayesian networks by specifying special probability distributions for each node. Correa *et al.* [52] used the Navies Bayes classifier to predict surface roughness in high-speed machining.

2.1.1.4 Decision Tree and Random Forest

Decision tree models, unlike logistic regression, are inherently nonlinear because they gradually split the feature space along with the input features. Decision tree approaches are generally faster than neural network models because they disregard the less important input features. Tucker and Kim [53] significantly reduced product development time and cost by optimizing the product design using the decision tree algorithm with varying attributes.

The Random forest (RF), originally introduced by Breiman [54], is a supervised learning system for regression and classification problems in which multiple decision tree classifiers are fitted to sub-samples of the dataset. Dasari *et al.* [55] used the Random Forests supervised learning approach to construct a surrogate turbine rear structure model. In their work, Dasari *et al.* extract if-then rules from the trained random forest model to gain a deep understanding of the design parameters. Wu *et al.* [56] developed a Random Forests model to predict the surface roughness of AM structure in the fused deposition manufacturing process.

2.1.1.5 Artificial Neural Network (ANN)

Neural network architectures, including ANN, CNN, and RNN, could be trained under supervised and unsupervised learning paradigms. However, since the majority of successful neural network models in the field of mechanical design and manufacturing are trained using supervised learning methods, they are listed under the supervised learning methods in this dissertation. Nearly all engineering applications, including aerospace, automotive, electronic, mechanical design, and manufacturing, have recently adopted ANN as a fast and powerful mathematical modeling technique for the optimization of engineering systems. Artificial Neural Networks are composed of several layers of neurons (nodes). In these networks, each neuron receives several inputs and computes their linear combination with a trainable weight parameter before passing the result to a

nonlinear activation function. Figure 3 demonstrates the general ANN architecture where each circle shows a single perceptron that calculates the weighted sum of all input features and passes it through a nonlinear activation function.

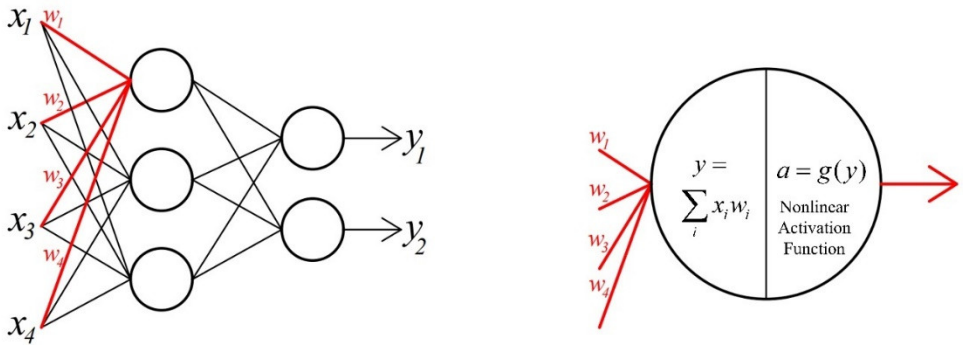

Figure 3: Representation of a shallow ANN (left) and a single perceptron unit (right).

Based on existing research data, Shi *et al.* [57] trained a highly accurate ANN model for compressive, flexural, and tensile strength estimation in Engineered Cementitious Composite (ECC). Chowdhury and Anand [58] developed an ANN model to investigate the impact of manufacturing process parameters on the thermal deformation of AM structures during SLS manufacturing. For Artificial Neural Network training, Chowdhury and Anand used ANSYS to model Ti6Al4V powder thermo-mechanical behavior under various process parameters.

2.1.1.6 Convolutional Neural Network (CNN)

The CNN technique introduced by Lecun *et al.* [59]-[60] has demonstrated outstanding performance in computer vision tasks such as image segmentation, image-to-image conversion, and object recognition [61]-[62]-[63]. Local and global patterns can be extracted from 2D or 3D arrays of numbers through convolutional layers in CNN architectures, and the unknown parameters of the network (weights and biases) can be optimized using the backpropagation algorithm. Scime *et al.* [23] developed a Dynamic Segmentation CNN (DSCNN) model for the real-time anomaly classification during the powder-based AM process. Zhang *et al.* [22] developed a CNN-based

porosity control method for direct laser deposition of metallic powders based on image data obtained by high-speed digital cameras under various process parameters. Based on a large dataset created by finite element simulations, Messner [64] developed a CNN-based surrogate model to evaluate the effective mechanical properties of periodic composites structures.

2.1.1.7 Recurrent Neural Network (RNN)

RNNs are neural networks that can efficiently be trained on time-series and sequential data. RNN algorithms are used for a variety of problems, including Natural Language Processing (NLP), speech recognition, rhythm learning, and time series anomaly detection. The Recurrent Neural Network methods, unlike conventional neural network algorithms such as ANN and simple CNN, maintains an internal state (memory) from one time step to the next. RNNs provide a much better interpretation of a sequence than other learning algorithms because of the existence of the mentioned internal state. Figure 4 shows the standard architecture of RNN, which consists of hidden layers and recursive input and output data; The gray arrows represent the internal state that passes from one time step to the next.

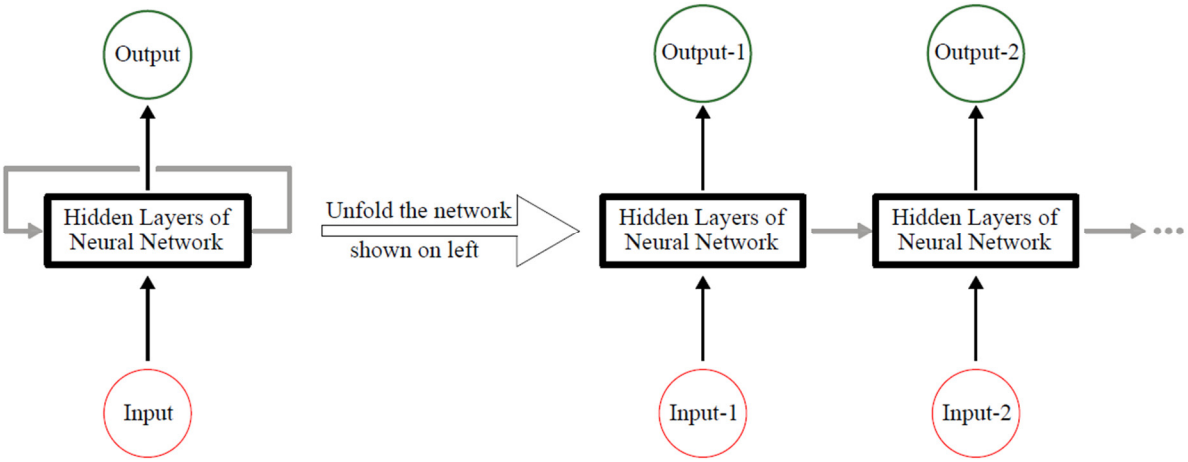

Figure 4: Representation of RNN in folded form (left) and unfolded form (right).

To develop a systematic repair and replacement strategy for the air compressors of heavy-

duty vehicles, Chen *et al.* [65] trained an RNN model capable of predicting the potential problems in close proximity to a failure using Logged Vehicles Data and Volvo Service Records from Volvo approved workshops. Wu *et al.* [66] designed an RNN based on Gated Recurrent Unit (GRU) to predict the evolution stress-strain state of mesoscale composite Representative Volume Element (RVE) subjected to random loading paths. Mozaffar *et al.* [26] developed a highly accurate RNN model to predict the thermal behavior of AM structures manufactured using the directed energy deposition technique.

2.1.2 Unsupervised Learning

The cost of labeling the training data is a major issue in supervised learning algorithms. Unsupervised ML methods, unlike supervised learning, do not rely on human intelligence to label the target output [67]. Without the existence of labeled training data or any other external guidance, unsupervised learning methods could recognize hidden patterns in the given dataset.

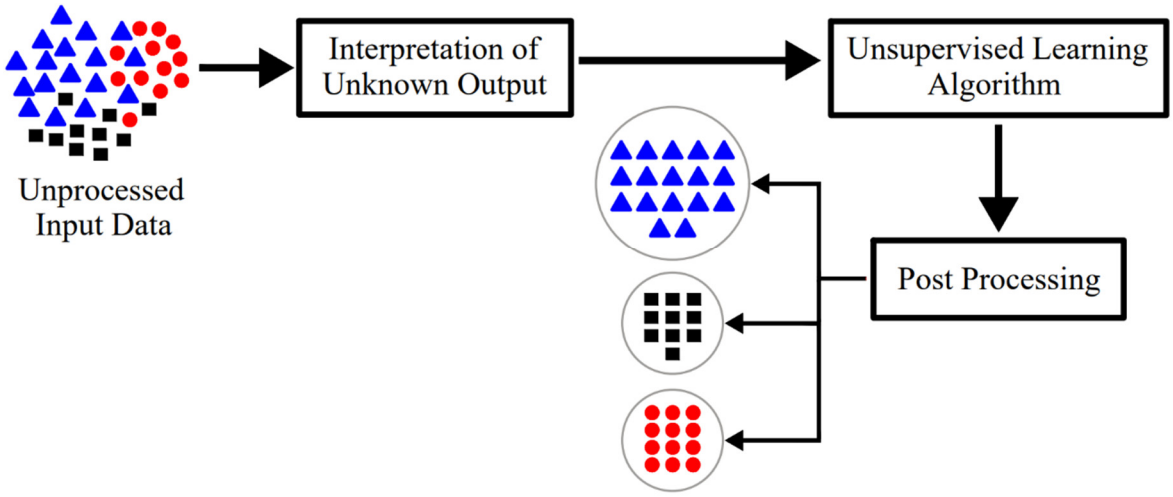

Figure 5: Schematic depicting the unsupervised learning process for clustering task.

Clustering is one of the most common applications of unsupervised learning algorithms, in which the algorithm attempts to classify inherent groupings within the unlabeled data and then assigns a label to each data point. Figure 5 demonstrates the general unsupervised learning process for a

clustering task where the data is classified without human supervision. K-means clustering, Principal Component Analysis (PCA), Restricted Boltzmann Machine (RBM), and Self-Organizing Map (SOM) are the four most popular unsupervised learning methods used in design and manufacturing.

2.1.2.1 K-means clustering

Clustering has seen widespread use in mechanical design and manufacturing as a common method for identifying groups or clusters in multivariate unlabeled input data. For separating observations into a set of k clusters, K-means clustering is one of the simplest and most commonly used clustering algorithms. In order to assign each observation to one cluster, the K-mean algorithm begins by selecting K cluster centers, either randomly or heuristically. The algorithm then calculates the Euclidean distance between each point and the centroid and assigns each data point to the cluster with the shortest distance. Finally, the algorithm computes the mean of each cluster and uses it as the new centroid [68]. The last two steps of the K-means clustering algorithm are repeated until convergence is achieved. Donegan *et al*. [69] proposed a method for generating zoned maps of AM process history for location-specific process control using K-means clustering and the thermal history of metal AM structures. Using K-means clustering and topic modeling techniques, Sabbagh *et al*. [70] created a hybrid clustering scheme to group manufacturing suppliers into clusters based on their capabilities. Moreover, Khanzadeh [71] trained a Self-Organizing Map unsupervised learning model to determine the geometrical accuracy of AM structure. Khanzadeh also trained a K-mean clustering model to validate the efficiency of their proposed model.

2.1.2.2 Principal Component Analysis (PCA)

Principal Component Analysis is an unsupervised learning technique for reducing data

dimensionality while preserving most of the variance [72]. The Principal Component Analysis decreases the dimensionality of data by locating the highest variance directions in high-dimensional data and map them into a new subspace of the same or lower dimensions. Xe *et al*. [73] proposed a microstructural design technique based on the PCA learning method to achieve optimum physical performance for heterogeneous materials. Hong and Shen [74] used a combination of Residual Force Vector (RFV) and PCA to train an effective Neural Network for detecting the location and severity of structural damage in real-time. This hybrid approach enhanced the damage detection accuracy of the neural network as well as its training speed. Heidari and Ohadi [75] used PCA to reduce the dimensionality of wavelet coefficient statistical parameters, then used the extracted features to train a neural network for gearbox fault diagnosis.

2.1.2.3 Restricted Boltzmann Machine (RBM)

Restricted Boltzmann Machine is a generative two-layer neural network that is bidirectional and partially controlled by randomness. Restricted Boltzmann Machine models are restricted because no two nodes in the same layer share a connection. Restricted Boltzmann Machine networks aim to maximize the log-likelihood function of the marginal distribution of input data [76]. It must be noted that reconstruction error always exists even if the input data distribution is almost identical to the distribution learned by RBM models. In a conventional neural network model, the output of each neuron is computed by passing the result of the dot product of weights and the output of the previous layer into a nonlinear activation function. Instead of subjecting the result of the mentioned dot product to a nonlinear activation function to compute the output of each neuron in hidden layers, the RBM computes the probability that the hidden neuron would have the value of one. The contrastive divergence learning method that is commonly used to train RBMs is different from the conventional neural networks training process via

stochastic gradient descent (SGD). This learning method is built on a short Markov chain that starts at the last example and approximates the graphical slope describing the relationship between the weights of the network and its error. Ye *et al*. [77] trainan RBM model for in situ monitoring of melted states during the SLM process using the plume and spatter signatures obtained during the AM process. Ye *et al*.'s approach is more accurate and requires less signal preprocessing than most other learning approaches. Wang *et al*. [78] developed a new approach for identifying bearing defects by using resampled vibration signals as feature vectors to describe different types of bearing faults and trained an RBM classifier model using these feature vectors.

2.1.2.4 Self-Organizing Map (SOM)

Professor Teuvo Kohonen established the SOM in the 1980s as an unsupervised learning tool for data visualization and dimensionality reduction [79]. Self-Organizing Map converts nonlinear mathematical relationships from high-dimensional data into low-dimensional data while preserving the essential topological relationships among the input data components. Rather than using error reduction algorithms like SGD, the SOM unsupervised learning approach employs a competitive learning mechanism in which nodes fight for the right to answer a subset of the input data. Gan *et al*. [80] trained a SOM model based on multiphysics modeling and experimental results to visualize the linkage of the process–structure–properties (PSPs) during AM production of nickel-based super-alloys and to evaluate the relationships between manufacturing processes parameters. Khanzadeh *et al*. [71] used SOM to describe the geometrical precision of AM structure manufactured with the Fused Filament Fabrication (FFF) process and identified types of geometric deviations that exist in manufactured parts. Huang *et al*. [81] used a SOM model to test a new bearing life deterioration measure based on vibration signals. Furthermore, these degradation indicators were used to train an ANN model for predicting ball-bearing residual life.

2.1.3 Semi-Supervised Learning

Semi-supervised learning algorithms fall somewhere between supervised and unsupervised learning algorithms. The main goal of this learning paradigm is to enhance the supervised learning process using a massive number of unlabeled data available in the given dataset when there is a shortage of labeled data, and the labeling process is expensive, time-consuming, and complicated [82]. The presence of the mentioned limited number of labeled data makes semi-supervised learning methods more accurate than unsupervised learning methods. Generally, the semi-supervised learning process begins with a supervised model trained on available labeled data and then using that model to label the unlabeled data available in the given dataset. The newly labeled data from the supervised learning model and originally labeled data would be merged to create a more comprehensive dataset that could be used to train the final network of the semi-supervised learning process (see Figure 6) [83]. In this fashion, both the informative and predictive aspects of supervised and unsupervised learning were used to create an accurate learning model.

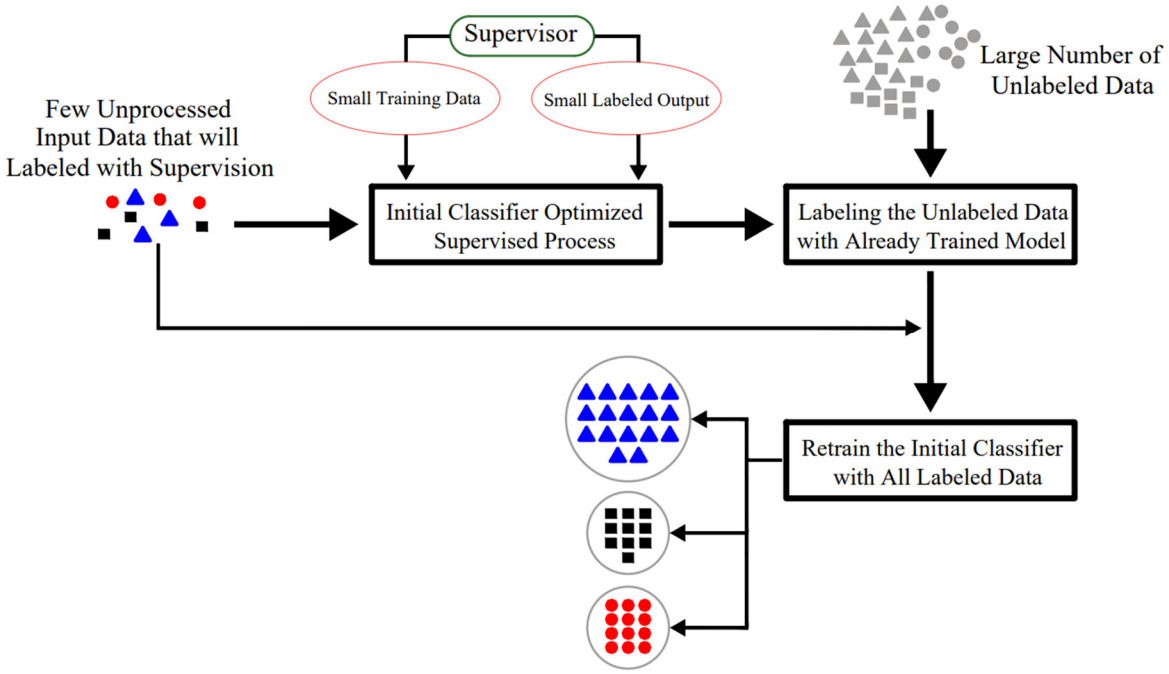

Figure 6: Schematic depicting the semi-supervised learning process for classification.

Guo *et al*. [84] used limited experimental data to train a semi-supervised DL classifier to evaluate the manufacturability of cellular structure with the L-PBF process and classify the failures during AM process, given the manufacturing process parameters. Verstraete *et al.* [85] proposed a semi-supervised generative adversarial network (GAN) to expand the manufacturing data size, and therefore, enhance the clustering results of the fault diagnosis of rolling element bearings. Guo and Buehler [86] used a semi-supervised learning method to train a graph neural network (GNN) to design the structural topology of architected materials with limited mechanical response data. Using photodiode signals, Okaro *et al*. [87] trained a semi-supervised Gaussian Mixture Model (GMM) that categorizes AM structures into two groups ('acceptable' and 'faulty') based on their mechanical properties. Okaro *et al*. showed that their proposed semi-supervised approach could produce results comparable to those of a supervised learning algorithm trained on all labeled data.

2.1.4 Reinforcement Learning (RL)

Reinforcement Learning (RL) is an ML technique that allows an agent to interact with the environment of interest via a trial-and-error procedure in order to learn how to control that system and maximize a numerical performance metric that expresses a long-term goal [88]-[89]. Unlike supervised, unsupervised, and semi-supervised learning methods, RL does not optimize the network by minimizing a loss function; instead, it aims to maximize a cumulative reward [90]. For the agent to learn the optimal control strategy for a particular task, RL methods need a well-defined reward function that generates a reward signal (performance metric) responsible for the optimization process. Through interaction with the environment and receiving the reward signal of each state, an agent would learn the optimal sequence that maximizes the long-term reward. For optimizing the control system in RL problems, the agent faces the challenge of discovering new states in order to achieve a possible higher long-term reward while maximizing the immediate

reward at the same time. The Exploration-Exploitation Dilemma is a term used in computer science to describe this trade-off between discovering new states and maximizing immediate reward. Some examples of RL algorithms are Q-learning, temporal difference, and model-free algorithms. Because of their limited appearance in mechanical design and manufacturing literature, the aforementioned three algorithms are not considered as distinct types of reinforcement techniques in this dissertation. Figure 7 depicts a conventional RL mechanism in which the agent performs actions in the environment that are translated into a reward and a state representation, which are then fed back to the agent.

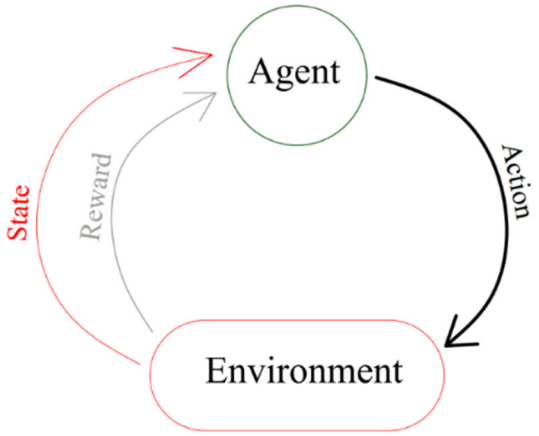

Figure 7: Schematic depicting the RL process.

Mozaffar *et al.* [91] developed a system for the toolpath design of AM processes using a model-free RL algorithm to deposit material in appropriate locations in the fastest way possible. Yang *et al.* [92] used RL to improve the swimming performance of dielectric elastomer-driven soft actuator-based cuttlefish robots, resulting in more than 90 % increase in speed of the robot. Lu *et al.* [93] created an anomaly detection system for monitoring temperature during real-time UAV flight operations using RL techniques. In order to optimize micro-fluidic flow sculpting devices, Lee *et al.* [94] developed a deep RL framework to reduce sculpting pillars while generating flow shapes relatively similar to the target shapes.

2.1.5 Imitation Learning

Imitation Learning is a combination of supervised and RL in which an agent is taught to perform a specific task from a human expert rather than learning the task on its own via the exploration process [95]. In principle, imitation learning is beneficial when it is simpler for an expert to show a particular behavior rather than specifying a reward function that would produce the same behavior through the exploration process. Owan *et al.* [96] utilized imitation learning to decrease cycle time for manufacturing tasks like fastener installation in confined spaces. When confident, their imitation learning model intelligently mimics faster human experts, and when uncertain, it mimics slower human experts.

2.2 Applications of Machine Learning in Mechanical Design and Manufacturing

AI is used in a wide range of industries and business sectors, including healthcare, banking, engineering. In the field of mechanical design and manufacturing, ML and DL technologies have been widely used to aid engineers in developing new design ideas, analyzing their designs, and improving the quality of manufactured products. Design recommendations, defect detection, surrogate modeling, process parameter optimization, and topology optimization are only a few applications of ML and DL in mechanical design and manufacturing. Some of the applications of AI in mechanical design and manufacturing are explored in this section of the dissertation.

2.2.1 Design Recommendations

Different ML methods may be used to obtain an optimal mechanical design, thus reducing the need for human intervention in the mechanical and manufacturing design process. Data collected from the iterative engineering design process by human experts can be used to train ML and DL models to assist other designers in evaluating their design procedure and providing insight for an optimal mechanical design [97]. Fuge *et al.* [98] investigated the ability of content-based

filtering and collaborative filtering for automatic design recommendation in extracting and validating design information using various ML methods (random forest, SVM, logistic regression, etc.). Raina *et al.* [99] developed a DL framework to mimic the actions of a human designer using historical human sequential design data. Raina *et al.* extracted and encoded collections of patterns from sequential design images and subsequently decoded the embedded data back to the original image using a convolutional autoencoder. As seen in Figure 8, The DL model developed by Raina *et al.* learned the operations performed by human designers for truss structure design problems. Yao *et al.* [100] developed an SVM classifier method that can propose AM design features to inexperienced AM designers based on features obtained from actual industrial application examples.

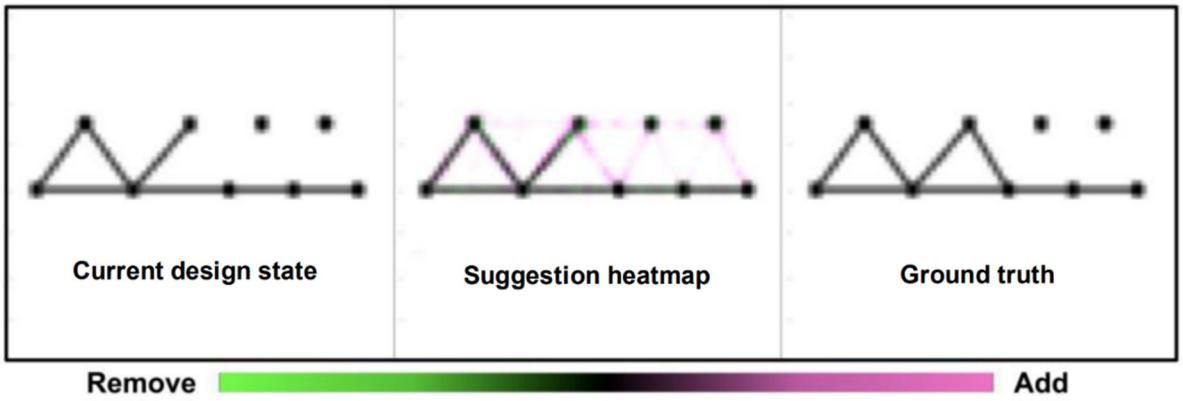

Figure 8: An example of the suggested tress design with the DL model that tries to mimic human designer actions. The color gradient depicts the recommendations, with pink indicating "Add" green indicating "Delete" and black indicating "No Modification" [99].

2.2.2 Defect Detection and Classification

Since the majority of defect detection systems for AM processes rely on cameras to collect data about the condition of the AM structure, defect detection strongly relies on computer vision technologies. Using images recorded during the SLS manufacturing process, Westphal and Seitz

[101] developed a relatively accurate defect detection and classification for AM structure by retraining the existing VGG16 and the Xception CNN models using the transfer learning technique. Narayanan *et al.* [102] developed an in-situ defect detection framework for fused filament manufacturing method based on images collected from an optimal camera using PCA, SVM, and CNN models. Gorbert [103] trained a supervised learning ML model based on layer-by-layer image data collected by a high-resolution camera for defect detection during the PBF manufacturing process. Weimer *et al.* [104] evaluated several CNN configurations to create a visual surface anomaly detection method for manufacturing applications. Weimer shows in Figure 9 that their CNN model can successfully detect the surface anomalies crated during the manufacturing process.

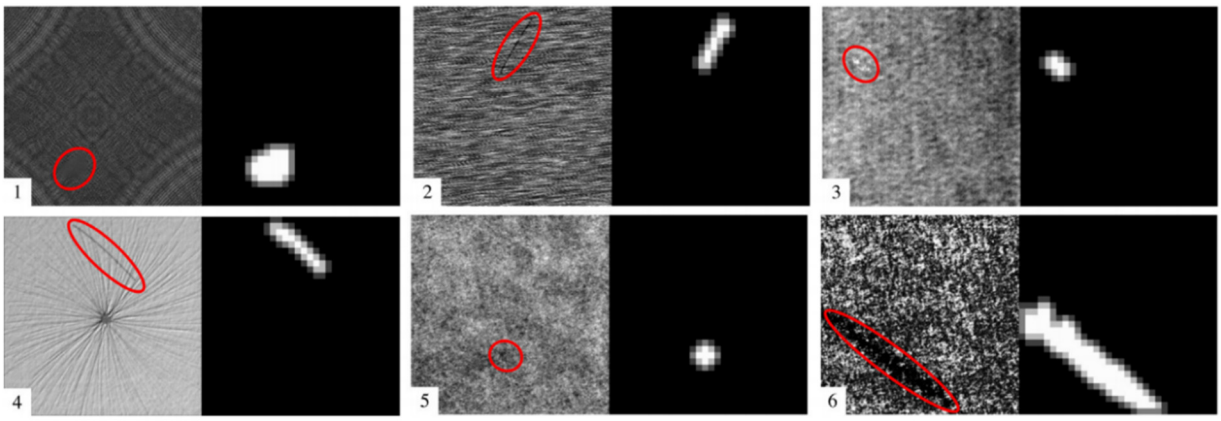

Figure 9: The image of the AM structure (left image in every pair of images) and segmented defect area predicted with CNN model (right image in every pair of images). It must be noted that the numbers on the bottom left side of every pair of images indicated a particular class of defect predicted with the CNN model out of multiple possible defect classes existing in AM structures [104].

In addition to the application of computer vision technologies in defect detection and classification, there have been limited ML-based defect detection methods without the use of image data and computer vision technology. Ye *et al.* [105] developed a deep belief network (DBN)

to detect the balling, keyholing, and cracking during the L-PBF manufacturing process based on the variations in the acoustic signals due to the change of temperature during the solidification process. Grasso *et al.* [106] used in-situ data from multiple sensors embedded in PBF systems to train an ML model for defect detection from received multi-sensor data.

2.2.3 Physic Based Surrogate Models

Physic-based surrogate models are a well-known engineering methodology for approximating a physical model quickly and accurately [107]. Surrogate modeling of mechanical systems based on ML methods is gaining traction in the field of mechanical design and manufacturing as an effective tool for uncovering the complex physics of AM processes and accelerating the mechanical design procedure. The most challenging aspect of the development of a surrogate model with ML and DL techniques is the time-consuming and expensive procedure to develop training data for a wide range of input variables. Despite the time-consuming and expensive development procedure, physics-based surrogate models have low evaluation costs, and they could be used for the development of near-real-time analysis of complex mechanical systems. Stathatos and Vosniakos [108] trained an ANN to develop a real-time surrogate model to determine the temperature and density of AM structures for arbitrary long tracks in laser-based AM based on the results of FEM simulation on small trajectory fragments in the laser-based AM process. Dupuis *et al.* [109] trained an ML model for the development of a surrogate model of an aerodynamic system with consideration of subsonic or transonic conditions.

2.2.4 Processes Parameter optimization

Since manufacturing process parameters directly impact AM structure reliability and structural integrity, optimizing them is a positive step toward improving the quality of the final product. Several researchers trained different ML and DL models to find the complex relationship

between manufacturing process parameters and effective properties of the final products and used the trained model for process parameter optimization. Some researchers utilize ML and DL techniques to discover the complex relationship between manufacturing process parameters and the efficient properties of final products and used these trained models to optimize the manufacturing process parameter. For the optimization of process parameters in the injection molding process, Changyu *et al.* [110] used ANN to figure out the complicated relationship between process conditions and injection molding quality index. Furthermore, they used the power of a genetic algorithm to achieve a global optimization solution for non-linear systems to build a combined ANN and genetic algorithm to optimize the injection molding procedure. Rong-Ji *et al.* [111] developed an ANN model to investigate the impact of manufacturing process parameters on shrinkage during the SLS manufacturing process. Rong-Ji *et al.* optimized the production process parameters using a genetic algorithm based on a trained ANN model. Sukthomya and Tannock [112] introduced an innovative neural network model based on Taguchi experimental design using data collected in a single response process for optimizing manufacturing process parameters.

2.2.5 Topology Optimization

Topology optimization is a structural design technique used in structural design under specific external load and boundary conditions [113]. Traditionally, engineers use FEM and other conventional numerical techniques for the topology optimization of complex structures. Recently, there has been increasing interest in using new AI technologies to optimize the topology of complex structures, including for AM structures. In order to reduce the computational time of the topology optimization process for relatively large structures, Chi *et al.* [114] developed an ML-based framework based on the result of the complex FEM. Chi *et al.* also employed an online updating approach, in which new training data produced from physical simulations is used to

continuously refine the ML model. In order to reduce the number of optimization steps, Sosnovik and Oseledets [115] trained a CNN model based on partially converged design and the changes of that design with respect to the previous optimization step. Yu *et al.* [116] trained a variational autoencoder (VAE) model, as well as a Generative Adversarial Networks (GAN) for the development of a topology optimization framework based on multi-channel images constructed from the applied boundary conditions.

Chapter 3. Prediction of the Heat-Map of Powder Beds in Selective Laser Sintering Process Using Encoder-Decoder Convolutional Neural Network

Selective Laser Sintering is one of the most popular AM methods for manufacturing complex polymeric, metallic, or ceramic structures [117]. The manufacturing process begins by dispersing a thin layer of powder on top of a platform that usually preheats to reduce the thermal gradient during the scanning process and reduce the residual stresses in the final workpiece. The relatively high-power laser scans through the dispersed powder particles, heating them up to the sintering temperature ($T_{melt}/2 < T < T_{melt}$) allowing the micro-powders to be fused in the final product without being fully melted. Subsequently, the platform is lowered by one layer after scanning the first layer, and the dispersing of powder as well as scanning by laser is repeated for the second layer of the powder [118]. This process is repeated until the manufacturing process is completed. The use of jigs and fixtures and any other special tooling equipment is not required during the SLS manufacturing process since the workpiece is immersed in the powder bed and is supported by it. After scanning the last layer of powder particles, the workpiece is gradually cooled down in a controlled temperature environment to avoid any significant change to mechanical properties of the final product due to sudden temperature change [119]. Finally, the manufactured product is removed from the platform after the cooling process, and any extra powders would be cleaned from the final workpiece.

In the PBF processes, such as SLS manufacturing, powder particles are transformed into the AM structure layer-by-layer and path-by-path, allowing for complicated shapes to be printed from powder particles. However, despite their indisputable advantages over subtractive manufacturing, the PBF manufactured structures experience more thermal and residual stresses

due to the high-temperature gradients experience by AM structure during the laser scanning and cooling process. Therefore, modeling transient temperatures throughout the SLS manufacturing process is critical for determining the quality of the final product. On the other hand, simulation of the thermal field of SLS manufactured structure requires a complicated numerical model due to the discrete nature of powder particles used in this AM process.

Traditional numerical methods for simulating the thermal field of AM structures such as FEM and DEM techniques are time intensive and cannot be utilized to construct a real-time simulation or process control system. A sophisticated and time-consuming physics-based model was utilized in this chapter of the dissertation to develop a dataset for training a DL model developed here. The physics-based model is not new and was developed by Gobal and Ravani [4]. It is used here to develop a dataset by simulating thousands of position-time representations of the laser head with various process parameters and their corresponding heat-map of AM structures. Moreover, this dataset is used to train a DL model developed in this dissertation which would provide for a sub-second prediction of the thermal field of powder beds during the AM process.

3.1 Developing Dataset for the Deep Learning Model of Thermal Field of Powder-Based AM structures

A dataset for training a DL model is generated using a physics-based numerical model of the thermal field of the SLS manufactured structure developed by Gobal and Ravani [4]. On average, the generated DL model is shown to be more than 41,000 times faster than the physics-based model, and therefore, it has the potential to create a near real-time simulation of the thermal field of AM structures that might be the foundation of a future process control system for the SLS manufacturing process.

The DL model utilized in this dissertation employs a deep encoder-decoder CNN

architecture that can be used for pixel-wise mapping of the input image (2D or 3D array of number) to output image corresponding to the inputted image; as a result, the training procedure of this DL model requires a significant number of pairs of images [120]-[121]-[122]. The deep encoder-decoder CNN architecture is made up of three networks: an encoder network that extracts a collection of patterns from the input image, a decoder network that generates the output image, and a bottleneck network that incorporates some data into the DL model and connects the encoder and decoder networks together.

Using convolutional layers, the encoder network of the proposed deep encoder-decoder CNN model captures local and global patterns from a 2D representation of the trajectory of the laser head. For spatial down-sampling of outputted data from each convolutional layer, the encoder network employs max-pooling layers. The encoder network generates a compressed and distorted version of the 2D representation of the trajectory of the laser head. This compressed version of the input image later would be flattened and passed into the bottleneck network, which is made up of multiple FC layers. The process parameters and mechanical characteristics of powder particles were concatenated into the first layer of the bottleneck network to integrate their influence on the thermal field of AM structures. The output of the bottleneck network would be the 1D encoded state of the laser head trajectory as well as AM process parameters and mechanical properties of powder particles. In order to decode this encoded state into the heat-map of AM structure, multiple stacks of convolutional and up-sampling layers were used in the decoder network of the proposed DL model. These up-sampling layers in the decoder network of the proposed DL model are not trainable, and they only use an interpolation technique to enlarge the images.

The most critical step before the training process of the DL model developed here is to collect and preprocess a dataset including thousands of laser head trajectories with various AM

process parameters and mechanical properties of powder particles along with their corresponding image representation of SLS manufactured structure. An image representation of the trajectory of the laser head (2D position-time representation of laser head) can be easily obtained by discretizing the powder bed with small uniform cubes and assigning a number to each cube with respect to the trajectory (position-time history) of the laser beam. Figure 19 depicted the procedure for generating a 2D position-time representation of a laser head for a domain of study discretized by the same size cubes to a 5×5 2D array of numbers. It should be pointed out, however, in the simulations conducted in this dissertation, the powder beds were converted to a 100×100 2D array of numbers.

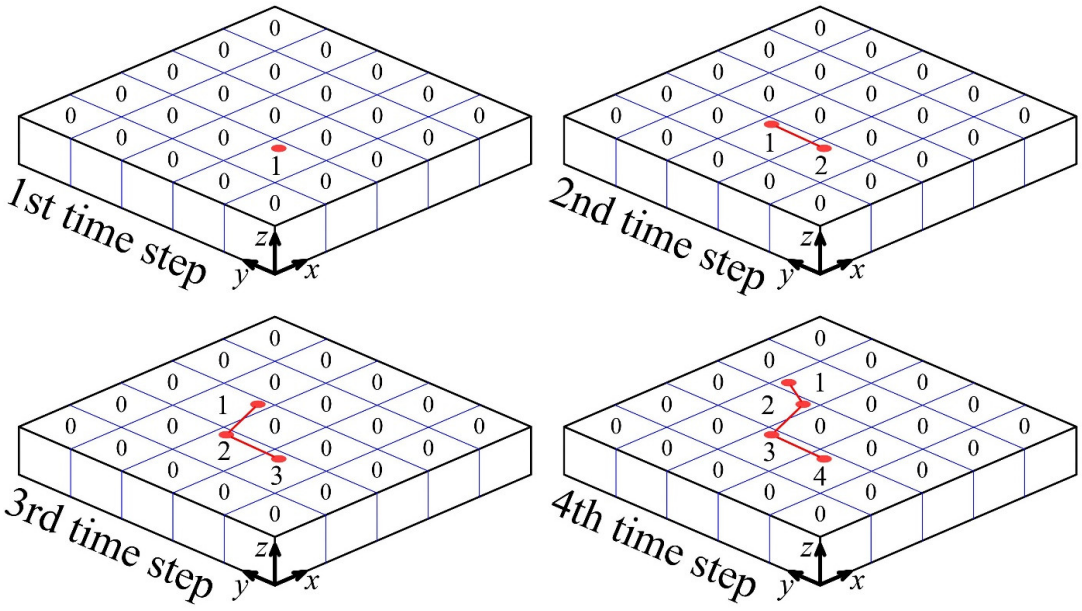

Figure 10: The construction of 2D image representation of the trajectory of the laser head for the first 4 time step of the physics-based simulation.

In order to construct the 2D image representation of the trajectory of the laser head corresponding to the first time step of the physics-based simulation, the number one is assigned to the cube in which the center of the laser beam is currently placed inside its border and zeros to all other cubes in the domain. As the laser head moves to a new location in the next time step of the

simulation, the number allocated to all cubes in the domain would be incremented by one with the exception of cubes having an already assigned value of zero. Again, in this new time step, the number one would be allocated to the cube corresponding to the present position of the laser beam. By continuously using the aforementioned technique from the initial to the final time step of each physics-based simulation, the 2D image representation of the trajectory of the laser head is generated.

The cubes with relatively small non-zero value in their 2D representation of laser head trajectory (i.e., the cubes which laser passed through them more recently) have extensively higher temperatures compare to the cubes with a relatively large value. In order to clearly represent this extensive temperature difference between the cubes in which the laser passed through them recently and the ones that laser passed through them relatively earlier to DL model, the non-zero elements of the position-time representation of the laser head were subjected to an exponentially decaying function. After training the DL model with data subjected to several different decaying functions, the following exponentially decaying function was chosen for the mentioned task:

$$f(x) = e^{-x/500} \tag{1}$$

where x is the non-zero elements of the position-time image representation of the laser head. This decay function (Eq. 1) maps the lower non-zero integer in the developed images (the earlier position of the laser beam) to near-one values and maps the highest number of time steps in all numerical examples (2,372) to a near-zero value; hence, no further input data scaling is necessary. Moreover, because exponential functions decrease quicker than linear functions, the difference between the present position of the laser and the location where it has previously passed through would be more evident to the DL model.

The manufacturing process parameters such as the velocity of the laser head, the diameter

of the laser head, and laser power as well as material properties of powder particles are not included in the developed 2D position-time representation of the laser head. These essential input parameters would be independently introduced to the DL model by concatenating them into the 1D array of numbers that are flattened from the output of the encoder network (first FC layer of the bottleneck network). Physics-based simulations in this dissertation were performed on a 5mm × 5mm × 0.05mm powder bed domain, which was discretized using 0.05mm × 0.05mm × 0.05mm cubes, converting the structure to a 100×100 2D array of numbers.

The heat-map of AM structure generated from the physics-based simulation was labeled on each position-time representation of laser head and their corresponding process parameters and mechanical properties of powder particles. It is easier to construct an image representation for the heat-map of an AM structure than it is to construct a position-time representation of the laser head. The previously established discretization approach for generating a 2D position-time representation of the laser head is utilized to create an image representation of the heat-map of the AM structure. As a result, the AM structure is turned into a 100×100 2D array of numbers again. The average temperature of all particles, including fine or coarse particles used in the adaptive DEM method whose centers are located inside the cubes, may be used to calculate the number assigned to each element of the 2D array.

3.2 Prediction of the Heat-Map of Powder Beds Using Deep Encoder-Decoder Convolutional Neural Network Model

Convolutional (Conv) layers and max-pooling layers are used in the encoder network of the proposed DL architecture to extract patterns from the 2D representation of the trajectory of the laser head. Every convolutional layer is made up of multiple small learnable matrices of weights known as filters, which recognize spatial patterns in the given 2D representation of 2D position-

time representation of the laser head by detecting changes in intensity values of the image [123]. These filters could be considered as learnable windows of weights that slide over the image to extract essential features from a given 2D array of numbers using convolutional operation. In general, convolutional processes is sent through a nonlinear activation function to solve complex problems by adding nonlinearity to the convoluted input. The ReLU activation function is employed in this dissertation to create a nonlinear decision boundary in a deep neural network. Because it avoids problems with vanishing gradients and has a substantially shorter run time than other nonlinear activation functions such as *sigmoid*, the ReLU is the most often employed activation function in DL [124]-[125]. In addition, the output of convolutional layers is often fed into a pooling layer to reduce the size of data and alleviate overfitting concerns [126]. The max-pooling layer, which is the most common pooling approach for CNN, is used in this dissertation to extract the essential features of the 2D array of numbers. The convolutional operation, activation function, and pooling operation must be stacked together to learn hierarchical visual representations from a 2D array of numbers in the encoder network of the DL model.

The output of the encoder network is flattened and is concatenated here with ten numbers representing the mechanical properties of powder particles. The material properties considered are density, melting temperature, heat capacity, thermal conductivity, Young's modulus, and Poisson's ratio, absorption coefficient, surface energy per unit area, atomic volume, and diffusion coefficient. In addition, three numbers are used to represent the manufacturing process parameters, namely laser power, the radius of the laser beam, and the scanning speed making for a total of thirteen numbers. It is worth mentioning that all these numbers are scaled between 0 and 1 before getting concatenated into the flattened output of the encoder network. The data will pass through several FC layers in the bottleneck network after concatenating the encoder network output with the

mechanical properties of powder particles and manufacturing process parameters. Since the perceptrons in FC layers are interconnected, the FC layers are able to learn global information from input data. As a result, the output of the bottleneck section would be an encoded 1D representation of the whole manufacturing process from the start to the present time step.

The output of the bottleneck section of the proposed DL architecture is reshaped to a low-resolution 2D array of numbers representing the heat-map of AM structure. The purpose of the decoder network is to recreate the heat-map of the AM structure in its original 100×100 shape. The decoder networks may utilize transposed convolutional layers or up-sampling layers combined with convolutional layers to accomplish nonlinear decoding of the encoded state into the heat-map of AM structure [127]. In this dissertation, the reshaped output of the bottleneck section is fed into the decoder network, consisting of up-sampling layers combined with convolutional layers. The proposed network employs the bilinear interpolation up-sampling approach to boost spatial resolution while maintaining a 2D representation of the image. The output of the decoder network would be a 2D array of numbers with the same shape as the supplied 2D position-time representation of the laser head after passing data through multiple up-sampling layers paired with convolutional layers. The pixels of the heat-maps of AM structures in the developed dataset have values ranging from 373 K to 1773 K, which are scaled to values ranging from 0 to 1 for DL training purposes. The ReLU activation function is utilized in the output layer of the DL model since there are no negative values in the scaled heat-map of the AM structure.

The developed dataset comprises of 116,237 pairs of images representing the position-time sequence of the laser head with the image representations of the heat-map of AM structures and their accompanying manufacturing process parameters and mechanical properties of powders particle. The physics-based simulation was run for two distinct powder particles, six distinct laser

pathways, various laser powers, laser beam radii, and scanning speeds to collect the dataset.

Solid-state sintering for metallic materials happens at temperatures far higher than 400 K, whereas only 13.57 percent of cubes in each heat-map in the dataset had temperatures over 400 K on average (the temperatures of 86.43 percent of the cubes in each heat-map are between 373 and 400 K on average). Using the standard mean squared error (MSE) loss function to predict an extremely sparse heat-map of AM structures would result in the DL model predicting a white picture with uncommon high values that differ from the ground truth label. Using standard MSE, the predicted temperatures of cubes in each 100×100 2D array of numbers are very similar, hovering around 373 K, posing a complex problem in predicting the temperature of more important hot cubes. Inspired by the work of Somandepalli *et al.* [128] in developing a custom loss function with an additional penalty for misclassification in a multi-class pixel labeling problem, a custom MSE loss function is used here that reduces errors associated with temperatures between 373 K and 400 K (0 to 0.01928 after scaling) and thus penalizes the prediction of cell values higher than 400 K (0.01928 after scaling). The proposed DL model aims to generate an output picture representation of the AM structure heat-map that is similar to the heat-map obtained by physics-based simulation (label image). The pixel-wise similarity between the output image and the label image can be evaluated using a custom MSE loss function as follows:

$$J(W,b)=\frac{1}{N_{ex}T_wT_h}\sum_{i=1}^{N_{ex}}\sum_{n=1}^{T_w}\sum_{m=1}^{T_h}\begin{cases}\beta\left(y_i^{(n,m)}-\hat{y}_i^{(n,m)}\right)^2 & \text{if } y_i^{(n,m)}<0.01928,\\ \left(y_i^{(n,m)}-\hat{y}_i^{(n,m)}\right)^2 & \text{otherwise,}\end{cases} \tag{2}$$

where W and b are learnable weight and bias parameters of convolutional layers and FC layers throughout the DL model. These must be tuned using the backpropagation method. T_w and T_h

are number of pixels in width and heights of both output image and label image, N_{ex} is the number of pixelated AM structure in each batch of data, β is the hyper-parameter that regulates the penalty reduction for cell values below 400 K ($0< \beta \leq 1$, the value of β in our model is set to be 0.1), $\hat{y}_i^{(n,m)}$ is the output pixel of the DL model located at the width of n and hight of m, and $y_i^{(n,m)}$ is the ground truth label associated with $\hat{y}_i^{(n,m)}$ output pixel.

The architecture of the deep encoder-decoder CNN proposed in this dissertation is shown in Figure 11. This DL model encoder network uses four stacks of convolutional operations, ReLU activation function, and pooling operation followed by a flattened layer. Both 2D representation of the trajectory of laser head (input image to DL model) and heat-map of powder bed (output image to DL model) are 100×100 2D array of numbers; hence, the padding operation of hidden layers must be selected in a fashion so that the DL model output would be a 100×100 2D array of numbers. Therefore, the same padding technique is applied to all convolutional and max-pooling operation in the encoder network and the first two convolutional operations in the decoder network. Furthermore, the third and fourth convolutional operation in the decoder network are being subjected to valid padding. The number of channels in the encoder network increases from Conv-1 to Conv-4, and all convolutional (Conv) layers have 3×3 kernels, and all max-pooling operations have a 2×2 filter. The flattened perceptrons are concatenated with thirteen numbers representing process parameters and mechanical characteristics of powder particles, as previously discussed. These are sent to the FC layers in the bottleneck network of the DL model. Each of the first four FC layers in the bottleneck section (FC-5 to FC-8) has the same number of units. However, more perceptrons are dedicated to the last FC layer (FC-9) so that it can be reshaped to the size of the first convolutional layer in the decoder network (Conv-10). To decode the encoded state into the heat-map of AM structure, the decoder network employs four stacks of convolutional

operations, ReLU activation function, and up-sampling procedure with a 2×2 filter. The number of channels in the decoder section decreases from Conv-10 to a single-channel output.

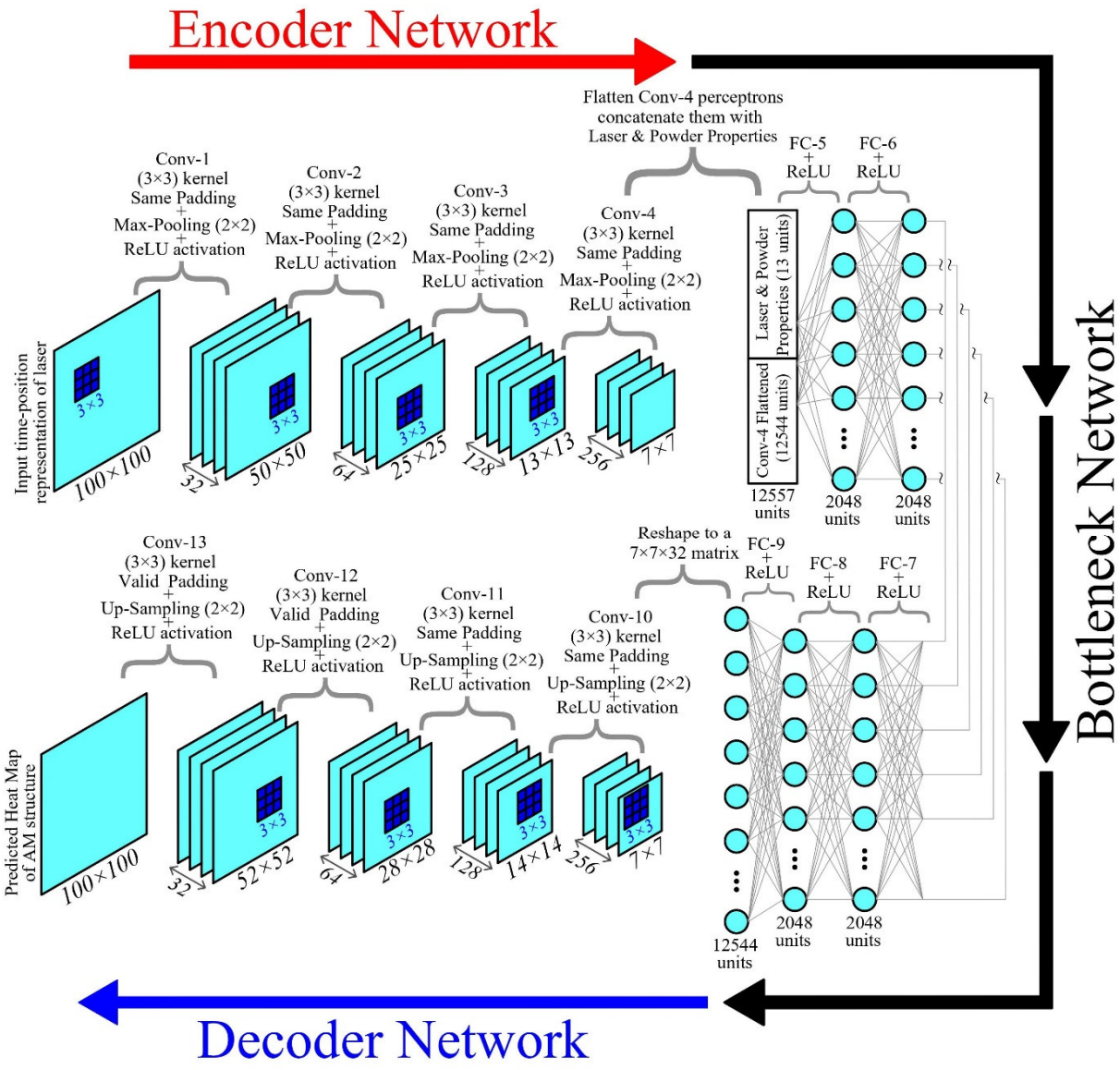

Figure 11: The deep encoder-decoder CNN architecture for the prediction of the heat-map of the AM structure.

Training of the DL model for this huge dataset is a time-consuming process; therefore, the original dataset was shuffled to create a subset of original data with only 20,000 images to investigate the effect of different hyper-parameters on the accuracy of the model. The original dataset was randomly subdivided into 16,000 training and 4,000 validation samples. Some of

hyper-parameters including learning rate, batch size, the number of neurons per FC layer, the percentage of dropout in FC layers, and the number of filters in Conv layers were fine-tuned via the empirical study in order to develop a DL model with high prediction performance, while the other hyper-parameters were left at their default values in the Keras API.

After the empirical tuning process, the ReLU activation function is chosen for all Conv and FC layers. In this process, the dropout percentage is set to be 40%, and the batch size is set to be 256. Several combinations of the number of filters in Conv layers, the number of neurons per FC layers, and the learning rates are used to train the deep encoder-decoder CNN model and find optimal hyper-parameter settings. Figure 12 depicts the loss versus the number of data batches for the proposed DL model using the six hyper-parameter settings listed in Table 1. These six networks are backpropagated on the custom MSE loss function (see Eq. 2), and they are optimized with the adaptive moment estimation (Adam) algorithm.

Table 1: Six different hyper-parameter settings (DEDCNN-1 to 6) for the deep encoder-decoder network.

Hyper-parameter Settings	**Encoder and Decoder Networks Number of filters in Conv layers**				**Bottleneck Network Number of neurons per FC layers**					
	Conv-1 & Conv-13	**Conv-2 & Conv-12**	**Conv-3 & Conv-11**	**Conv-4 & Conv-10**	**FC-5**	**FC-6**	**FC-7**	**FC-8**	**FC-9**	**Learning rate**
DEDCNN-1	8	16	32	64	1024	1024	1024	1024	3136	0.0001
DEDCNN-2	32	64	128	256	1024	1024	1024	1024	6272	0.0001
DEDCNN-3	64	128	256	512	2048	2048	2048	2048	25088	0.0001
DEDCNN-4	16	32	64	128	2048	2048	2048	2048	6272	0.001
DEDCNN-5	64	128	256	512	2048	2048	2048	2048	25088	0.001
DEDCNN-6	32	64	128	256	2048	2048	2048	2048	12544	0.001

As shown in Figure 12, reducing the learning rate can extremely slow down the learning process, which is not always a reasonable solution to reduce the bias of the DL model. The learning

rate is a configurable hyperparameter in DL optimization algorithms that control how quickly the loss function is minimized at each iteration [129]. One can see in Figure 12, the encoder-decoder CNN models with DEDCNN-4 to DEDCNN-6 hyper-parameter settings (which have higher learning rates) converged faster than DEDCNN-1 to DEDCNN-3. Even though the DEDCNN-6 hyper-parameter setting has a lower number of trainable parameters (65.37 million) than the DEDCNN-5 hyper-parameter setting (93.97 million), the network with the DEDCNN-6 hyper-parameter setting had a lower error after training for 6000 batches of data. Moreover, since DEDCNN-6 has a smaller number of perceptrons than DEDCNN-5, the forward propagation process for an unseen example would be quicker for the DL model with the DEDCNN-6 hyper-parameter setting. Therefore, the DL model with the DEDCNN-6 hyper-parameter setting was chosen to be trained on the larger dataset for a higher number of epochs.

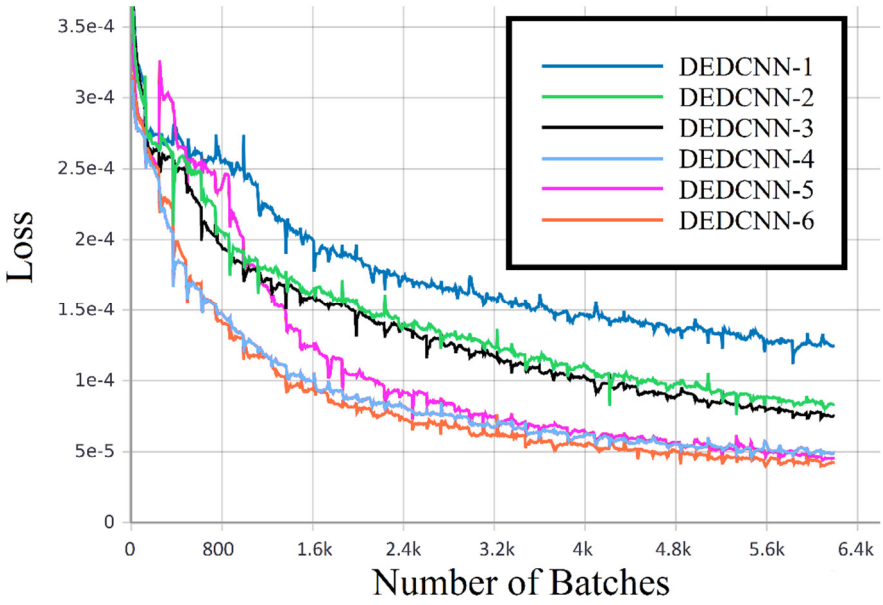

Figure 12: Training loss vs. the number of batches of data for deep encoder-decoder CNN training with six different hyper-parameter settings (DEDCNN-1 to DEDCNN-6).

50,000 pairs of images with their corresponding manufacturing process parameters and mechanical properties of powder particles are randomly selected from the entire dataset and then

randomly split into 40,000 training and 10,000 validation examples to train the deep encoder-decoder CNN model DEDCNN-6 hyper-parameter configuration on a relatively large dataset. The DL model with the DEDCNN-6 hyper-parameter configuration takes 171.92 hours to train for 300 epochs on this complicated dataset. Figure 13 shows the training and validation loss for the DL model trained on the larger dataset with the DEDCNN-6 hyper-parameter configuration versus the number of epochs. As can be seen in Figure 13, after 250 epochs, both training and validation loss converge to relatively low loss values. Additionally, the DL model does not suffer from variance issues since the difference between training and validation loss is negligible.

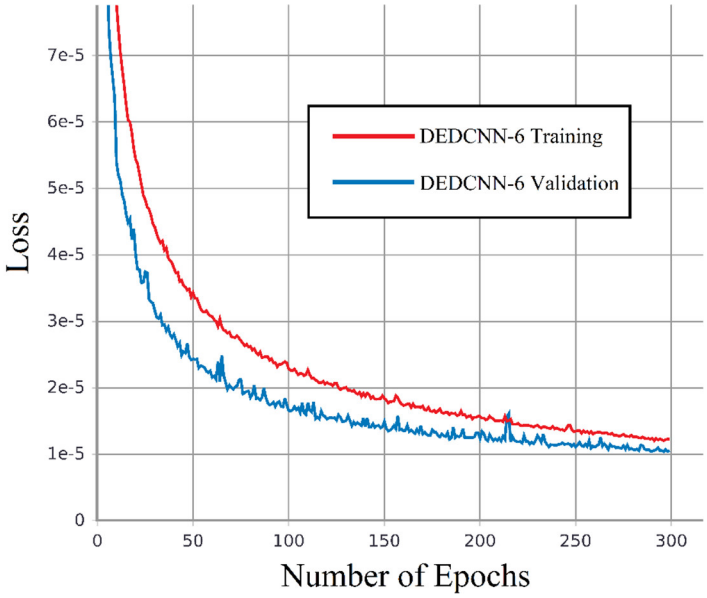

Figure 13: Training and validation loss vs. the number of epochs for the deep encoder-decoder CNN model with DEDCNN-6 hyper-parameter setting trained on 50,000 examples.

Figure 14 shows how effectively the proposed DL model with DEDCNN-6 hyper-parameter configuration predicts the heat-map of an Inconel-713 AM structure after being trained for a particular number of epochs. The ground truth label for this specific unseen example is shown in the bottom right heat-map in Figure 5, with the other eight heat-maps displaying the output of the DL model trained for 4 to 300 epochs. As depicted in Figure 14, the generated heat-map

becomes more similar to the ground truth label as the DL model is trained for more epochs.

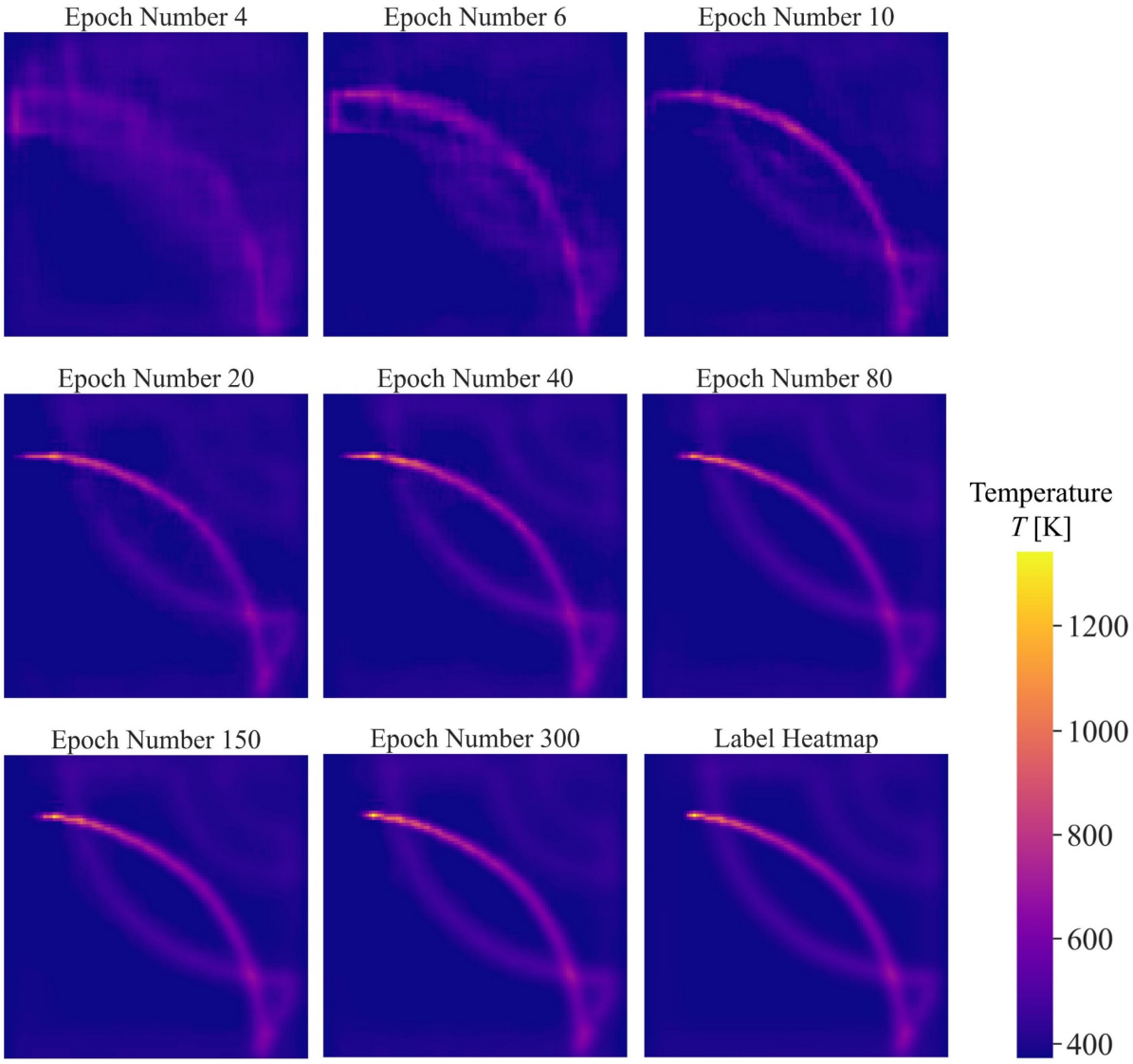

Figure 14: Evolution of the heat-map prediction with the DL model trained for different epochs.

3.3 Numerical Examples for the Evaluation of the Data-Driven Model of the Thermal Field of Powder Beds

Several examples are provided in this section of Chapter 3 to demonstrate the computational performance of the proposed DL model for predicting the thermal field of AM structures at any stage of the manufacturing process. Table 2 and Figure 15 show the material

properties of the powder particles and the six distinct laser pathways employed in the physics-based simulation, respectively. Powder particles having a mean diameter of 15 μm and a standard variation of 10 μm are created for all physics-based simulations with an initial preheat temperature of 373 K. Moreover, the thermal gradient in the vicinity of the melt pool is reduced by heating the underlying substrate to 373 K. This pre-heating decreases the amount of residual distortion during the scanning of the first layer of the powder [130]. For the physics-based simulations, the laser power, scanning speed, and laser beam radius were set to 50 to 140 W, 1 to 2 m/s, and 50 to 75 μm, respectively. For all simulations, the powder bed packing density is set at 58 percent.

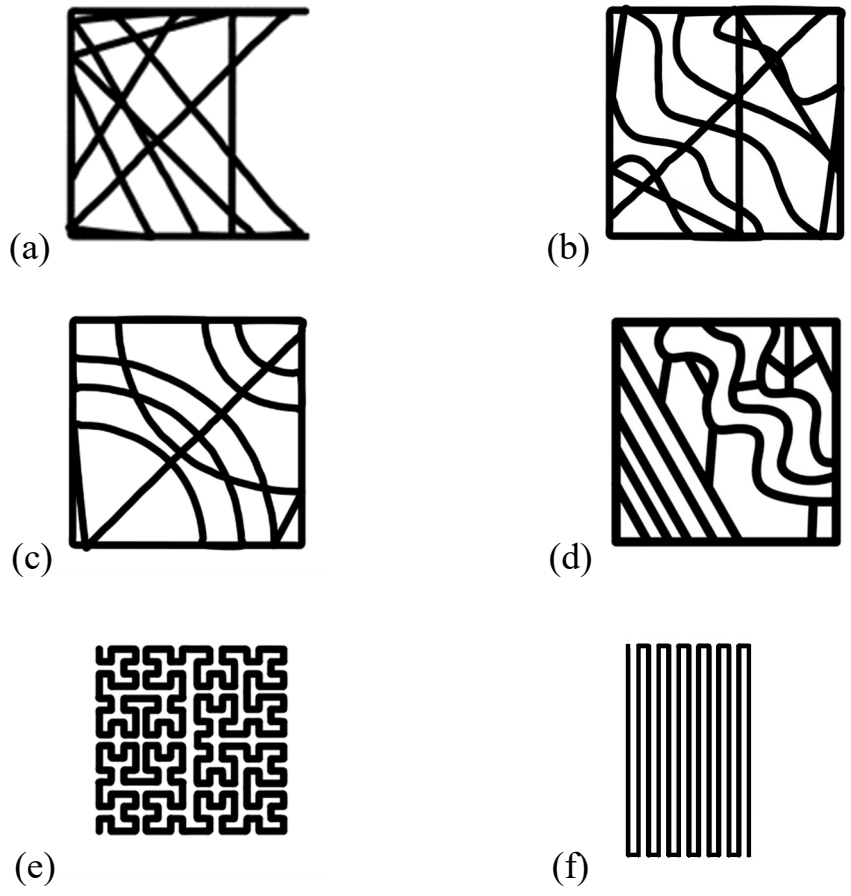

Figure 15: six different laser path used in the simulations (a) the first laser path with 1,211 time steps, (b) the second laser path with 1,479 time steps, (c) the third laser path with 1,413 time steps, (d) the fourth laser path with 1,591 time steps, (e) the fifth laser path with 2,372 time steps, (f) the six laser path with 2,242 time steps.

Table 2: Material properties of powder particles, [18]-[131]-[132]-[133]-[134]-[135]-[136]

Material Property	**Steel**	**Inconel-713**	**Unit**
Density (ρ)	7800	8190	Kg/m^3
melting temperature (T_{melt})	1500	1335	°C
Thermal conductivity (c)	600	435	J/kg K
Solid conductivity (τ)	40	8.9	W/m K
Young's modulus (E)	210	200	GPa
Poisson's ratio (ν)	0.28	0.278	-
Absorption (K_{ab})	0.3	0.87	-
Surface energy (γ_s)	1	2.34	J/m^2
Atomic volume (Ω_0)	1.18×10^{-29}	1.22×10^{-29}	m^3
Diffusion coefficient (D_g)	3.83×10^{-19}	1.85×10^{-18}	m^3/s

Figure 16 and Figure 17 compare the heat-maps of AM structure evaluated using physics-based simulations and its equivalent heat-map predicted with DL model (see Figure 15 for laser pathways) at the 255th time step of the fifth laser pathway with Inconel-713 powders and 1,000th time step of the sixth laser path with steel powders, respectively. The manufacturing process parameters used to generate Figure 16 are 80 W laser power, 70 μm laser radius, and 1.25 m/s scanning speed, whereas Figure 17 generated with a 120 W laser, a 70 μm laser radius, and a 2 m/s scanning speed. The high-temperature region of both simulation and DL evaluated heat-maps have been enlarged in Figure 16 and presented at the bottom of the figure for a better presentation of the heated region. It took the physics-based simulation 640.42 and 807.25 seconds to generate the heat-maps shown on the left side of Figure 16 and Figure 17, respectively.

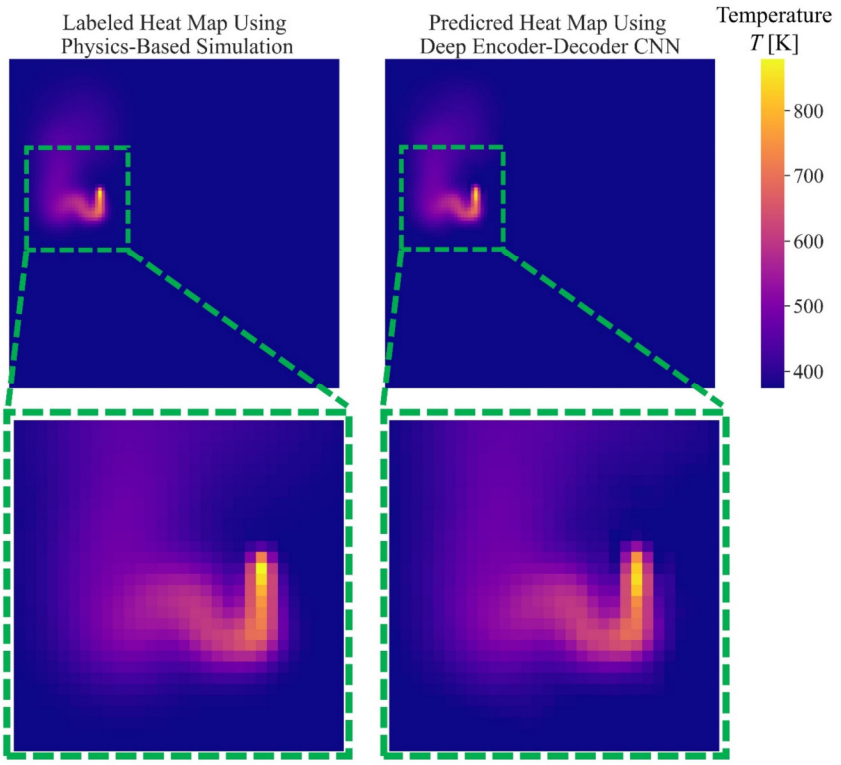

Figure 16: Heat-map of AM structure evaluated with physics-based simulations (two heat-maps on the left side), and predicted with DL model (two heat-maps on the right side) at 255th time step of fifth laser path.

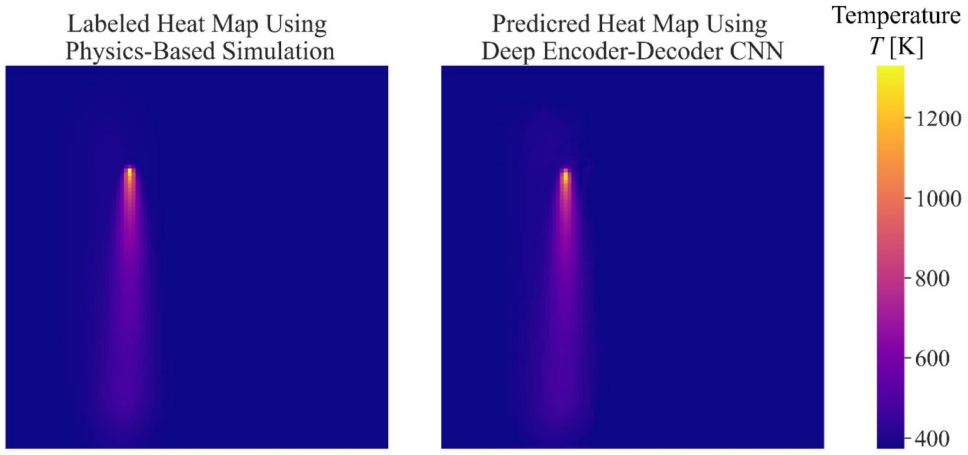

Figure 17: Heat-map of AM structure evaluated with physics-based simulations (the heat-map on the left side), and predicted with DL model (the heat-map on the right side) at 1,000th time step of sixth laser path.

The DL model only took 20.5 and 18.2 milliseconds to forward propagate the 2D representation of the laser head's trajectory, manufacturing process parameters, and the properties of the powder particles associated with the 255th time steps of the fifth laser path and 1,000th time step of the sixth laser path, respectively. An excellent agreement with the results of the physics-based simulations can be seen in both cases.

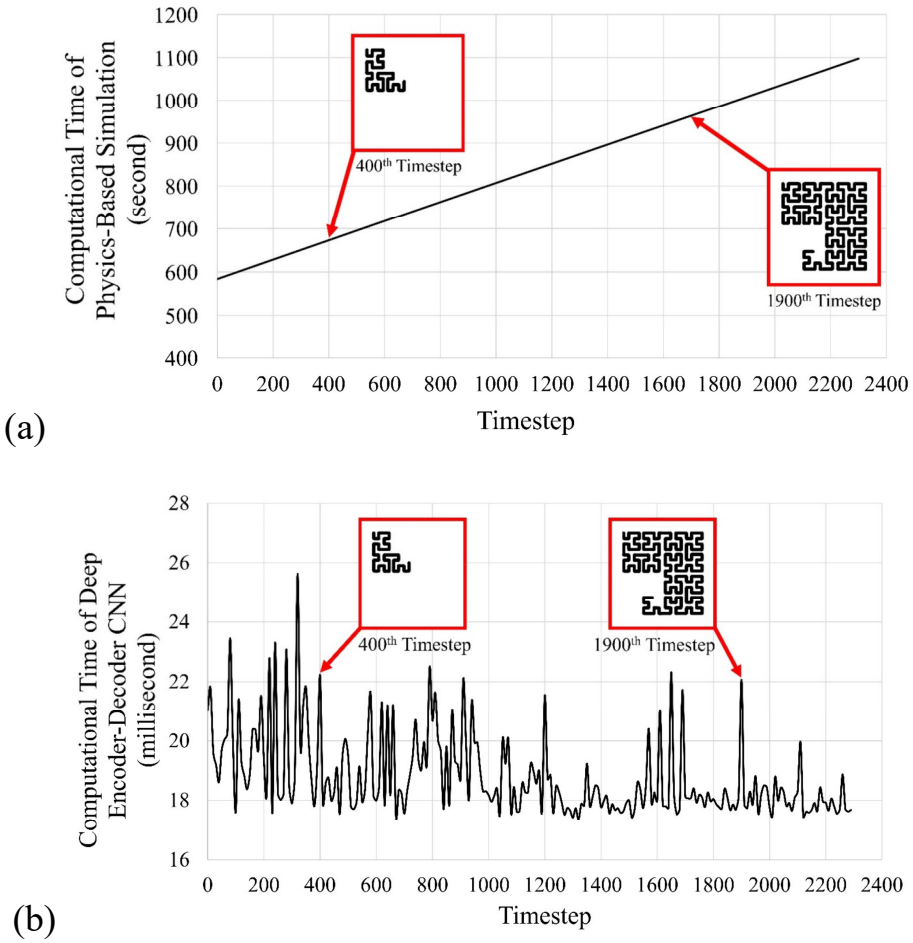

Figure 18: Computational time vs. the number of the time step for (a) physics-based simulation and (b) deep encoder-decoder CNN model.

For each time step of the fifth laser pathway, Figure 18 depicts the computing time required to assess the thermal field of AM structures throughout the SLS manufacturing process using both physics-based simulations (Figure 18(a)) and the DL model (Figure 18(b)). Figure 18 evaluates

the computational times using the identical material properties and manufacturing process parameters that were utilized to construct Figure 16. As can be seen, the computing time of the DL model is significantly less than the time required to solve the problem using physics-based simulation. Moreover, as shown in Figure 18(a), the computing time in the physics-based simulation grows linearly with the number of executed time steps.

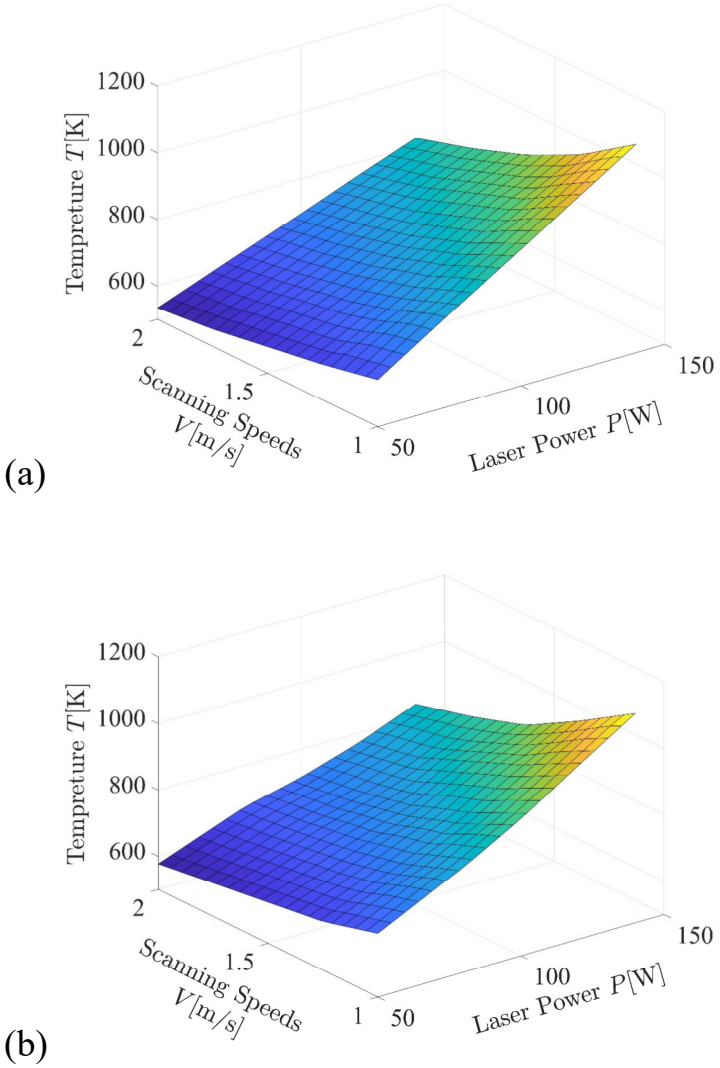

Figure 19: The average temperature of the ten hottest cubes at 200th time step of the fifth path for variable laser powers and scanning speeds using (a) the physics-based simulation and (b) the deep encoder-decoder CNN model.

For various laser powers and scanning speeds, Figure 19 shows the average temperature of the ten hottest cubes at the 200^{th} time step of the fifth pathway (see Figure 15 for paths). The average temperature of the ten hottest cubes was calculated using physics-based simulation and the DL model for twenty-three distinct combinations of laser powers and scanning speeds from the dataset. Steel powder was used as the powder material in these simulations, and the laser beam radius was adjusted to 70 μm for all simulations. As illustrated in Figure 19, the average temperature of the ten cubes calculated with the DL model follows the same trend as the average temperature obtained with the physics-based simulation.

Chapter 4. Prediction of Aggregate Elastic Properties of Powder Beds in Selective Laser Sintering using Convolutional Neural Network

The aim of the physical modeling of powder-based additive production processes is to relate the macroscopic mechanical characteristics of AM parts to their microscopic structural features. The Finite Element Method or Discrete Element Method techniques are the most often used method for determining the effective elastic properties of powder-based AM structures. Although, these numerical models are time-consuming and could limit our ability to develop a simulation-based real-time control system to evaluate effective elastic properties of AM structures.

This chapter of the dissertation presents a novel DL method for determining aggregate elastic properties of SLS manufactured structures. The proposed DL method was validated for unseen SLS manufactured structures by comparing the results of a DEM simulation. The average discrepancy in predicted effective elastic properties of AM structure between sub-second DL model and time-consuming DEM simulation is less than 4%. Therefore, the proposed DL model will be very beneficial in developing a real-time control system for predicting the aggregate elastic properties of powder beds during the manufacturing process.

4.1 Physics-Based Simulation of Aggregate Elastic Properties of Powder Beds

The analysis of the force-displacement behavior of each pair of sintered powder particles within the SLS manufacturing domain is the first step towards establishing a DEM simulation for predicting the effective elastic properties of powder-based AM structures and subsequently training of a DL model capable of sub-second prediction of effective elastic properties of the aggregate. Jefferson *et al.* [25] developed the particle response law for both normal and tangential

relative deformation between each pair of powder particles using a sophisticated FEM simulation and demonstrated that this force-displacement model agrees with the Hertzian contact theory. Moreover, Liu *et al.* [26] simplified the force-displacement model proposed by Jefferson *et al.* by representing each pair of partially sintered particles as truncated elastic spheres overlapping adjacent particles with an elastic bridge capable of transmitting normal force, tangential forces, and rotational moments.

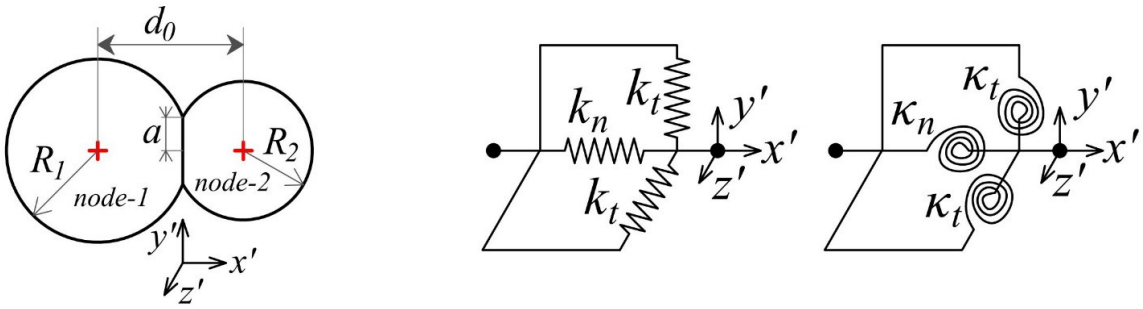

Figure 20: A pair of sintered particles (left), the system of 6 springs connecting two particles (right).

As depicted in Figure 20, the force-displacement between each pair of particles was numerically modeled in this dissertation using a single normal spring k_n, two tangential springs k_t, one torsional spring normal to the plane of contact κ_n And two torsional springs tangent to the plane of κ_t. Gobal [137] established the spring constants using the Liu *et al.* [138] force-displacement model as follows:

$$k_n = \frac{Ea}{1-\nu^2}\left\{\frac{1+a^*\left[\frac{\pi}{6}\left(1-\nu^2\right)\left(1+2a^*\right)-a^*\right]}{\sqrt{\left(1-a^{*2}\right)}-\bar{\psi}\left(a^*+a^{*2}\left[\frac{\pi}{6}\left(1-\nu^2\right)\left(1+2a^*\right)-a^*\right]\right)}\right\}, \tag{3}$$

$$k_t = \frac{2Ea}{(2-\nu)(1+\nu)}\left\{\frac{1+a^*\left[\frac{\pi}{6}\left(1-\nu^2\right)\left(1+2a^*\right)-a^*\right]}{\sqrt{\left(1-a^{*2}\right)}}\right\}, \tag{4}$$

$$\kappa_n = \frac{8ER^3a^{*3}}{(2-\nu)(1+\nu)}\left\{\frac{1+a^*\left[\frac{\pi}{6}(1-\nu^2)(1+2a^*)-a^*\right]}{\sqrt{(1-a^{*2})}}\right\}, \tag{5}$$

$$\kappa_t = \frac{2ER^3a^{*3}}{(1-\nu^2)}\left\{\frac{1+a^*\left[\frac{\pi}{6}(1-\nu^2)(1+2a^*)-a^*\right]}{\sqrt{(1-a^{*2})}-\bar{\psi}\left(a^*+a^{*2}\left[\frac{\pi}{6}(1-\nu^2)(1+2a^*)-a^*\right]\right)}\right\}, \tag{6}$$

where a^* is nondimensionalized contact radius a with effective curvature R (i.e., $a^* = a/R$), and $\bar{\psi}$ is the geometric term that needs to be evaluated from the distribution of load on the particles [25]. Liu *et al.* [138] experimented with several values of the geometric term and found that $\bar{\psi} = 0.08$ provides the greatest match to the experimental data, hence, the same value is used in this dissertation for modeling the bounding forces and momentum of the partially sintered particle. Furthermore, in order to prevent the stiffnesses mentioned in Eq. 3 to Eq. 6, turn into complex numbers, a^* must be less than one ($a^* < 1$).

The force-displacement model used in this dissertation is based on DEM developed by Gobal [137], in which beam elements constructed within every two sintered particles have 6 degrees of freedom (DoF) per particle (node). This force-displacement model ($\mathbf{f}' = \mathbf{K}'\mathbf{u}'$) is between two particles where the displacement vector is $\mathbf{u}' = (\mathrm{u}'_1, \mathrm{u}'_2, \ldots, \mathrm{u}'_{12})$ and force vector is $\mathbf{f}' = (\mathrm{f}'_1, \mathrm{f}'_2, \ldots, \mathrm{f}'_{12})$. Gobal [137] developed a 12×12 stiffness matrix of the local equivalent beam element using the unit displacement technique as follows:

$$\mathbf{K}' = \begin{bmatrix} \mathbf{K}'_{11} & \mathbf{K}'_{12} \\ \mathbf{K}'_{21} & \mathbf{K}'_{22} \end{bmatrix}, \tag{7}$$

where

$$\mathbf{K}'_{11}=\begin{bmatrix} k_n & 0 & 0 & 0 & 0 & 0 \\ 0 & k_t & 0 & 0 & 0 & k_t d_0 \\ 0 & 0 & k_t & 0 & -k_t d_0 & 0 \\ 0 & 0 & 0 & \kappa_n & 0 & 0 \\ 0 & 0 & -k_t d_0 & 0 & \kappa_t + k_t d_0^2 & 0 \\ 0 & k_t d_0 & 0 & 0 & 0 & \kappa_t + k_t d_0^2 \end{bmatrix},$$

$$\mathbf{K}'_{12}=\left(\mathbf{K}'_{21}\right)^{\mathrm{T}}=\begin{bmatrix} -k_n & 0 & 0 & 0 & 0 & 0 \\ 0 & -k_t & 0 & 0 & 0 & k_t d_0 \\ 0 & 0 & -k_t & 0 & -k_t d_0 & 0 \\ 0 & 0 & 0 & -\kappa_n & 0 & 0 \\ 0 & 0 & k_t d_0 & 0 & k_t d_0^2 - \kappa_t & 0 \\ 0 & -k_t d_0 & 0 & 0 & 0 & k_t d_0^2 - \kappa_t \end{bmatrix},$$

$$\mathbf{K}'_{22}=\begin{bmatrix} k_n & 0 & 0 & 0 & 0 & 0 \\ 0 & k_t & 0 & 0 & 0 & -k_t d_0 \\ 0 & 0 & k_t & 0 & k_t d_0 & 0 \\ 0 & 0 & 0 & \kappa_n & 0 & 0 \\ 0 & 0 & k_t d_0 & 0 & k_t d_0^2 + \kappa_t & 0 \\ 0 & -k_t d_0 & 0 & 0 & 0 & k_t d_0^2 + \kappa_t \end{bmatrix}.$$

The first step in putting together the global stiffness matrix is to perform the coordinate transformation on the stiffness matrices ($\mathbf{K}'_{11},\ \mathbf{K}'_{12},\ \mathbf{K}'_{21},\ \mathbf{K}'_{22}$) of the constructed beam element. Each block of the stiffness matrix must be transformed into its tensorial form for coordinate transformation, thus the 6×6 blocks of stiffness matrix must first turn into $3\times 3\times 3\times 3$ fourth-order tensorial form (K'_{ijkl}). Each one of these tensors must be subjected to coordinate transformation using the following equation:

$$\mathrm{K}'_{ijkl}=R_{im}R_{jn}R_{kp}R_{lq}\mathrm{K}'_{mnpq},\quad \mathbf{R}=\mathbf{R}_z(\psi)\mathbf{R}_y(\phi)\mathbf{R}_x(\theta), \tag{8}$$

where ψ, ϕ, and θ are the angles between beam element and x, y, and z global coordinate system, moreover $\mathbf{R}_x$, $\mathbf{R}_y$, and $\mathbf{R}_z$ are rotation matrices. The global stiffness matrix may be constructed after coordinate transformation by integrating every block of the local stiffness matrix into its appropriate location in the global stiffness matrix. By subjecting the assembly to

displacement or tractional boundary condition, the displacement of every particle within the aggregate can be obtained by inversing the global stiffness matrix and multiplying it with global force vector $(\mathbf{U} = \mathbf{K}^{-1}\mathbf{F})$.

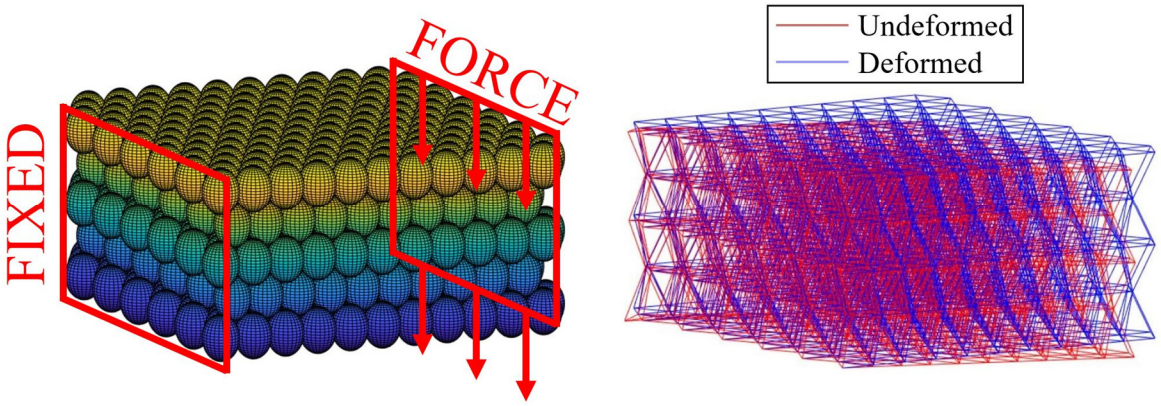

Figure 21: Powder bed subjected to displacement and traction B.C. (left), and isometric view (middle) and XZ view (right) of deformed and undeformed generated spaceframe structure.

In this dissertation, a fully packed 3D structure has been used to simulate structurally determinant powder bed packing. In order to generate a fully packed structure first, a fully packed 2D structure of uniform circular particles with a radius less than the desired average radius of the particle was generated then the second layer of powders could be generated by connecting the centers of adjacent particles in the first layer and constructing 2D triangular elements. Consequently, particles in the second layer may be generated in the center of the triangle element. The following layers of powder particles could be created simply by duplicating the positions of the particles from the first and second layers that had previously been created.

Each powder particle in the generated fully packed structure barely touches its adjacent particle; Although these particles are not yet sintered together, therefore, the beam element could not be constructed between them. The radius of each particle in the fully packed structure was raised randomly between 5 and 14 percent of the radius of each particle in order to generate a

realistic representation of sintered particles. The increase in powder radii could not be set higher than 14 percent since it would cause the stiffnesses of beam elements (Eq. 3 to Eq. 6) to turn into complex numbers $(a^* > 1)$. To guarantee that these fully packed models closely mimic the sintered AM structure, the position of each powder particle randomly changes within a small cubic box where the center of these cubic boxes is at the center of each displaced particle within the manufacturing domain, and each side of these boxes is $l = 2.05R_i$.

In order to model the geometry of the final manufactured structure, the fully packed structure is generated first, followed by the elimination of powders that are not inside the prescribed scanning path of the laser. Figure 22 illustrates the laser scanning path on the AM structure; the red region is densely packed with particles, while the white space is empty of particles. The average radius of the spherical particle is set to be 12.5 μm.

The definition of continuum mechanical state variables *stress* and *strain* tensors are not self-evident in SLS manufactured structure due to the stochastic nature. There are different approaches to find a theoretical definition of state variables based on grain displacements, local geometrical characteristics, and forces transmitted between contacting particles. In this dissertation, the average stress and strain in the DEM simulation is calculated using the Katalin Bagi [139]-[140] definition of state variables in a granular assembly.

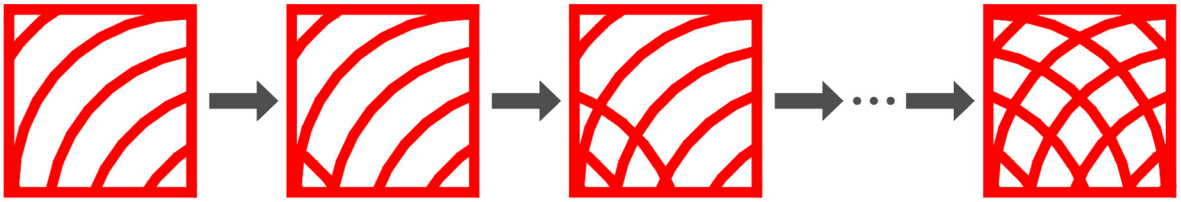

Figure 22: Schematic of the laser scanning path.

Bagi discretized the unit normal vector in the Gauss-Ostrogradski equation using the

material cell system and *space cell system* concepts and derived the average of displacement gradient tensor as follows:

$$\bar{e}_{ij} = \frac{1}{V}\iiint_{(V)} e_{ij}dV = \frac{1}{V}\iint_{(S)} u_i n_j dS = \frac{1}{V}\sum_{m<n} \Delta u_i^{mn} d_j^{mn}, \tag{9}$$

where V is the volume of the tetrahedral structure created by the beam elements. and $\Delta u_i^{mn} = u_i^m - u_i^n$ is the relative displacement vector between each pair of particles as determined by the established force-displacement model, and d_j^{mn} is the *complimentary area vector* which is defined as follows:

$$d_i^{mn} = \frac{1}{4}\sum_{t=1}^{T}\left(a_i^{m(t)} - a_i^{n(t)}\right), \quad a_i^k = -\frac{1}{3}b_i^k, \tag{10}$$

where the beam element is built between the centers of the two powder particles m and n, which have been sintered together. After generating the beam elements, to compute the complimentary area vector, the tetrahedral (space cells) that include edge mn must be collected. In Eq. 10, T is the number of collected tetrahedral for edge mn and b_i^k is a vector that corresponds to each four-face of every tetrahedron that has been collected (the number of b_i^k vector for edge mn would be equal to $4T$). For example, three tetrahedral sounding the edge mn (i.e., $T = 3$) in Figure 23. The magnitude of b_i^k vector is equal to the area of its corresponding face and the direction of this vector is normal to the face and pointing outward. The symmetric part of the displacement gradient would be the strain tensor.

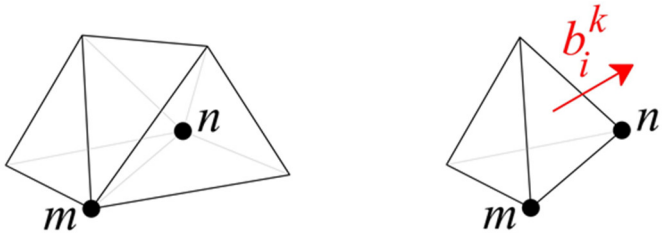

Figure 23: Schematic of three tetrahedral between six sintered particles (left), and the b_i^k (right).

The Cauchy stress tensor for granular material with volume V may be expressed as the sum of the dyadic product of particles contact forces f_i^c and the branch vector$\left(l_j^c = x_j^m - x_j^n\right)$ as follows:

$$\bar{\sigma}_{ij} = \frac{1}{V}\iiint_{(V)} \sigma_{ij} dV = \frac{1}{V}\sum_{b\in B} f_i^b x_j^b = \frac{1}{V}\sum_{c\in V\cup B} f_i^c l_j^c, \tag{11}$$

where b is the number of particles exposed to external loading, and b is the number of powder particle connections. Six independent experiments for the same structure with different boundary conditions must be carried out to determine the effective elastic constants [141]. The effective compliance matrix $\mathbf{S}^{\text{eff}}$ can be defined as follows:

$$\bar{\boldsymbol{\varepsilon}} = \mathbf{S}^{\text{eff}}\bar{\boldsymbol{\sigma}} \tag{12}$$

The six general elastic properties (E_x, E_y, E_z, ν_{yz} , ν_{zx} , ν_{xy}) can be obtained from elements of the compliance matrix.

4.2 Developing Dataset for the Convolutional Neural Network Model of Effective Elastic Properties of Powder Beds

The proposed method for evaluating effective elastic properties of SLS manufactured structures is too slow to develop a real-time system capable of predicting aggregate elastic properties at any step of the manufacturing process. In this section of Chapter 4, a novel CNN regression technique is presented as an alternate method for the evaluation of effective elastic properties of SLS manufactured structures. In this approach, the time-consuming DEM is used for CNN training purposes and not at run time. The convolutional layers of the proposed CNN model can extract local patterns of the image representation of powder beds; thus, CNN attempts to extract wider global patterns from these image representations by stacking multiple convolutional layers in a hierarchical fashion. The first step for implementing the CNN for evaluation of effective elastic properties of powder beds is to collect and create a dataset that includes hundreds of image

representations of AM structures as well as their elastic properties ($E_x, E_y, E_z, \nu_{yz}, \nu_{zx}$, ν_{xy}).

By discretizing the AM structure with small uniform cuboid boxes and computing the fraction of the volume of each box filled with powders particle to the overall volume of the box, an image representation of powder-based AM structure could be obtained. For instance, A structure with a 3 mm × 3 mm base and three layers of powder may be discretized using a 0.03 mm × 0.03 mm × 0.1 mm cuboid, resulting in a 100 by 100 2D array of numbers (image representation of powder bed). Each element of the generated 2D array of numbers would be numbers ranging from 0 (empty cell) to 1 (cell packed with the solid material). A time-consuming DEM simulation would be used to label each of these AM structures with their associated effective elastic properties.

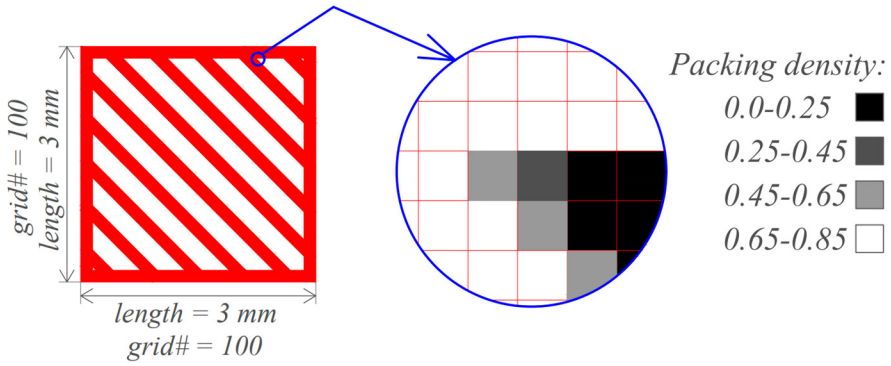

Figure 24: The pixilation process to present the powder-based AM structure with a 2D array of numbers.

4.3 Prediction of the Effective Elastic Properties of Powder Beds Using Deep Convolutional Neural Network Model

In conventional CNN architectures, the FC layers are the last layer of the DL model [142]. All of the neurons in the FC layers are linked to all of the output of the preceding layer. Because of this full connection between input and output, the CNN model could thoroughly mix the flow of information between the input and output of the FC layer. As a result, the final output of the CNN model would be based on the whole inputted image representation of the powder bed. In the Conventional CNN model for multi-classification tasks, the last FC layer (output layer) would use

a SoftMax activation function that computes the probabilities of each class according to its mathematical description. This implies that when the SoftMax activation function is used, the sum of all output values equals one, and the values represent the level of confidence in the specific class [42]. Although, the aim of this chapter of the dissertation is to estimate the six independent, effective elastic properties of the image representation of the SLS manufactured structures using the CNN model. Therefore, the classifier output layer of the conventional CNN model is replaced with a multiple output regression layer. For a CNN model with T distinct outputs, all T regression tasks share the same input image representation of SLS manufactured structure from N input pixelated AM structures $\{x_i\}_{i=1}^{N}$, each distinct regression task could be label as $\{\{y_i^t\}_{i=1}^{N}\}_{t=1}^{T}$. The N and T could be set to be the number of batches of image representation of AM structure that feed into the CNN model and six corresponding to six independent effective elastic properties of AM structure, respectively. The mean squared error loss function of the multiple output CNN regressor model may be stated as follows, assuming each regression task has the same importance:

$$J(W,b)=\frac{1}{N}\sum_{i=1}^{N}\sum_{t=1}^{T}\left(y_i^t-\hat{y}_i^t\right)^2 \tag{13}$$

where $\hat{y}_i^t$ is the output of t-th regression task for i-th SLS manufactured structure. Moreover, W and b are the weight and bias parameters of filters and FC layers for the entire CNN model, respectively, which must be learned via the backpropagation procedure.

The proposed multiple-output regression output layer replaced the output layer of several well-known deep CNN architectures for the multi-classification problem, including AlexNet [143], LeNet-5 [144], and VGG Net [145], and the modified architecture was trained using the generated dataset. These modified networks are backpropagated on proposed loss (error between predicted and actual effective elastic properties of SLS manufactured structure) and optimized using an

adaptive moment estimation (Adam) algorithm. The original dataset is randomly divided into 1600 training and 400 validation examples. All hyper-parameters were left at their default values in the Keras API except for the batch size, which was adjusted to 100 training samples each iteration.

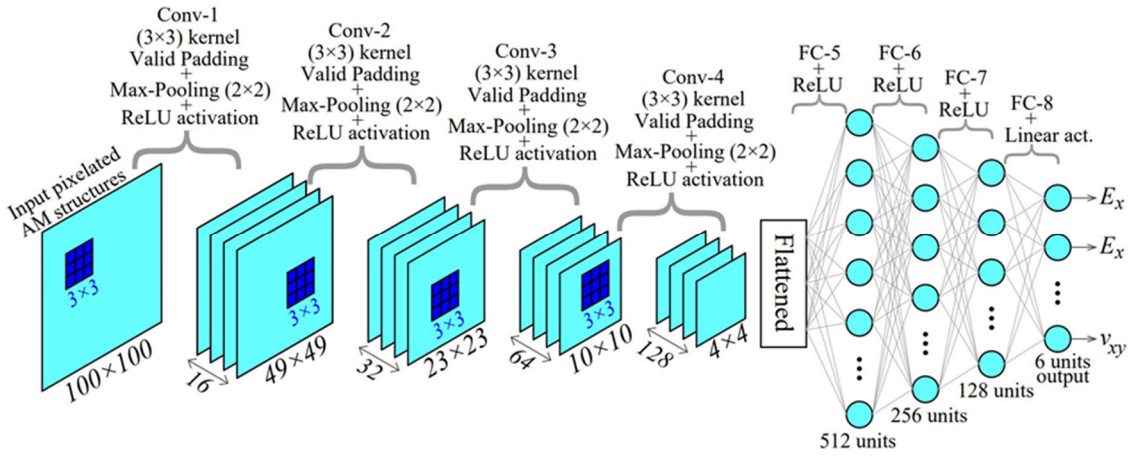

Figure 25: The CNN architecture of the proposed Custom Net to predict the effective elastic properties of the SLS manufactured structure.

The training accuracy of the modified AlexNet, LeNet-5, and VGG Net CNN architecture after only 80 epochs is 92.5, 90.6, and 18.1 percent, respectively. While the MSE loss function is minimized for optimization of weight and biases in the DL model, the accuracy metric here is the average of the ratio of the absolute error to the evaluated value with the physics-based simulation for every six effective elastic properties of every example in the training set (training accuracy) and validation set (validation accuracy). Despite having a large number of trainable parameters (65.07 million), the accuracy of VGG Net architecture is severely low for the prediction of the effective elastic properties of powder bed given the pixelated SLS manufactured structure. The poor accuracy of the modified VGG Net architecture may be due to vanishing gradient problems in extremely deep neural networks model or the limited number of training examples [146]. The AlexNet architecture with 20.31 million and LeNet-5 architecture with only 59 thousand trainable parameters substantially outperform the VGG Net architecture. Even though AlexNet has fewer

trainable parameters than VGG Net, the forward propagation procedure for an unseen SLS manufactured structure may be too slow for a real-time system capable of sub-second prediction of the effective elastic properties of AM structure. Furthermore, the computational time of the forward propagation procedure of the LeNet-5 CNN architecture is way lower than AlexNet; however, it is less accurate. In this section of the dissertation, a novel CNN architecture called Custom Net is presented and well optimized to evaluate the effective elastic properties of the SLS manufactured structure to achieve high accuracy and acceptable computational efficiency.

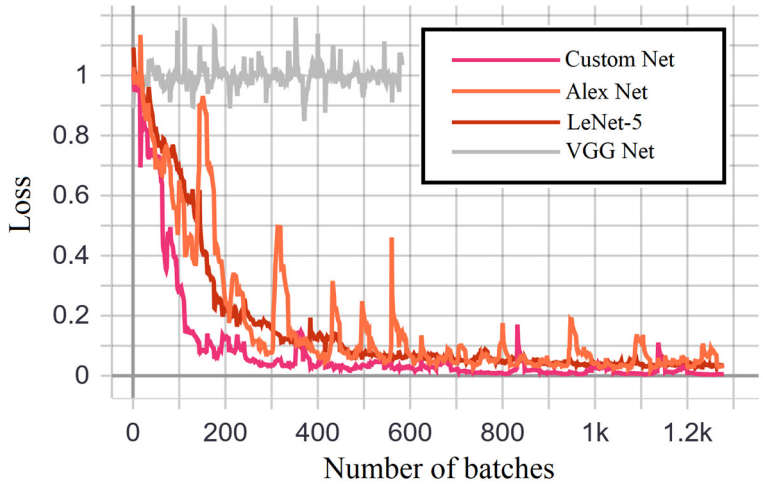

Figure 26: Loss versus the number of batches of data for AlexNet, LeNet-5, VGG Net, and proposed Custom Net.

As illustrated in Figure 25, The Custom Net is made up of four stacks of convolutional operations, ReLU activation function, and pooling operation, which are followed by four FC layers at the end of the CNN architecture. The ReLU activation function is used in the three hidden FC layers, while the final FC layer employs the multiple output regression layer. The number of Channels gradually rises from 16 in Conv-1 to 128 in Conv-4, and all convolutional (Conv) layers have the same 3×3 kernels. A 2×2 filter is used in every Max-Pooling operation, and the number of units in FC layers decreases from 512 units in FC-5 to 128 units in FC-7. The Custom Net was trained using the same optimizer and hyper-parameters as the three modified well-known

deep CNN architectures.

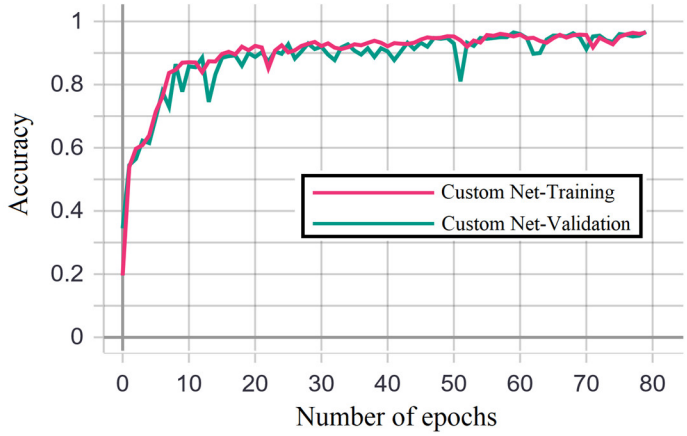

Figure 27: Training and validation accuracy for proposed Custom Net versus the number of epochs.

The proposed Custom Net has 1.31 million trainable parameters, which is considerably less than the modified VGG Net and AlexNet parameters; as a result, the forward propagation process for an unseen SLS manufactured structure in Custom Net is faster than the other two networks. The loss against the number of batches of data fed into each of the four mentioned CNN architectures is shown in Figure 26. One can see that Custom Net converged quicker than the other three CNN architectures, and Custom Net is more accurate than Alex Net and LeNet-5 after 1200 batches of training examples. Figure 27 shows the training and validation accuracy of Custom Net against the number of epochs. The Custom Net achieved 96.5 percent accuracy on the training set and 96.1 percent accuracy on the validation set after getting trained for less than 100 epochs. Because the difference between training and validation accuracy is relatively small, the further overfitting prevention methods (dropout, regularization, and data augmentation) are unnecessary.

Custom Net takes 32 minutes to get trained using the developed dataset, and it takes an average of 37.24 milliseconds for Custom Net to estimate the effective elastic properties of an unseen SLS manufactured structure. The computational time for the prediction of effective elastic

properties of Custom Net is significantly shorter compared to the DEM model which could take up to 6 hours and 34 minutes for a powder bed with large number of particles.

4.4 Numerical Examples for the Evaluation of the Data-Driven Model of the Effective Elastic Properties of Powder Beds

In this section, the described DEM model for evaluation of effective elastic properties of SLS manufactured structure is used to generate the dataset, and Custom Net CNN architecture used for sub-second prediction of the same effective elastic properties. The material properties of the powder particle that was developed to generate the dataset are given in the Table 3.

Table 3: Material properties of powder particles [18].

Property	Value
Particle mean radius (R_i)	12.5 μm
Density(ρ_i)	7800 Kg/m^3
Young's modulus (E_i)	210 (Gpa)
Poisson's Ratio	0.28

For 400 distinct unseen image representations of SLS manufactured powder bed structures, Figure 28 and Figure 29 compare the effective modulus of elasticity (E_x, E_y) evaluated using the DEM technique with their corresponding predicted values using the proposed CNN method. One can see that as the packing density of the powder bed structures increases, the effective modulus of elasticity increases as well. Moreover, as the packing density increases, the standard deviation of effective Young's modulus in both directions increases because the powder particles would fuse more into each other; Hence, the difference between the normal and tangential stiffnesses in each beam element within the AM structure would increase accordingly. An excellent agreement between the effective modulus of elasticity evaluated with DEM technique and predicted with

CNN model can be seen in all cases. The computational time of CNN model for evaluating the effective elastic properties of these 400 examples is only 0.0005 percent of the time needed for solving the problem using DEM model.

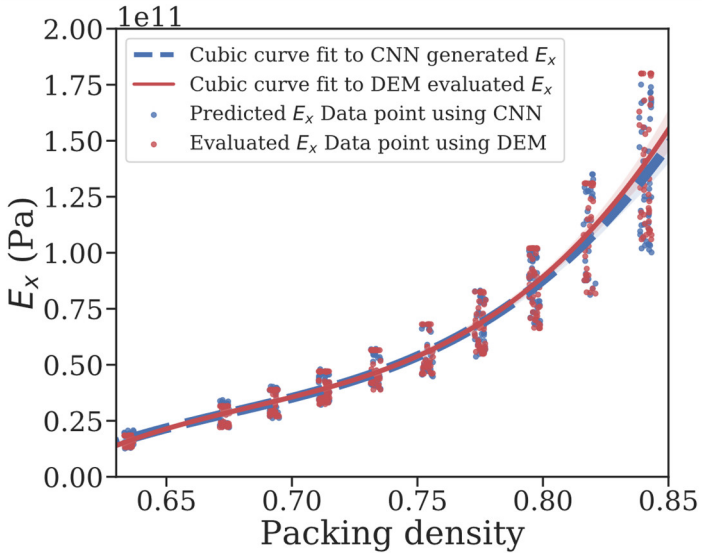

Figure 28: Scatterplot of DEM evaluated and CNN predicted E_x versus the packing density of unseen powder beds. The cubic fit to DEM evaluated, and CNN predicted values is also included.

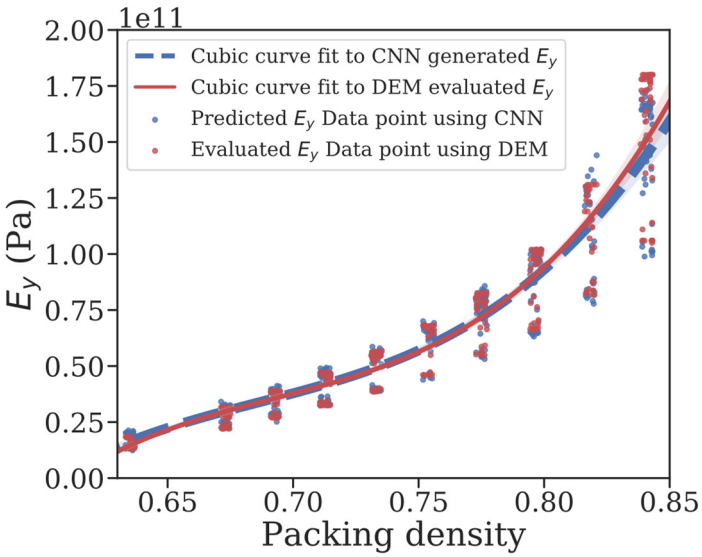

Figure 29: Scatterplot of DEM evaluated and CNN predicted E_y versus the packing density of unseen powder beds. The cubic fit to DEM evaluated, and CNN predicted values is also included.

For the same 400 AM structures, Figure 30 and Figure 31 compare the effective Poisson's

ratio (ν_{zx} , ν_{xy}) evaluated using the time-consuming DEM method and their corresponding predicted values using the sub-second CNN method. Figure 30 and Figure 31 show that an increase in packing density does not always result in an increase in effective Poisson's ratio.

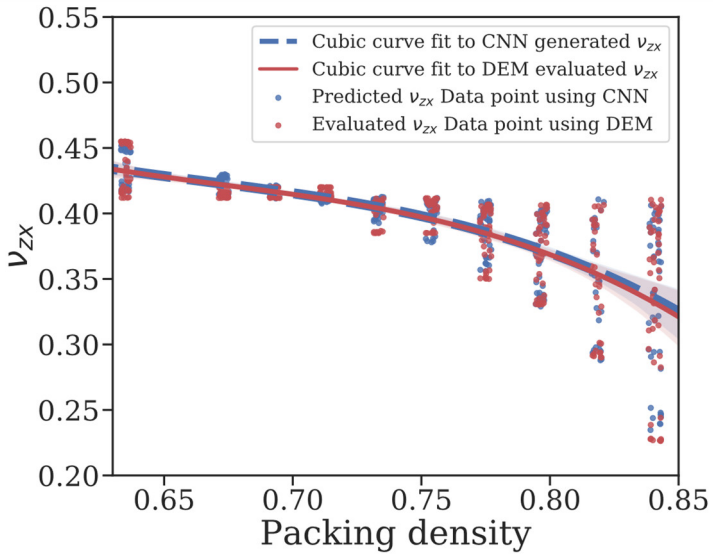

Figure 30: Scatterplot of DEM evaluated, and CNN predicted E_y versus the packing density of unseen powder beds. The cubic fit to DEM evaluated, and CNN predicted values is also included.

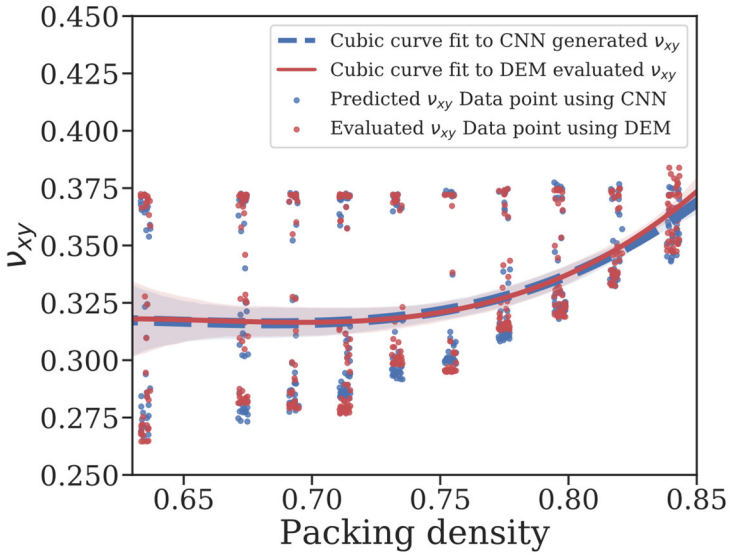

Figure 31: Scatterplot of DEM evaluated, and CNN predicted E_y versus the packing density of unseen powder beds. The cubic fit to DEM evaluated, and CNN predicted values is also included.

Chapter 5. Evaluation of Force-Displacement Behavior of the Elastoplastic Impact of Dissimilar Bodies Using Artificial Neural Network

The use of computational models such as DEM for simulation of the interactions of granular materials with each other and the environment has grown dramatically in the past few decades. This is especially the case in the modeling and simulation of AM processes [4]-[18], pharmaceutical manufacturing processes [147], and the operations involved in mineral processing [148]. Discrete Element Method simulations can provide extensive information on system dynamics by tracking the motion of each particle within the domain of study. For practical simulations with a large number of particles, however, DEM may become expensive and time-consuming. Material body contact models are essential for the simulation of granular systems with the DEM technique since they allow the evaluation of contact forces and displacements during the collision process [147]. The highly complicated contact and impact mechanics models could further increase the computational cost of DEM simulations for granular systems comprising thousands of particles [149]. Vu-Quoc and Zhang [150], Li *et al.* [151], and Thornton [152] developed accurate nonlinear collision models that are computationally expensive since multiple iterations are required to analyze the force-displacement behavior throughout the collision process. Renzo and Maio [153] looked into the effect of several different force-displacement models on the accuracy of collision simulation. The Renzo and Maio study of the development of force, displacement, and velocity throughout the collision process shows the significance of utilizing a complicated nonlinear collision model in the assessment of contact force and micro-slip effect in DEM simulations.

Several methods have been proposed in the literature to reduce the computing costs of the

use of nonlinear collision models in DEM simulations. For example, in order to reduce the computational time associated with DEM modeling of ball mill operation, Mishra and Murty [148] proposed an equivalent linearization technique to convert the nonlinear contact model to a simple linear model. To reduce the computational time of numerical models of contact, Boos, and McPhee [154] proposed a volumetric model of contact with relatively large contact surfaces, in which forces are expressed in terms of the properties of the volume of interference between the solid geometries of the bodies in contact. The more primitive method to reduce the computational time of the DEM model is scaling up the particle size, reducing the number of parameters in simulation, or adjusting some of the contact parameters [147].

The characterization of granular flow and rigid body dynamic analysis with many particles requires a deep understanding of the inelastic impact physics and complex force-displacement behavior of the colliding bodies during the collision process. Based on their recently developed nonlinear constitutive relation, Stronge, Sofi, and Ravani [36] developed a fairly simple nonlinear lumped parameter model for the elastoplastic impact to analyze the force-displacement behavior of colliding bodies with different material and geometrical properties. Their lumped parameter model utilizes the relatively time-consuming Newton-Raphson iterative algorithm to solve the nonlinear equations and accurately evaluate the compliance behavior of colliding bodies. However, implementing this time-consuming Newton-Raphson algorithm could significantly slow down the simulations with a large number of particles colliding against each other. This chapter briefly reviews their physics-based model of Stronge, Sofi, and Ravani [36] and presents a newly developed data-driven ANN model to predict the normal force-displacement behavior of colliding bodies much faster than the physics-based simulation. The Newton-Raphson iterative algorithm [36] is used to develop a dataset including more than ten thousand compliance curves for colliding

bodies with different material and geometrical properties and various relative impact velocities. This dataset is utilized for training an ANN model capable of sub-second compliance curve prediction based only on the material and geometrical properties of the colliding bodies and their relative impact velocities.

5.1 Physics-Based Simulation of Elastoplastic Impact of Dissimilar Bodies

To characterize the material compliance of each colliding body throughout the indentation phase, Stronge, Sofi, and Ravani [36] used the following strain-hardening constitutive relation:

$$\frac{\sigma_i}{Y_i} = \left(\frac{E_i \varepsilon_i}{Y_i} \right)^{1/n_i}, \tag{14}$$

where σ_i and ε_i are stress and strain experienced by the *i*th colliding body (*i*=1, 2); $E_i, Y_i,$ and n_i are the Young's modulus, yield strength and strain-hardening coefficient of the *i*th body. For piecewise evaluation of force-displacement behavior of the colliding bodies, the strain-hardening is set to be $n_i = 1$ for the elastic region $(\sigma_i \leq Y_i)$ and $n_i > 1$ in the plastic region $(\sigma_i > Y_i)$. Using Johnson strain-indentation relation [155] and assuming the contact area between colliding bodies to be circular with radius *a*, Stronge, Sofi, and Ravani [36] expanded the Eq.14 as follow:

$$\frac{\delta_i}{a} = \frac{Y_i}{E_i} \left(\frac{F}{\pi a^2 Y_i} \right)^{n_i}, \tag{15}$$

where δ_i is the indentation of *i*th colliding body, and F is the mutual contact force between the two colliding bodies during the indentation phase of the collision. Hill [156] *et al.* provides the following relationship between the radius of colliding bodies and increasing contact radius between the two materials during the indentation process:

$$c_i = a^2 / (2R\delta_i), \tag{16}$$

where *R* is an effective curvature $(R^{-1} = R_1^{-1} + R_2^{-1})$, and c_i is a constant that depends on the

strain-hardening coefficient. To evaluate c_i value for the spheroidal contact Stronge, Sofi, and Ravani [36] used the following equation developed by Storåkers *et al.* [157]:

$$c_i = \sqrt{2}\exp(-1/n_i). \tag{17}$$

The following force-displacement relation for each colliding body during the indentation period is obtained by substituting Eq. 16 into Eq. 15 as follows:

$$\frac{\delta_i}{R} = \left(2c_i\right)^{\frac{1-2n_i}{1+2n_i}} \left(\frac{Y_i}{E_i}\right)^{\frac{2}{1+2n_i}} \left(\frac{F}{\pi R^2 Y_i}\right)^{\frac{2n_i}{1+2n_i}}. \tag{18}$$

Stronge, Sofi, and Ravani [36] assumed that both colliding bodies would behave elastically during the restoration phase. As a result, they used the Hertzian contact equation to evaluate the force-displacement behavior of colliding bodies during the restitution period as follows:

$$\frac{F}{\pi \bar{R}_i^2 E_i} = \left(\frac{4}{3\pi}\right)\left(\frac{\delta_i - \delta_{if}}{\bar{R}_i}\right)^{3/2}, \tag{19}$$

where $\bar{R}_i$, and δ_{if} are, respectively, the unloaded effective surface curvature, and the unloaded indentation of *i*th colliding body. The displacement in terms of force and initial radius of curvature (R) during the restitution phase can be developed from Eq. 19 as follows:

$$\frac{\delta_i - \delta_{if}}{R} = \left(\frac{R}{\bar{R}_i}\right)^{1/3} \left(\frac{Y_2}{E_i}\right)^{2/3} \left(\frac{F}{\pi R^2 Y_2}\right)^{2/3}. \tag{20}$$

Figure 32 illustrates the complex elastoplastic impact process of two dissimilar colliding material bodies where the force-displacement relation from the beginning of the collision process up to the point of maximum compression and from that point to the complete separation of two colliding material bodies can be evaluated, respectively, by Eq. 18 and Eq. 20. From Eq. 16, Eq. 18, and Eq. 19 at the point of maximum compression, Stronge, Sofi, and Ravani [36] developed the following equation for evaluation of effective surface curvature:

$$\frac{\bar{R}_i}{R}=\left(\frac{4}{3\pi}\right)(2c_i)^{\frac{3}{1+2n_i}}\left(\frac{Y_i}{E_i}\right)^{\frac{-2(n_i-1)}{(1+2n_i)}}\left(\frac{Y_2}{Y_i}\right)^{\frac{n_i-1}{1+2n_i}}\left(\frac{F_c}{\pi R^2 Y_2}\right)^{\frac{n_i-1}{1+2n_i}}, \tag{21}$$

where F_c is the maximum normal force and Y_2 is yield stress of the initially softer body. The maximum normal force could be evaluated from maximum indentation (δ_{ic}) by setting the force and indentation in Eq. 18 (F and δ_i) to maximum normal force and maximum indentation (F_c and δ_i). By evaluating the work done by the normal component of contact force on both colliding material bodies from the beginning of the indentation period up to the point of maximum compression and equating it with the initial kinetic energy of normal relative motion, Strong, Sofi, and Ravani [36] derived the following expression for the maximum indentation (δ_{ic}) during the inelastic impact of dissimilar colliding bodies:

$$\frac{\delta_{ic}}{R}=\left(\left(\frac{1+4n_i}{2n_i}\right)\frac{M_i\left(v_i(0)\right)^2}{2\pi R^3 Y_i}\right)^{\frac{2n_i}{1+4n_i}}(2c_i)^{\frac{1-2n_i}{1+4n_i}}\left(\frac{Y_i}{E_i}\right)^{\frac{2}{1+4n_i}} \tag{22}$$

where M_i and $v_i(0)$ are the mass and the initial normal velocity relative to the center of momentum frame of reference of the *i*th colliding body, respectively. Finally, Stonge, Sofi, and Ravani [36] evaluated the unloading indentation δ_{if} of *i*th colliding body as follows:

$$\delta_{if}/\delta_{ic}=1-2c_i R/\bar{R}_i \tag{23}$$

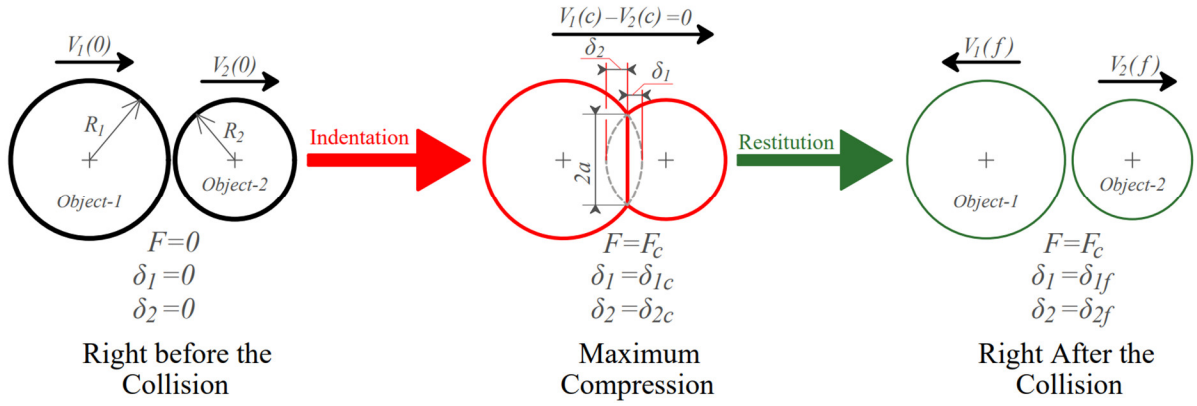

Figure 32: The process of collision between two dissimilar bodies including.

Stronge, Sofi, and Ravani analyzed the compliance behavior of each colliding material body by modeling the contact region of two colliding bodies as two nonlinear springs (see Figure 33). The stiffness of these nonlinear springs will behave differently in each phase of the collision since the force-displacement equations for indentation and restitution phases are different. Stronge, Sofi, and Ravani obtained two separate expressions for the stiffnesses of the nonlinear springs associated with each colliding body during indentation and restitution periods. They rearranged the Eq. 18 and Eq. 20 to obtain the relationship between force and displacement and then taking the derivative of the obtained equations with respect to the displacement. The resulting stiffnesses for indentation and restitution are as follows:

$$k_{i-\text{indent}} = \pi R^2 Y_i \frac{1+2n_i}{2n_i} (2c_i)^{\frac{2n_i-1}{2n_i}} \left(\frac{E_i}{Y_i}\right)^{\frac{1}{n_i}} \left(\frac{1}{R}\right)^{\frac{1+2n_i}{2n_i}} \delta_i^{\frac{1}{2n_i}}, \tag{24}$$

$$k_{i-\text{rest}} = \frac{3}{2}\pi R E_i \left(\frac{\bar{R}_i}{R}\right)^{1/2} \left(\frac{\delta_i - \delta_{if}}{R}\right)^{1/2}, \tag{25}$$

Having the stiffness of springs associated with each colliding body during indentation and restitution, the normal force-displacement relation during the collision process could be easily evaluated for each colliding material bodies using Hooke's law $(\delta_i = F_i/k_i)$, and the total displacement could be evaluated as:

$$\delta_{total} = \delta_1 + \delta_2 = \frac{k_1 + k_2}{k_1 k_2} F, \tag{26}$$

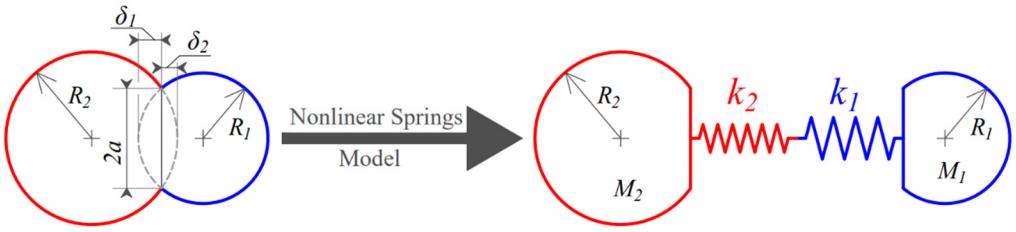

Figure 33: The nonlinear spring lumped parameter model of the elastoplastic impact of dissimilar bodies.

Stronge, Sofi, And Ravani developed a nonlinear simulation based on the numerical solution of the force-displacement equation of nonlinear springs allocated to each colliding body. They first linearly increased the load from zero to maximum contact force (F_c) and then linearly decreased it to reach zero again. For each segment of the piecewise variation in the value of the force, a Newton-Raphson iterative algorithm was implemented to solve the nonlinear problem. Stronge, Sofi, And Ravani validate the accuracy of their piecewise nonlinear lumped parameter model of the impact by comparing their result to a more detailed analysis by Vu-Quoc and Zhang [32] as well as experimental results of Brake [158]. Therefore, their results are considered in this dissertation as the ground truth label for predicting the force-displacement behavior of elastoplastic impact of dissimilar colliding bodies using the ANN model.

5.2 Developing Dataset for Artificial Neural Network Model of Elastoplastic Impact

Gathering and preparing a dataset with thousands of pairs of material bodies with similar and dissimilar materials and geometrical properties colliding against each other with various relative impact velocities is an essential step toward developing an ANN model for predicting force-displacement behavior in an elastoplastic impact of dissimilar colliding bodies. In developing this dataset for evaluating the force-displacement behavior of each pair of mentioned colliding bodies, the Newton-Raphson algorithm was called 200 times for each simulation (100 times for indentation and 100 times for each simulation restitution). The material properties of the colliding bodies used in the impact simulations conducted to generate the dataset needed for ANN training are listed in Table 4. The selected range of radius and relative impact velocities used in these physic-based simulations are between 25 to 320 μm and 0.009 to 0.2 m/s, respectively.

The final dataset developed in this dissertation includes over 10,000 pairs of colliding bodies with identical and differing materials, variable radius values for each colliding body, and

varying relative impact velocities. Each Newton-Raphson algorithm could converge with a different number of iterations; therefore, the overall number of force-displacement points generated in each example for the evaluation of the compliance curve was different. Therefore, further data integration process was needed before training the DL model. To develop a dataset with the same number of force-displacement points, first, the maximum number of these points for a single example throughout the dataset was found. Subsequently, for each example with a lower number of force-displacement points, the last point was repeated until its number of force-displacement points was equal to the maximum number of points determined earlier. All input and output features in the dataset, including the material and geometrical properties of each colliding material body, relative impact velocity, as well as obtained force and displacement from the physics-based simulation, were scaled by the minimum and range of that particular feature. The scaling was done to make all elements lie between zero and one, bringing all numeric column values in the dataset to a single scale.

Table 4: Material properties of some steel and aluminum alloys, tungsten, polyethylene [159]-[160]-[161]-[162].

Material	Density (Kg/m^3) ρ_i	Young's modulus (Gpa) E_i	Yield stress (MPa) Y_i	Hardness modulus n_1
Aluminum (1050 annealed)	2700	65	30	5.5
Aluminum (1050 work hardened)	2700	69	35	5.0
Aluminum (5754-0)	2700	70	96	4.5
B Steel (C = 0.21%)	7800	212	487	12.0
SK5 Steel (C = 0.87%)	7800	207	600	8.7
Tungsten	19300	400	750	1
Polyethylene	950	0.85	27.5	3.4

The final goal of the data-driven model of elastoplastic impact is to develop an ANN model

to quickly map the relative impact velocity, material properties, and radius of both colliding bodies to a set of force-displacement points that can accurately describe the compliance behavior of these colliding bodies. Since Stronge, Sofi, and Ravani [159] only studied the compliance curve of the initially softer body $(Y_2 \leq Y_1)$, the developed dataset only records the force-displacement behavior of the initially softer body as well. Furthermore, to reduce the complexity of the ANN model, only 45 points on the compliance curve of each collision scenario simulated with the Newton-Raphson algorithm have been selected for ANN training purposes.

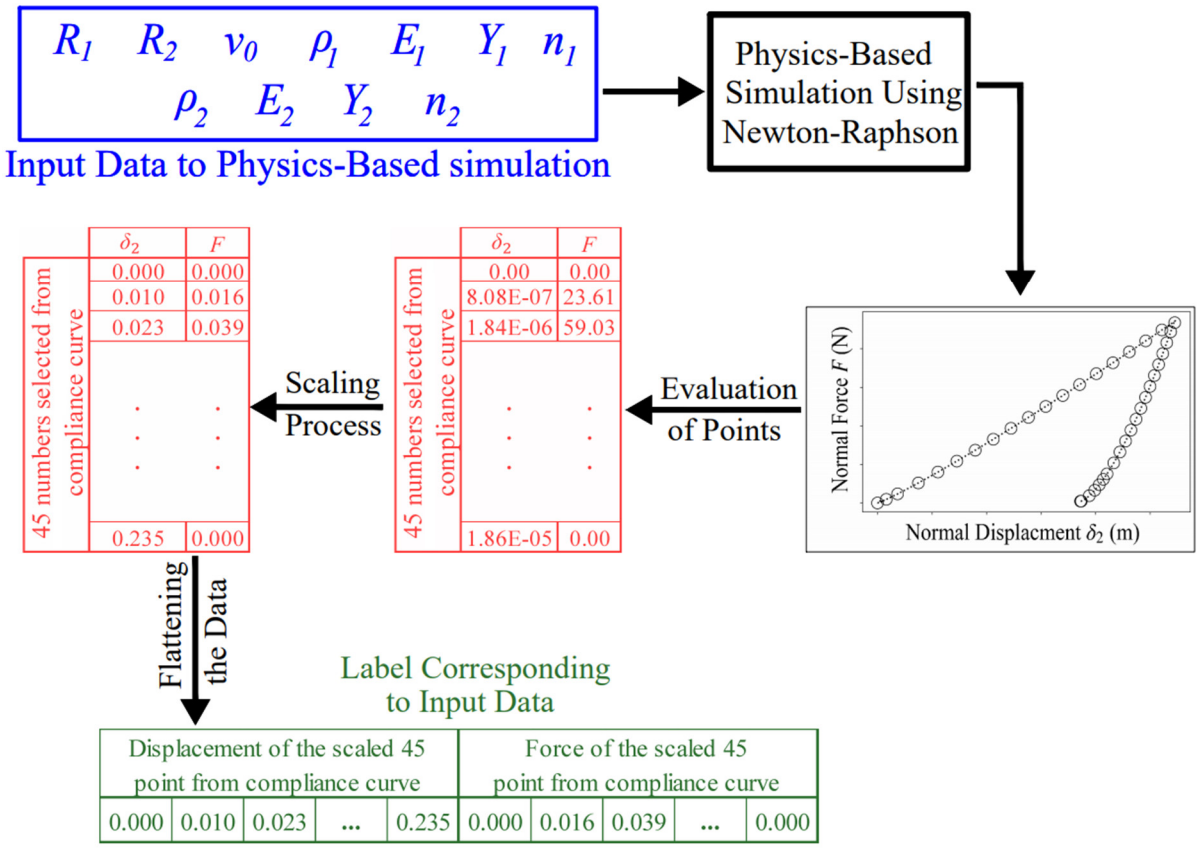

Figure 34: Procedure of labeling relative impact velocity the material properties and geometrical properties associated with a particular collision scenario with 90 numbers corresponding to 45 force-displacement points.

These 45 points include several points on the indentation phase and several points on the

restitution phases of the compliance curve. These points are selected with equal space with respect to force-displacement data points from initially integrated data. After the scaling process, the output data is flattened to build a 1D array of numbers with 90 elements where the first 45 elements are the displacements, and the following 45 elements are their corresponding forces associated with the compliance curve evaluated by the physics-based simulation. Figure 34 illustrates the procedure of labeling the input data by the physics-based simulation with 90 numbers.

5.3 Training Process and Architecture of the Artificial Neural Network Model for Prediction of Force-Displacement Behavior of Colliding Material Bodies

The architecture and training process of the DL model for predicting the compliance curve of the initially softer body in collisions between dissimilar bodies made of strain-hardening materials are described in depth in this section. The created dataset in the last section of this chapter is utilized for training a deep ANN model, which decreases the computing time of the physics-based simulation from several seconds to a fraction of a second. Based on the developed dataset, the deep ANN model is expected to predict 45 independent displacements of the originally softer colliding body and their associated 45 independent force variables based on the produced dataset. As a result, a multiple outputs ANN model that can predict 90 independent outputs at the same time is required. Therefore, the same mean squared loss of multiple output model used in Chapter 4 for the prediction of 6 independent, effective elastic properties of powder beds (Eq. 13) is used here for comparing the 90 outputs of the multiple output ANN regressor model and their corresponding 90 labeled data.

In order to achieve high accuracy and acceptable computational efficiency, the developed collision dataset was used to train several ANN architectures with multiple output regression layers using the proposed MSE loss function (Eq. 13) and adaptive moment estimation (Adam) optimizer.

The number of neurons in each hidden layer, the number of layers, arrangement of these layers, the type of activation function in neurons, batch size, and the learning rate are highly optimized to meet the demand of a highly accurate and efficient DL model. In a deep neural network, the most accurate results are observed when the number of neurons increases in each consecutive layer for the first couple of layers until the number of neurons in the hidden layer reaches a relatively high value, and then the number of neurons in the next following layers are reduced until the networks get to the output layer. The architecture of the highly optimized network developed in this fashion here is shown in the figure below.

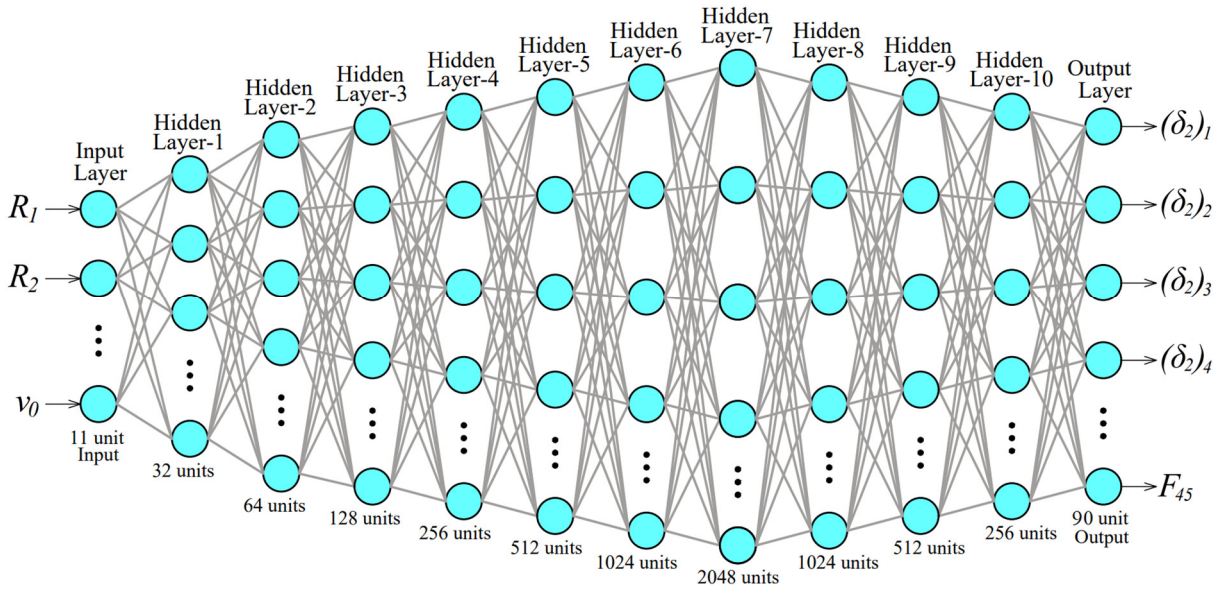

Figure 35: The proposed ANN architecture for the prediction of force-displacement behavior of the colliding body.

As shown in Figure 35, the proposed ANN with 10 hidden layers receives the 11 input data and outputs 90 numbers corresponding to 45 points on the compliance curve. The 11 input data includes pairs of the radi (R_1 and R_2), densities (ρ_1 and ρ_2), Young's modulus (E_1 and E_2), Yield stresses (Y_1 and Y_2), and Strain-hardening coefficients (n_1 and n_2) of both colliding bodies, as well as relative impact velocity (v_0). Starting with the first hidden layer (Hidden Layer-1), which

consists of 32 neurons, the number of neurons in the first seven hidden layers are doubled in every successive layer until it reaches 2048 neurons at the seventh hidden layer (Hidden Layer-7). For the following three hidden layers, the number of hidden neurons is halved in every consecutive layer until it reaches 256 neurons at the last hidden layer (Hidden Layer-10). In the proposed architecture, all layers are fully connected, meaning that neurons in every layer are connected to all neurons in their neighboring layers. After an empirical study of hyper-parameters, the ReLU activation function is chosen for all neurons to introduce some nonlinearity to the calculated weighted some of every input to the perceptron. The batch size and learning rate are set to 256 and 0.0005, respectively.

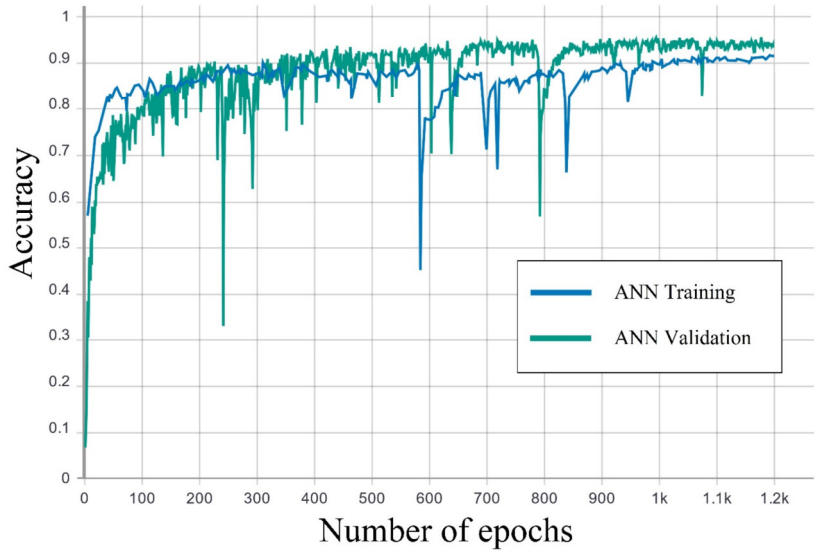

Figure 36: Training and validation accuracy vs. the number of epochs for the proposed ANN model.

The proposed ANN model is trained for 17.16 hours on 9,000 training examples and validated using 1,000 collision examples. Figure 36 shows the accuracy of the ANN model versus the number of passes of the entire training dataset through the ANN model during the training process (epochs). One can see from Figure 36 that after 1,000 epochs, both training and validation reach accuracies more than 90%. Furthermore, the best performance of the ANN model is observed

at 1,200th epoch where the training and validation accuracies have reached 91.51% and 94.27%, respectively. Evaluation of 100 randomly selected validation examples shows that it takes only 14.03 milliseconds for the proposed ANN model to predict the 45 force-displacement points on the compliance curve while it takes the physics-based simulation 6.75 seconds; hence on average, the ANN model is more than 480 times faster than the physics-based model.

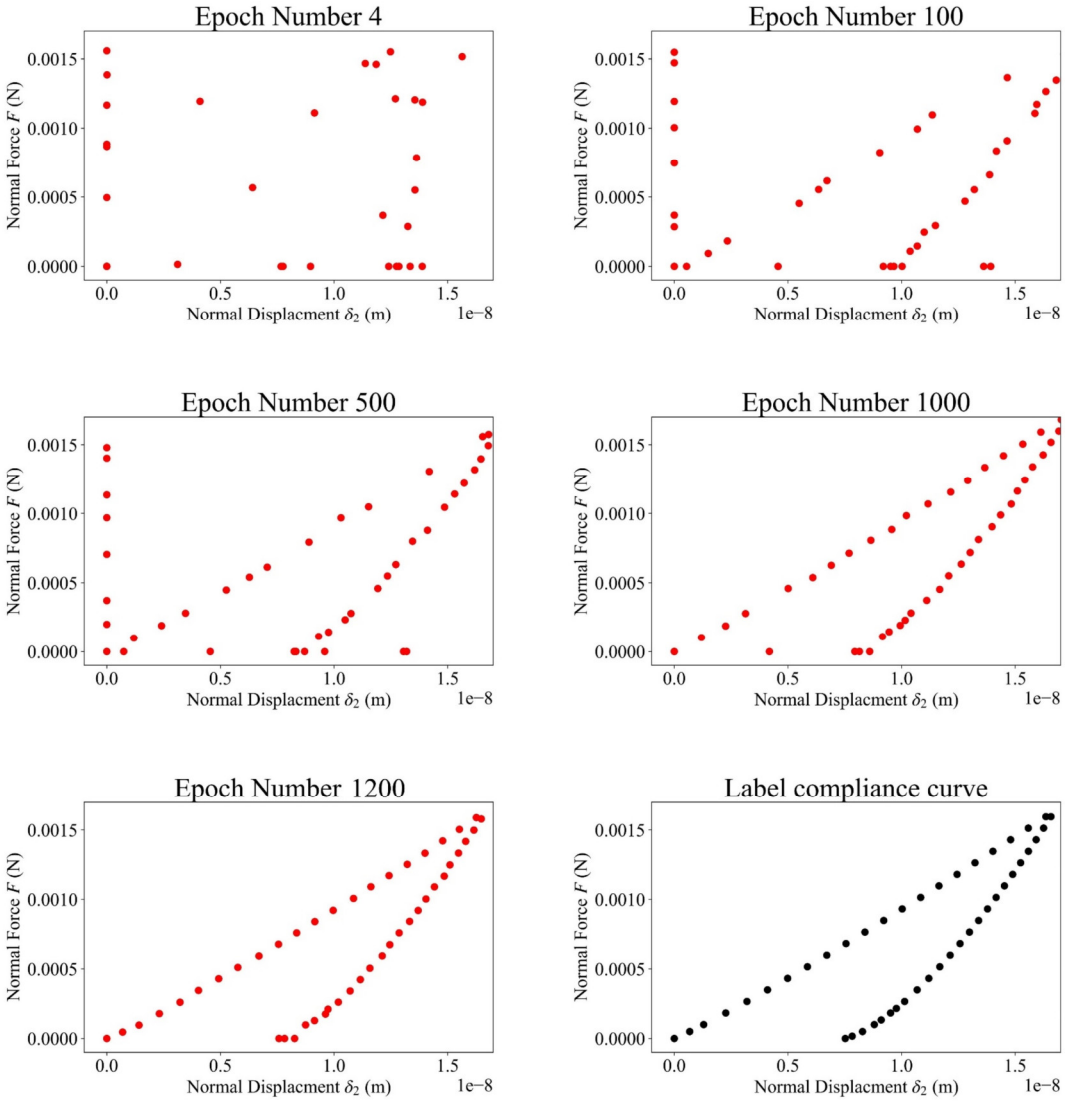

Figure 37: Evolution of the prediction of the collision compliance curve with the ANN model trained for the different number of epochs.

Figure 37 shows how effectively the proposed ANN model predicts the force-displacement behavior of Aluminum 5754-0 material body with the radius of 169 μm colliding against Tungsten material body with the radius of 195 μm with a relative impact velocity of 0.021 m/s. The ground truth label for this specific unseen example is shown in the bottom right compliance curve in Figure 37, with the other five compliance curves displaying the output of the ANN model trained for 4 to 1200 epochs.

5.4 Numerical Examples for the Evaluation of the Data-Driven Model of the Impact of Material Bodies

Multiple examples are shown in this section of the dissertation to demonstrate the accuracy and efficiency of the proposed ANN model for predicting the force-displacement behavior of dissimilar colliding material bodies in elastoplastic impact. As mentioned earlier, the results shown in this dissertation are the force-displacement behavior of the initially softer body; the same ANN model could be used to predict the force-displacement behavior of the initially harder body. Figure 38, Figure 39, and Figure 40 compare the 45 force-displacement points selected from physics-based simulation and their counterparts generated with the ANN model for three different collision cases of similar and dissimilar colliding bodies. The material and geometrical properties of both colliding bodies and their impact velocity for these three figures can be found in Table 5.

Table 5: Material and geometrical properties of 1st and 2nd colliding body as well as the relative impact velocity used to generate Figure 38, Figure 39, and Figure 40.

Figure number	Material of 1st body	Material of 2nd body	Radius of 1st body (μm)	Radius of 2nd body (μm)	v_0 (m/s)
Figure 38	Aluminum (5754-0)	Aluminum (5754-0)	259	99	0.1027
Figure 39	Aluminum (5754-0)	Polyethylene	134	98	0.1235
Figure 40	Tungsten	SK5 Steel (C = 0.87%)	126	99	0.0549

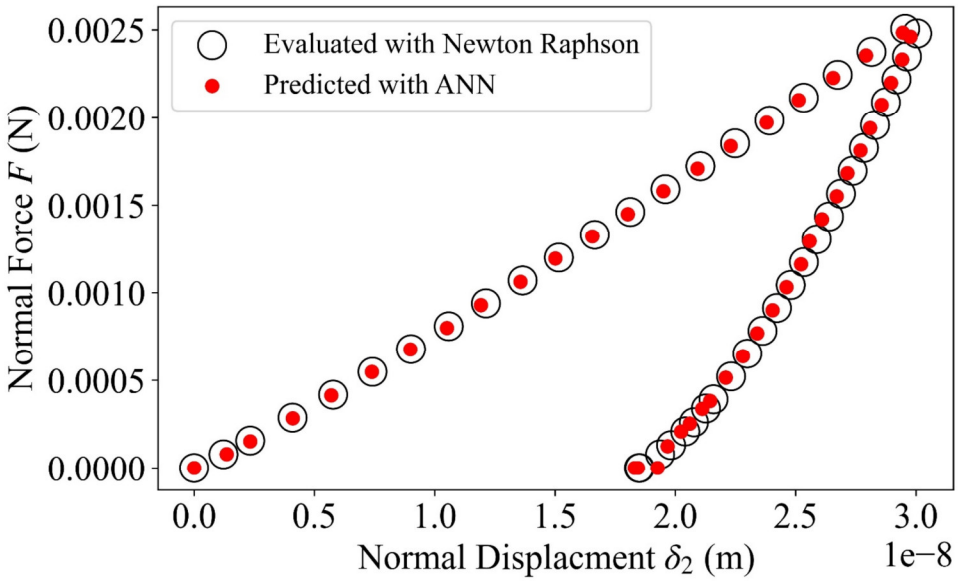

Figure 38: 45 points generated by the ANN model and 45 points selected from the compliance curve generated with lumped parameter model of the Aluminum (5754-0) body colliding against a body with the same material.

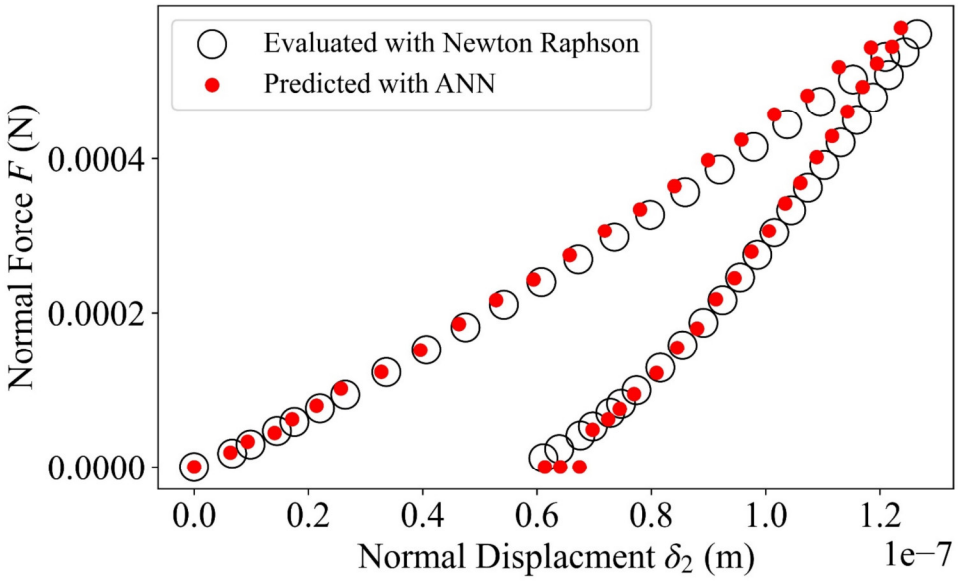

Figure 39: 45 points generated by the ANN model and 45 points selected from compliance curve generated with lumped parameter model of the polyethylene body colliding against an Aluminum (5754-0) body.

As shown in Figure 38, Figure 39, and Figure 40, the results generated by the proposed ANN model are almost identical to the results of physics-based simulation, which uses the

Newton-Raphson numerical method. One can see that the third point prior to the last data point generated by the ANN model in all figures has more error compared to other data points. It is worth mentioning that there are some repeating but not identical patterns of a small error in the indention and restitution phase of each generated plot. This means that, for instance, most of the points generated by ANN for the indentation phase of Figure 39 are shifted top left side of the ground-truth label, and most of the points generated by ANN for the restitution phase of the same figure are again shifted to the top left side of the ground-truth label. Connecting these points together results in a smooth plot which indicates the integrity of the ANN model.

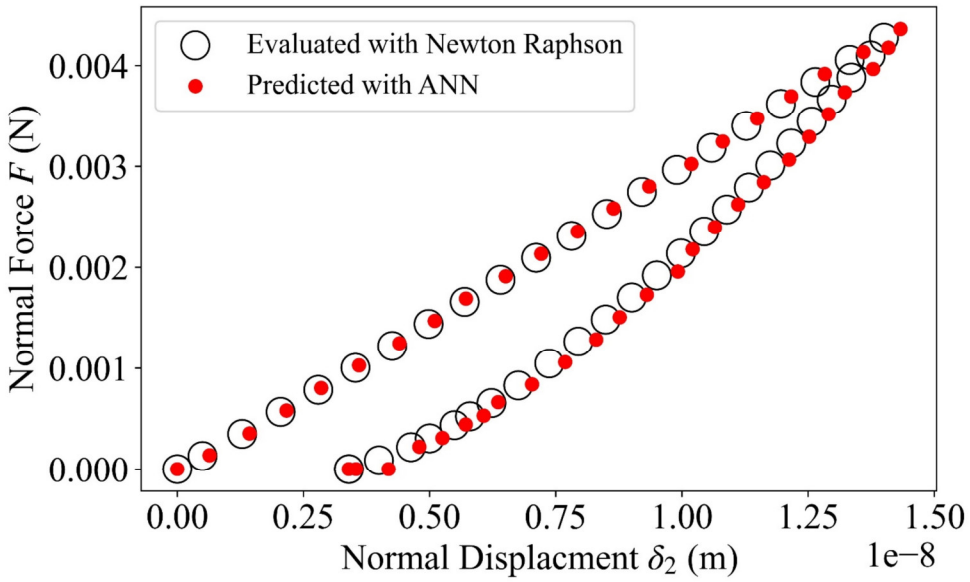

Figure 40: 45 points generated by the ANN model and 45 points selected from compliance curve generated with lumped parameter model of the SK5 Steel body colliding against Aluminum 5754-0 body.

For a better comparison of the plot generated with the physics-based model and the ANN results, the original force-displacement with a large number of points on the compliance curve is used to generate the ground-truth curve depicted in Figure 41. The scatter points generated with the ANN model are connected together in this figure to generate a curve for comparing the performance of the two models (the collision information can be found in the caption).

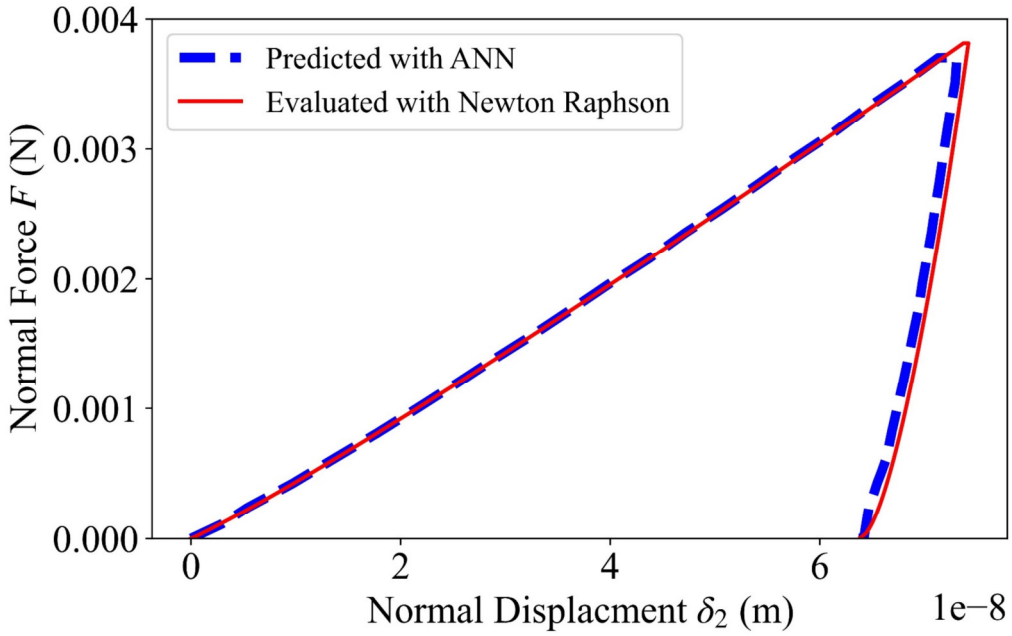

Figure 41: Compliance curve generated by the ANN and lumped parameter model of the Aluminum 1050 work hardened (initially softer body) with 204 μm radius colliding against a Tungsten body with 192 μm radius with 0.0589 m/s relative impact velocity.

Figure 42 illustrates the maximum indentation of the aluminum 1050 work-hardened with the radius of 250 μm colliding against B steel with the radius of 100 μm for various values of relative impact velocities. In order to evaluate the maximum indentation of the initially softer body versus relative impact velocity, the compliance curve has been generated 21 times for 21 incremental values of relative impact velocity between 0.05 m/s and 0.1 m/s using both piecewise nonlinear lumped parameter model as well as the developed ANN model.

Figure 43 compares the maximum contact force evaluated with the piecewise nonlinear lumped parameter model and the developed ANN model for various relative impact velocities for B steel and Tungsten colliding material bodies with 300 μm and 30 μm radius respectively. Again, the compliance curve has been generated 21 times for 21 incremental values of relative impact velocity between 0.05 m/s and 0.1 m/s using both methods.

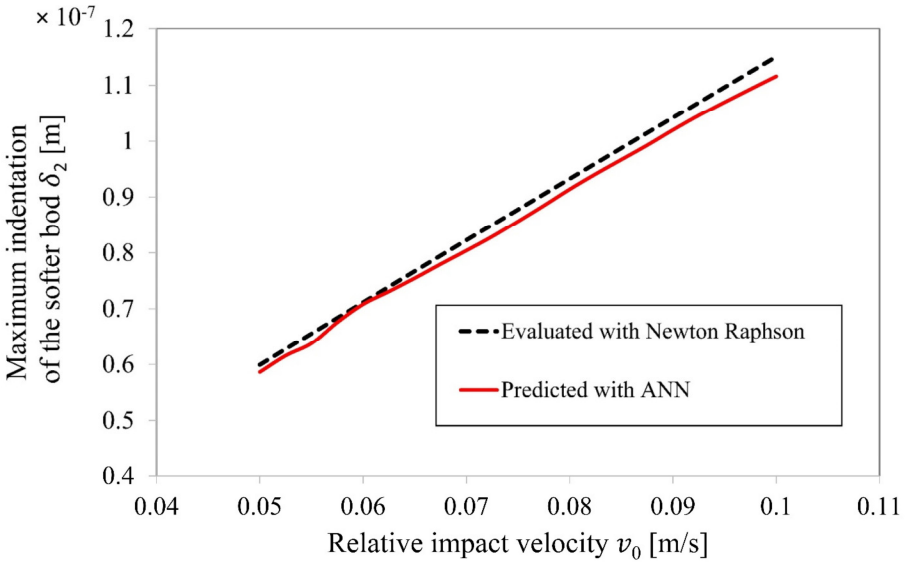

Figure 42: Maximum indentation of Aluminum 1050 work-hardened colliding against B steel versus relative impact velocity evaluated with the time-consuming Newton Raphson numerical method as well as the present DL model.

Despite the excellent agreement between the two methods, for evaluation of maximum indentation of the initially softer body in Figure 42 and maximum contact force between two colliding material bodies in Figure 43, the ANN model does not follow the perfect linear path of the lumped parameter model in these two figures.

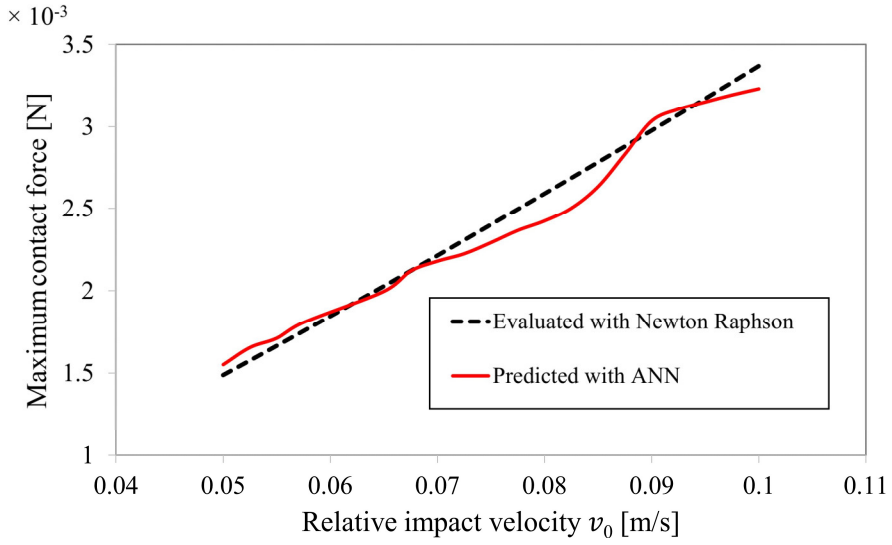

Figure 43: Maximum contact force between B steel and Tungsten colliding material bodies versus relative impact velocity evaluated with the time-consuming Newton Raphson numerical method as well as the present DL model.

Chapter 6. Conclusion and Future Works

The primary goal of this dissertation was to develop data-driven reduced-order models of the mechanical and thermomechanical interactions of material particles in powder-based AM processes and elastoplastic collision of strain-hardening material particles. The time-consuming physics-based numerical models of material particle interactions are employed to develop datasets, which are subsequently used to train DL models capable of lowering physics-based model computing time from several minutes to sub-second levels. The reduced-order models of the mechanical and thermomechanical interactions of material particles in the SLS manufacturing process have the potential to provide the basis for a real time process control system, and it can be used for AM process parameter optimization. Furthermore, the developed DL models of strain-hardening material particles preserve the non-linear characteristic of the collision between two material particles while reducing the computational cost of granular flow simulation with a large number of particles at the same time.

The adaptive DEM physics-based model of the thermal field of the SLS manufactured structure developed by Gobal and Ravani is utilized in Chapter 3 of this dissertation to develop a dataset including thousands of pairs of image representations of the trajectory of the laser head and heat-maps of the AM structure. The generated dataset is used to train a novel deep encoder-decoder CNN model capable of reducing the computational time to less than 1/41,000th of the time required to run the adaptive DEM simulation. Furthermore, the developed deep encoder-decoder CNN model results have been verified by comparison with the physics-based model results, and an excellent agreement between the two methods has been observed for laser trajectory and manufacturing process parameters. The developed DL model for sub-second prediction of the heat-map of powder-based AM structure may be expanded in the future to include AM structures with

several layers of powder particles, allowing researchers to investigate the intricate thermal interactions between layers and the degree of fusion between neighboring layers of powder particles. Moreover, the dataset and subsequently the DL model may further expand by considering the effect of the mean and standard deviation of the size of the powder particles, various pre-heating temperatures, and layer thickness on the heat-map of AM structure during the manufacturing process. The developed DL model may also be extended to applications such as fast prediction of the possible manufacturing defects like high residual stresses, out of plane distortion, and large porosity in the final product.

A fast and accurate DL approach for determining aggregate elastic properties of powder beds in the SLS manufacturing process is presented in this dissertation. The average discrepancy in predicted effective elastic properties between the proposed CNN regression model and DEM simulation is less than 4% for powder-based AM structures. The proposed CNN model is significantly more efficient than physics-based simulations because it can predict effective elastic properties without constructing a massive stiffness matrix. The computational time of the CNN model is 0.0005% the time needed for solving the problem using DEM simulation. By concatenating the material characteristics to flattened layers of CNN architecture as additional neurons, a CNN model may theoretically be utilized for powder particles with different material properties.

Considering the high computational cost of numerical models for simulation of the elastoplastic collision of the material bodies in granular systems with a large number of particles, in this dissertation, an ANN model developed for sub-second prediction of force-displacement behavior of colliding bodies during nonlinear collision given the relative impact velocity as well as material and geometrical properties of both colliding bodies. On average, the DL model is more

than 480 times faster than the physics-based model. Furthermore, the difference between predicted normalized points on the compliance curve with the DL model and the conventional iterative model is less than 6% for different collision scenarios. The developed sub-second DL model of the elastoplastic collision of dissimilar bodies with strain-hardening material can provide a basis for fast simulation of granular systems. Therefore, collecting a new dataset from the resulting enhanced granular simulation would be faster and more convenient compared to the conventional numerical models. Subsequently, the enhanced simulation of the granular system itself can be used to train new data-driven models to investigate different aspects of a granular system with a large number of interacting particles. For instance, the resulting enhanced simulation can be used to train a DL model capable of predicting the velocity field of powder particles from their mass distribution and various other system control signals in pharmaceutical manufacturing processes.

References

[1] G. Fu, D. Z. Zhang, A. N. He, Z. Mao, and K. Zhang, "Finite Element Analysis of Interaction of Laser Beam with Material in Laser Metal Powder Bed Fusion Process," *Materials*, vol. 11, no. 5, Art. no. 5, May 2018, doi: 10.3390/ma11050765.

[2] P. Liu, X. Cui, J. Deng, S. Li, Z. Li, and L. Chen, "Investigation of thermal responses during metallic additive manufacturing using a 'Tri-Prism' finite element method," *International Journal of Thermal Sciences*, vol. 136, pp. 217–229, Feb. 2019, doi: 10.1016/j.ijthermalsci.2018.10.022.

[3] J. C. Steuben, A. P. Iliopoulos, and J. G. Michopoulos, "Discrete element modeling of particle-based additive manufacturing processes," *Computer Methods in Applied Mechanics and Engineering*, vol. 305, pp. 537–561, Jun. 2016, doi: 10.1016/j.cma.2016.02.023.

[4] A. Gobal and B. Ravani, "An Adaptive Discrete Element Method for Physical Modeling of the Selective Laser Sintering Process," *Applied Mechanics and Materials*, 2017. https://www.scientific.net/AMM.869.69 (accessed Dec. 16, 2019).

[5] W. J. Stronge, A. R. Sofi, and B. Ravani, "Computing the composite coefficient of restitution for inelastic impact of dissimilar bodies," *International Journal of Impact Engineering*, vol. 133, p. 103333, Nov. 2019, doi: 10.1016/j.ijimpeng.2019.103333.

[6] Z. Luo and Y. Zhao, "A survey of finite element analysis of temperature and thermal stress fields in powder bed fusion Additive Manufacturing," *Additive Manufacturing*, vol. 21, pp. 318–332, May 2018, doi: 10.1016/j.addma.2018.03.022.

[7] N. C. Levkulich, S. L. Semiatin, J. E. Gockel, J. R. Middendorf, A. T. DeWald, and N. W. Klingbeil, "The effect of process parameters on residual stress evolution and distortion in the laser powder bed fusion of Ti-6Al-4V," *Additive Manufacturing*, vol. 28, pp. 475–484, Aug.

2019, doi: 10.1016/j.addma.2019.05.015.

[8] N. Kumar, H. Kumar, and J. S. Khurmi, “Experimental Investigation of Process Parameters for Rapid Prototyping Technique (Selective Laser Sintering) to Enhance the Part Quality of Prototype by Taguchi Method,” *Procedia Technology*, vol. 23, pp. 352–360, Jan. 2016, doi: 10.1016/j.protcy.2016.03.037.

[9] J. C. Heigel and B. M. Lane, “MEASUREMENT OF THE MELT POOL LENGTH DURING SINGLE SCAN TRACKS IN A COMMERCIAL LASER POWDER BED FUSION PROCESS,” Jun. 2017, Accessed: Nov. 29, 2020. [Online]. Available: https://www.nist.gov/publications/measurement-melt-pool-length-during-single-scan-tracks-commercial-laser-powder-bed

[10] L. E. Criales, Y. M. Arısoy, B. Lane, S. Moylan, A. Donmez, and T. Özel, “Laser powder bed fusion of nickel alloy 625: Experimental investigations of effects of process parameters on melt pool size and shape with spatter analysis,” *International Journal of Machine Tools and Manufacture*, vol. 121, pp. 22–36, Oct. 2017, doi: 10.1016/j.ijmachtools.2017.03.004.

[11] Y. Yang, M. Allen, T. London, and V. Oancea, “Residual Strain Predictions for a Powder Bed Fusion Inconel 625 Single Cantilever Part,” *Integr Mater Manuf Innov*, vol. 8, no. 3, pp. 294–304, Sep. 2019, doi: 10.1007/s40192-019-00144-5.

[12] A. K. Singh and P. R. Srinivasa, “Response surface-based simulation modeling for selective laser sintering process,” *Rapid Prototyping Journal*, vol. 16, no. 6, pp. 441–449, Jan. 2010, doi: 10.1108/13552541011083362.

[13] Y. Yang, O. Ragnvaldsen, Y. Bai, M. Yi, and B.-X. Xu, “Three-dimensional non-isothermal phase-field modeling of microstructure evolution during selective laser sintering,” Feb. 2019, doi: 10.1038/s41524-019-0219-7.

[14] E. J. R. Parteli and T. Pöschel, “Particle-based simulation of powder application in additive manufacturing,” *Powder Technology*, vol. 288, pp. 96–102, Jan. 2016, doi: 10.1016/j.powtec.2015.10.035.

[15] J. G. Michopoulos, A. P. Iliopoulos, J. C. Steuben, A. J. Birnbaum, and S. G. Lambrakos, “On the multiphysics modeling challenges for metal additive manufacturing processes,” *Additive Manufacturing*, vol. 22, pp. 784–799, Aug. 2018, doi: 10.1016/j.addma.2018.06.019.

[16] L. Xin, M. Boutaous, S. Xin, and D. A. Siginer, “Numerical modeling of the heating phase of the selective laser sintering process,” *International Journal of Thermal Sciences*, vol. 120, pp. 50–62, Oct. 2017, doi: 10.1016/j.ijthermalsci.2017.05.017.

[17] S. Haeri, Y. Wang, O. Ghita, and J. Sun, “Discrete element simulation and experimental study of powder spreading process in additive manufacturing,” *Powder Technology*, vol. 306, pp. 45–54, Jan. 2017, doi: 10.1016/j.powtec.2016.11.002.

[18] A. Gobal and B. Ravani, “Physical Modeling for Selective Laser Sintering Process,” *J. Comput. Inf. Sci. Eng*, vol. 17, no. 2, Jun. 2017, doi: 10.1115/1.4034473.

[19] W. Gao, Y. Tan, and M. Zang, “A cubic arranged spherical discrete element model,” *Int. J. Comput. Methods*, vol. 11, no. 05, p. 1350102, Mar. 2014, doi: 10.1142/S0219876213501028.

[20] J. Wang, Y. Ma, L. Zhang, R. X. Gao, and D. Wu, “Deep learning for smart manufacturing: Methods and applications,” *Journal of Manufacturing Systems*, vol. 48, pp. 144–156, Jul. 2018, doi: 10.1016/j.jmsy.2018.01.003.

[21] G. D. Goh, S. L. Sing, and W. Y. Yeong, “A review on machine learning in 3D printing: applications, potential, and challenges,” *Artif Intell Rev*, Jul. 2020, doi: 10.1007/s10462-020-09876-9.

[22] B. Zhang, S. Liu, and Y. C. Shin, “In-Process monitoring of porosity during laser additive

manufacturing process," *Additive Manufacturing*, vol. 28, pp. 497–505, Aug. 2019, doi: 10.1016/j.addma.2019.05.030.

[23] L. Scime, D. Siddel, S. Baird, and V. Paquit, "Layer-wise anomaly detection and classification for powder bed additive manufacturing processes: A machine-agnostic algorithm for real-time pixel-wise semantic segmentation," *Additive Manufacturing*, vol. 36, p. 101453, Dec. 2020, doi: 10.1016/j.addma.2020.101453.

[24] B. Yuan, B. Giera, G. Guss, I. Matthews, and S. Mcmains, "Semi-Supervised Convolutional Neural Networks for In-Situ Video Monitoring of Selective Laser Melting," in *2019 IEEE Winter Conference on Applications of Computer Vision (WACV)*, Jan. 2019, pp. 744–753. doi: 10.1109/WACV.2019.00084.

[25] L. Scime and J. Beuth, "A multi-scale convolutional neural network for autonomous anomaly detection and classification in a laser powder bed fusion additive manufacturing process," *Additive Manufacturing*, vol. 24, pp. 273–286, Dec. 2018, doi: 10.1016/j.addma.2018.09.034.

[26] M. Mozaffar *et al.*, "Data-driven prediction of the high-dimensional thermal history in directed energy deposition processes via recurrent neural networks," *Manufacturing Letters*, vol. 18, pp. 35–39, Oct. 2018, doi: 10.1016/j.mfglet.2018.10.002.

[27] A. Paul *et al.*, "A real-time iterative machine learning approach for temperature profile prediction in additive manufacturing processes," *arXiv:1907.12953 [cs, stat]*, Aug. 2019, Accessed: Dec. 22, 2019. [Online]. Available: http://arxiv.org/abs/1907.12953

[28] Y. Du and S. Wang, "Energy Dissipation in Normal Elastoplastic Impact Between Two Spheres," *J. Appl. Mech*, vol. 76, no. 6, Nov. 2009, doi: 10.1115/1.3130801.

[29] A. Big-Alabo, "Rigid Body Motions and Local Compliance Response during Impact of Two Deformable Spheres," *Mechanical Engineering Research*, vol. 8, no. 1, p. p1, Dec. 2017, doi:

10.5539/mer.v8n1p1.

[30] C. Wu, L. Li, and C. Thornton, "Rebound behaviour of spheres for plastic impacts," *International Journal of Impact Engineering*, vol. 28, no. 9, pp. 929–946, Oct. 2003, doi: 10.1016/S0734-743X(03)00014-9.

[31] S. D. Mesarovic and N. A. Fleck, "Frictionless indentation of dissimilar elastic–plastic spheres," *International Journal of Solids and Structures*, vol. 37, no. 46, pp. 7071–7091, Nov. 2000, doi: 10.1016/S0020-7683(99)00328-5.

[32] L. Vu-Quoc and X. Zhang, "An elastoplastic contact force–displacement model in the normal direction: displacement–driven version," *Proceedings of the Royal Society of London. Series A: Mathematical, Physical and Engineering Sciences*, vol. 455, no. 1991, pp. 4013–4044, Nov. 1999, doi: 10.1098/rspa.1999.0488.

[33] L. Vu-Quoc, X. Zhang, and L. Lesburg, "A Normal Force-Displacement Model for Contacting Spheres Accounting for Plastic Deformation: Force-Driven Formulation," *J. Appl. Mech*, vol. 67, no. 2, pp. 363–371, Jun. 2000, doi: 10.1115/1.1305334.

[34] A. Big-Alabo, "Equivalent impact system approach for elastoplastic impact analysis of dissimilar spheres," *International Journal of Impact Engineering*, vol. 113, pp. 168–179, Mar. 2018, doi: 10.1016/j.ijimpeng.2017.11.021.

[35] K. H. Hunt and F. R. E. Crossley, "Coefficient of Restitution Interpreted as Damping in Vibroimpact," *Journal of Applied Mechanics*, vol. 42, no. 2, pp. 440–445, Jun. 1975, doi: 10.1115/1.3423596.

[36] W. J. Stronge, A. R. Sofi, and B. Ravani, "Computing the composite coefficient of restitution for inelastic impact of dissimilar bodies," *International Journal of Impact Engineering*, vol. 133, p. 103333, Nov. 2019, doi: 10.1016/j.ijimpeng.2019.103333.

[37] C. Thornton, S. J. Cummins, and P. W. Cleary, “An investigation of the comparative behaviour of alternative contact force models during inelastic collisions,” *Powder Technology*, vol. 233, pp. 30–46, Jan. 2013, doi: 10.1016/j.powtec.2012.08.012.

[38] J. Coaplen, W. J. Stronge, and B. Ravani, “Work equivalent composite coefficient of restitution,” *International Journal of Impact Engineering*, vol. 30, no. 6, pp. 581–591, Jul. 2004, doi: 10.1016/j.ijimpeng.2003.10.038.

[39] W. J. Stronge and B. Ravani, “‘Work equivalent composite coefficient of restitution.’ Int. J. Impact Engineering 30(6), 581–592, 2004: Reply to comment: ‘Work equivalent composite coefficient of restitution’ by Akuro Big-Alabo,” *International Journal of Impact Engineering*, vol. 95, pp. 176–177, Sep. 2016, doi: 10.1016/j.ijimpeng.2016.02.002.

[40] F. J. Montáns, F. Chinesta, R. Gómez-Bombarelli, and J. N. Kutz, “Data-driven modeling and learning in science and engineering,” *Comptes Rendus Mécanique*, vol. 347, no. 11, pp. 845–855, Nov. 2019, doi: 10.1016/j.crme.2019.11.009.

[41] G. X. Gu, C.-T. Chen, D. J. Richmond, and M. J. Buehler, “Bioinspired hierarchical composite design using machine learning: simulation, additive manufacturing, and experiment,” *Mater. Horiz.*, vol. 5, no. 5, pp. 939–945, Aug. 2018, doi: 10.1039/C8MH00653A.

[42] E. Haghighat, M. Raissi, A. Moure, H. Gomez, and R. Juanes, “A deep learning framework for solution and discovery in solid mechanics,” *arXiv:2003.02751 [cs, stat]*, May 2020, Accessed: Mar. 09, 2021. [Online]. Available: http://arxiv.org/abs/2003.02751

[43] N. Dawson-Elli, S. B. Lee, M. Pathak, K. Mitra, and V. R. Subramanian, “Data Science Approaches for Electrochemical Engineers: An Introduction through Surrogate Model Development for Lithium-Ion Batteries,” *J. Electrochem. Soc.*, vol. 165, no. 2, pp. A1–A15,

2018, doi: 10.1149/2.1391714jes.

[44] M. Kang and N. J. Jameson, “Machine Learning: Fundamentals,” in *Prognostics and Health Management of Electronics*, John Wiley & Sons, Ltd, 2018, pp. 85–109. doi: 10.1002/9781119515326.ch4.

[45] P. Cunningham, M. Cord, and S. J. Delany, “Supervised Learning,” in *Machine Learning Techniques for Multimedia: Case Studies on Organization and Retrieval*, M. Cord and P. Cunningham, Eds. Berlin, Heidelberg: Springer, 2008, pp. 21–49. doi: 10.1007/978-3-540-75171-7_2.

[46] F. Jiang, Z. Guan, Z. Li, and X. Wang, “A method of predicting visual detectability of low-velocity impact damage in composite structures based on logistic regression model,” *Chinese Journal of Aeronautics*, vol. 34, no. 1, pp. 296–308, Jan. 2021, doi: 10.1016/j.cja.2020.10.006.

[47] I. Baturynska, “Statistical analysis of dimensional accuracy in additive manufacturing considering STL model properties,” *Int J Adv Manuf Technol*, vol. 97, no. 5, pp. 2835–2849, Jul. 2018, doi: 10.1007/s00170-018-2117-4.

[48] I. Baturynska and K. Martinsen, “Prediction of geometry deviations in additive manufactured parts: comparison of linear regression with machine learning algorithms,” *J Intell Manuf*, vol. 32, no. 1, pp. 179–200, Jan. 2021, doi: 10.1007/s10845-020-01567-0.

[49] S. Muthukrishnan, H. Krishnaswamy, S. Thanikodi, D. Sundaresan, and V. Venkatraman, “Support vector machine for modelling and simulation of heat exchangers,” *Thermal Science*, vol. 24, no. 1 Part B, pp. 499–503, 2020.

[50] K. Aoyagi, H. Wang, H. Sudo, and A. Chiba, “Simple method to construct process maps for additive manufacturing using a support vector machine,” *Additive Manufacturing*, vol. 27, pp. 353–362, May 2019, doi: 10.1016/j.addma.2019.03.013.

[51] D. Heckerman, “A Tutorial on Learning With Bayesian Networks,” *arXiv:2002.00269 [cs, stat]*, Mar. 2021, Accessed: Apr. 01, 2021. [Online]. Available: http://arxiv.org/abs/2002.00269

[52] M. Correa, C. Bielza, M. de J. Ramirez, and J. R. Alique, “A Bayesian network model for surface roughness prediction in the machining process,” *International Journal of Systems Science*, vol. 39, no. 12, pp. 1181–1192, Dec. 2008, doi: 10.1080/00207720802344683.

[53] C. S. Tucker and H. M. Kim, “Data-Driven Decision Tree Classification for Product Portfolio Design Optimization,” *Journal of Computing and Information Science in Engineering*, vol. 9, no. 041004, Nov. 2009, doi: 10.1115/1.3243634.

[54] L. Breiman, “Random Forests,” *Machine Learning*, vol. 45, no. 1, pp. 5–32, Oct. 2001, doi: 10.1023/A:1010933404324.

[55] S. K. Dasari, A. Cheddad, and P. Andersson, “Random Forest Surrogate Models to Support Design Space Exploration in Aerospace Use-Case,” in *Artificial Intelligence Applications and Innovations*, Cham, 2019, pp. 532–544. doi: 10.1007/978-3-030-19823-7_45.

[56] D. Wu, Y. Wei, and J. Terpenny, “Surface Roughness Prediction in Additive Manufacturing Using Machine Learning,” presented at the ASME 2018 13th International Manufacturing Science and Engineering Conference, Sep. 2018. doi: 10.1115/MSEC2018-6501.

[57] L. Shi, S. T. K. Lin, Y. Lu, L. Ye, and Y. X. Zhang, “Artificial neural network based mechanical and electrical property prediction of engineered cementitious composites,” *Construction and Building Materials*, vol. 174, pp. 667–674, Jun. 2018, doi: 10.1016/j.conbuildmat.2018.04.127.

[58] S. Chowdhury and S. Anand, “Artificial Neural Network Based Geometric Compensation for Thermal Deformation in Additive Manufacturing Processes,” presented at the ASME 2016

11th International Manufacturing Science and Engineering Conference, Sep. 2016. doi: 10.1115/MSEC2016-8784.

[59] Y. LeCun *et al.*, "Backpropagation Applied to Handwritten Zip Code Recognition," *Neural Computation*, vol. 1, no. 4, pp. 541–551, Dec. 1989, doi: 10.1162/neco.1989.1.4.541.

[60] Y. LeCun, P. Haffner, L. Bottou, and Y. Bengio, "Object Recognition with Gradient-Based Learning," in *Shape, Contour and Grouping in Computer Vision*, D. A. Forsyth, J. L. Mundy, V. di Gesú, and R. Cipolla, Eds. Berlin, Heidelberg: Springer, 1999, pp. 319–345. doi: 10.1007/3-540-46805-6_19.

[61] Y. Wei, Q. Tian, J. Guo, W. Huang, and J. Cao, "Multi-vehicle detection algorithm through combining Harr and HOG features," *Mathematics and Computers in Simulation*, vol. 155, pp. 130–145, Jan. 2019, doi: 10.1016/j.matcom.2017.12.011.

[62] W. M. Thu and D. W. T. Tun, "GLCM and LTP Based Classification of Food Types," *International Journal of Science and Engineering Applications*, vol. 7, no. 08, p. 5, 2018.

[63] J. Yoo, H. Eom, and Y. S. Choi, "Image-To-Image Translation Using a Cross-Domain Auto-Encoder and Decoder," *Applied Sciences*, vol. 9, no. 22, Art. no. 22, Jan. 2019, doi: 10.3390/app9224780.

[64] M. C. Messner, "Convolutional Neural Network Surrogate Models for the Mechanical Properties of Periodic Structures," *Journal of Mechanical Design*, vol. 142, no. 024503, Oct. 2019, doi: 10.1115/1.4045040.

[65] K. Chen, S. Pashami, Y. Fan, and S. Nowaczyk, "Predicting Air Compressor Failures Using Long Short Term Memory Networks," in *Progress in Artificial Intelligence*, Cham, 2019, pp. 596–609. doi: 10.1007/978-3-030-30241-2_50.

[66] L. Wu, V. D. Nguyen, N. G. Kilingar, and L. Noels, "A recurrent neural network-accelerated

multi-scale model for elasto-plastic heterogeneous materials subjected to random cyclic and non-proportional loading paths," *Computer Methods in Applied Mechanics and Engineering*, vol. 369, p. 113234, Sep. 2020, doi: 10.1016/j.cma.2020.113234.

[67] M. E. Celebi and K. Aydin, *Unsupervised Learning Algorithms*. Springer, 2016.

[68] B. C. Patel and G. Sinha, "An Adaptive K-means Clustering Algorithm for Breast Image Segmentation," 2010, doi: 10.5120/1467-1982.

[69] S. P. Donegan, E. J. Schwalbach, and M. A. Groeber, "Zoning additive manufacturing process histories using unsupervised machine learning," *Materials Characterization*, vol. 161, p. 110123, Mar. 2020, doi: 10.1016/j.matchar.2020.110123.

[70] R. Sabbagh and F. Ameri, "A Framework Based on K-Means Clustering and Topic Modeling for Analyzing Unstructured Manufacturing Capability Data," *Journal of Computing and Information Science in Engineering*, vol. 20, no. 011005, Sep. 2019, doi: 10.1115/1.4044506.

[71] M. Khanzadeh, P. Rao, R. Jafari-Marandi, B. K. Smith, M. A. Tschopp, and L. Bian, "Quantifying Geometric Accuracy With Unsupervised Machine Learning: Using Self-Organizing Map on Fused Filament Fabrication Additive Manufacturing Parts," *Journal of Manufacturing Science and Engineering*, vol. 140, no. 031011, Dec. 2017, doi: 10.1115/1.4038598.

[72] M. Ringnér, "What is principal component analysis?," *Nature Biotechnology*, vol. 26, no. 3, Art. no. 3, Mar. 2008, doi: 10.1038/nbt0308-303.

[73] C. Xu, S. Gao, and M. Li, "Heterogeneous Material Design Using a PCA-Based Microstructure Representing Method," presented at the ASME 2015 International Design Engineering Technical Conferences and Computers and Information in Engineering Conference, Jan. 2016. doi: 10.1115/DETC2015-46955.

[74] S. Hong and M.-H. H. Shen, “A Novel Online Structure Damage Identification Using Principal Component Analysis (PCA),” Apr. 2009, pp. 367–374. doi: 10.1115/POWER2007-22198.

[75] H. Heidari and A. Ohadi, “Fault Detection in Gearbox With Non-Stationary Rotational Speed Using CWT Feature Extraction, PCA Reduction and ANN Classifier Methods,” Sep. 2013, pp. 193–199. doi: 10.1115/DETC2012-71271.

[76] A. Fischer and C. Igel, “An Introduction to Restricted Boltzmann Machines,” in *Progress in Pattern Recognition, Image Analysis, Computer Vision, and Applications*, Berlin, Heidelberg, 2012, pp. 14–36. doi: 10.1007/978-3-642-33275-3_2.

[77] D. Ye, J. Y. Hsi Fuh, Y. Zhang, G. S. Hong, and K. Zhu, “In situ monitoring of selective laser melting using plume and spatter signatures by deep belief networks,” *ISA Transactions*, vol. 81, pp. 96–104, Oct. 2018, doi: 10.1016/j.isatra.2018.07.021.

[78] X. He, D. Wang, Y. Li, and C. Zhou, “A Novel Bearing Fault Diagnosis Method Based on Gaussian Restricted Boltzmann Machine,” *Mathematical Problems in Engineering*, vol. 2016, p. e2957083, Dec. 2016, doi: 10.1155/2016/2957083.

[79] T. Kohonen, “The self-organizing map,” *Proceedings of the IEEE*, vol. 78, no. 9, pp. 1464–1480, Sep. 1990, doi: 10.1109/5.58325.

[80] Z. Gan *et al.*, “Data-Driven Microstructure and Microhardness Design in Additive Manufacturing Using a Self-Organizing Map,” *Engineering*, vol. 5, no. 4, pp. 730–735, Aug. 2019, doi: 10.1016/j.eng.2019.03.014.

[81] R. Huang, L. Xi, X. Li, C. Richard Liu, H. Qiu, and J. Lee, “Residual life predictions for ball bearings based on self-organizing map and back propagation neural network methods,” *Mechanical Systems and Signal Processing*, vol. 21, no. 1, pp. 193–207, Jan. 2007, doi:

10.1016/j.ymssp.2005.11.008.

[82] X. Zhu and A. B. Goldberg, “Introduction to Semi-Supervised Learning,” *Synthesis Lectures on Artificial Intelligence and Machine Learning*, vol. 3, no. 1, pp. 1–130, Jan. 2009, doi: 10.2200/S00196ED1V01Y200906AIM006.

[83] X. Zhou and M. Belkin, “Chapter 22 - Semi-Supervised Learning,” in *Academic Press Library in Signal Processing*, vol. 1, P. S. R. Diniz, J. A. K. Suykens, R. Chellappa, and S. Theodoridis, Eds. Elsevier, 2014, pp. 1239–1269. doi: 10.1016/B978-0-12-396502-8.00022-X.

[84] “Semi-supervised deep learning based framework for assessing manufacturability of cellular structures in direct metal laser sintering process | SpringerLink.” https://link.springer.com/article/10.1007/s10845-020-01575-0 (accessed Apr. 29, 2021).

[85] D. B. Verstraete, E. L. Droguett, V. Meruane, M. Modarres, and A. Ferrada, “Deep semi-supervised generative adversarial fault diagnostics of rolling element bearings,” *Structural Health Monitoring*, vol. 19, no. 2, pp. 390–411, Mar. 2020, doi: 10.1177/1475921719850576.

[86] K. Guo and M. J. Buehler, “A semi-supervised approach to architected materials design using graph neural networks,” *Extreme Mechanics Letters*, vol. 41, p. 101029, Nov. 2020, doi: 10.1016/j.eml.2020.101029.

[87] I. A. Okaro, S. Jayasinghe, C. Sutcliffe, K. Black, P. Paoletti, and P. L. Green, “Automatic fault detection for laser powder-bed fusion using semi-supervised machine learning,” *Additive Manufacturing*, vol. 27, pp. 42–53, May 2019, doi: 10.1016/j.addma.2019.01.006.

[88] Y. Li, “Deep Reinforcement Learning: An Overview,” *arXiv:1701.07274 [cs]*, Nov. 2018, Accessed: May 10, 2021. [Online]. Available: http://arxiv.org/abs/1701.07274

[89] M. Wiering and M. van Otterlo, *Reinforcement Learning: State-of-the-Art*. Springer Science

& Business Media, 2012.

[90] K. Guo, Z. Yang, C.-H. Yu, and M. J. Buehler, “Artificial intelligence and machine learning in design of mechanical materials,” *Mater. Horiz.*, vol. 8, no. 4, pp. 1153–1172, Apr. 2021, doi: 10.1039/D0MH01451F.

[91] M. Mozaffar, A. Ebrahimi, and J. Cao, “Toolpath design for additive manufacturing using deep reinforcement learning,” *arXiv:2009.14365 [cs]*, Sep. 2020, Accessed: May 12, 2021. [Online]. Available: http://arxiv.org/abs/2009.14365

[92] T. Yang *et al.*, “A soft artificial muscle driven robot with reinforcement learning,” *Scientific Reports*, vol. 8, no. 1, Art. no. 1, Sep. 2018, doi: 10.1038/s41598-018-32757-9.

[93] H. Lu, Y. Li, S. Mu, D. Wang, H. Kim, and S. Serikawa, “Motor Anomaly Detection for Unmanned Aerial Vehicles Using Reinforcement Learning,” *IEEE Internet of Things Journal*, vol. 5, no. 4, pp. 2315–2322, Aug. 2018, doi: 10.1109/JIOT.2017.2737479.

[94] X. Y. Lee, A. Balu, D. Stoecklein, B. Ganapathysubramanian, and S. Sarkar, “A Case Study of Deep Reinforcement Learning for Engineering Design: Application to Microfluidic Devices for Flow Sculpting,” *Journal of Mechanical Design*, vol. 141, no. 111401, Sep. 2019, doi: 10.1115/1.4044397.

[95] A. Hussein, M. M. Gaber, E. Elyan, and C. Jayne, “Imitation Learning: A Survey of Learning Methods,” *ACM Comput. Surv.*, vol. 50, no. 2, p. 21:1-21:35, Apr. 2017, doi: 10.1145/3054912.

[96] P. Owan, J. Garbini, and S. Devasia, “Faster Confined Space Manufacturing Teleoperation Through Dynamic Autonomy With Task Dynamics Imitation Learning,” *IEEE Robotics and Automation Letters*, vol. 5, no. 2, pp. 2357–2364, Apr. 2020, doi: 10.1109/LRA.2020.2970653.

[97] J. S. Arora and G. Baenziger, “Uses of artificial intelligence in design optimization,” *Computer Methods in Applied Mechanics and Engineering*, vol. 54, no. 3, pp. 303–323, Mar. 1986, doi: 10.1016/0045-7825(86)90108-8.

[98] M. Fuge, B. Peters, and A. Agogino, “Machine Learning Algorithms for Recommending Design Methods,” *Journal of Mechanical Design*, vol. 136, no. 101103, Aug. 2014, doi: 10.1115/1.4028102.

[99] A. Raina, C. McComb, and J. Cagan, “Learning to Design From Humans: Imitating Human Designers Through Deep Learning,” *Journal of Mechanical Design*, vol. 141, no. 111102, Sep. 2019, doi: 10.1115/1.4044256.

[100] X. Yao, S. K. Moon, and G. Bi, “A hybrid machine learning approach for additive manufacturing design feature recommendation,” *Rapid Prototyping Journal*, vol. 23, no. 6, pp. 983–997, Jan. 2017, doi: 10.1108/RPJ-03-2016-0041.

[101] E. Westphal and H. Seitz, “A machine learning method for defect detection and visualization in selective laser sintering based on convolutional neural networks,” *Additive Manufacturing*, vol. 41, p. 101965, May 2021, doi: 10.1016/j.addma.2021.101965.

[102] B. N. Narayanan, K. Beigh, S. Duning, and D. Erdahl, “Automated material identification and segmentation using deep learning for laser powder bed fusion,” in *Applications of Machine Learning 2020*, Aug. 2020, vol. 11511, p. 115110P. doi: 10.1117/12.2567007.

[103] C. Gobert, E. W. Reutzel, J. Petrich, A. R. Nassar, and S. Phoha, “Application of supervised machine learning for defect detection during metallic powder bed fusion additive manufacturing using high resolution imaging.,” *Additive Manufacturing*, vol. 21, pp. 517–528, May 2018, doi: 10.1016/j.addma.2018.04.005.

[104] D. Weimer, B. Scholz-Reiter, and M. Shpitalni, “Design of deep convolutional neural network architectures for automated feature extraction in industrial inspection,” *CIRP Annals*, vol. 65, no. 1, pp. 417–420, Jan. 2016, doi: 10.1016/j.cirp.2016.04.072.

[105] D. Ye, G. S. Hong, Y. Zhang, K. Zhu, and J. Y. H. Fuh, “Defect detection in selective laser melting technology by acoustic signals with deep belief networks,” *Int J Adv Manuf Technol*, vol. 96, no. 5, pp. 2791–2801, May 2018, doi: 10.1007/s00170-018-1728-0.

[106] M. Grasso, F. Gallina, and B. M. Colosimo, “Data fusion methods for statistical process monitoring and quality characterization in metal additive manufacturing,” *Procedia CIRP*, vol. 75, pp. 103–107, Jan. 2018, doi: 10.1016/j.procir.2018.04.045.

[107] S. Koziel and A. Pietrenko-Dabrowska, *Performance-Driven Surrogate Modeling of High-Frequency Structures*. Springer Nature, 2020.

[108] E. Stathatos and G.-C. Vosniakos, “Real-time simulation for long paths in laser-based additive manufacturing: a machine learning approach,” *Int J Adv Manuf Technol*, vol. 104, no. 5, pp. 1967–1984, Oct. 2019, doi: 10.1007/s00170-019-04004-6.

[109] R. Dupuis, J.-C. Jouhaud, and P. Sagaut, “Surrogate Modeling of Aerodynamic Simulations for Multiple Operating Conditions Using Machine Learning,” *AIAA Journal*, vol. 56, no. 9, pp. 3622–3635, 2018, doi: 10.2514/1.J056405.

[110] S. Changyu, W. Lixia, and L. Qian, “Optimization of injection molding process parameters using combination of artificial neural network and genetic algorithm method,” *Journal of Materials Processing Technology*, vol. 183, no. 2, pp. 412–418, Mar. 2007, doi: 10.1016/j.jmatprotec.2006.10.036.

[111] W. Rong-Ji, L. Xin-hua, W. Qing-ding, and W. Lingling, “Optimizing process parameters for selective laser sintering based on neural network and genetic algorithm,” *Int*

J Adv Manuf Technol, vol. 42, no. 11, pp. 1035–1042, Jun. 2009, doi: 10.1007/s00170-008-1669-0.

[112] W. Sukthomya and J. D. T. Tannock, "Taguchi experimental design for manufacturing process optimisation using historical data and a neural network process model," *International Journal of Quality & Reliability Management*, vol. 22, no. 5, pp. 485–502, Jan. 2005, doi: 10.1108/02656710510598393.

[113] J. Zhu, H. Zhou, C. Wang, L. Zhou, S. Yuan, and W. Zhang, "A review of topology optimization for additive manufacturing: Status and challenges," *Chinese Journal of Aeronautics*, vol. 34, no. 1, pp. 91–110, Jan. 2021, doi: 10.1016/j.cja.2020.09.020.

[114] H. Chi *et al.*, "Universal machine learning for topology optimization," *Computer Methods in Applied Mechanics and Engineering*, vol. 375, p. 112739, Mar. 2021, doi: 10.1016/j.cma.2019.112739.

[115] I. Sosnovik and I. Oseledets, "Neural networks for topology optimization," *arXiv:1709.09578 [cs, math]*, Sep. 2017, Accessed: May 17, 2021. [Online]. Available: http://arxiv.org/abs/1709.09578

[116] Y. Yu, T. Hur, and J. Jaeho, "Deep learning for topology optimization design," *Korea Advanced Atomic Research Institute*, [Online]. Available: https://arxiv.org/pdf/1801.05463.pdf

[117] J. P. Kruth, X. Wang, T. Laoui, and L. Froyen, "Lasers and materials in selective laser sintering," *Assembly Automation*, vol. 23, no. 4, pp. 357–371, Jan. 2003, doi: 10.1108/01445150310698652.

[118] D. T. Pham, S. Dimov, and F. Lacan, "Selective laser sintering: Applications and technological capabilities," *Proceedings of the Institution of Mechanical Engineers, Part B:*

Journal of Engineering Manufacture, vol. 213, no. 5, pp. 435–449, May 1999, doi: 10.1243/0954405991516912.

[119] A. Nazarov, I. Skornyakov, and I. Shishkovsky, "The Setup Design for Selective Laser Sintering of High-Temperature Polymer Materials with the Alignment Control System of Layer Deposition," *Machines*, vol. 6, no. 1, Art. no. 1, Mar. 2018, doi: 10.3390/machines6010011.

[120] G. Li, X. He, W. Zhang, H. Chang, L. Dong, and L. Lin, "Non-locally Enhanced Encoder-Decoder Network for Single Image De-raining," *arXiv:1808.01491 [cs]*, Aug. 2018, Accessed: Dec. 31, 2020. [Online]. Available: http://arxiv.org/abs/1808.01491

[121] I. D. Mastan and S. Raman, "Multi-level Encoder-Decoder Architectures for Image Restoration," *arXiv:1905.00322 [cs, eess]*, May 2019, Accessed: Dec. 31, 2020. [Online]. Available: http://arxiv.org/abs/1905.00322

[122] Z. Chi, X. Wu, X. Shu, and J. Gu, "Single Image Reflection Removal Using Deep Encoder-Decoder Network," *arXiv:1802.00094 [cs]*, Jan. 2018, Accessed: Dec. 31, 2020. [Online]. Available: http://arxiv.org/abs/1802.00094

[123] J. Brownlee, *Deep Learning for Computer Vision: Image Classification, Object Detection, and Face Recognition in Python*. Machine Learning Mastery, 2019.

[124] H. Lee and H. Kwon, "Going Deeper With Contextual CNN for Hyperspectral Image Classification," *IEEE Transactions on Image Processing*, vol. 26, no. 10, pp. 4843–4855, Oct. 2017, doi: 10.1109/TIP.2017.2725580.

[125] H. Ide and T. Kurita, "Improvement of learning for CNN with ReLU activation by sparse regularization," in *2017 International Joint Conference on Neural Networks (IJCNN)*, May 2017, pp. 2684–2691. doi: 10.1109/IJCNN.2017.7966185.

[126] H. Das, C. Pradhan, and N. Dey, *Deep Learning for Data Analytics: Foundations, Biomedical Applications, and Challenges*. Academic Press, 2020.

[127] D. Kim and D. Hwang, *Intelligent Imaging and Analysis*. MDPI, 2020.

[128] K. Somandepalli, A. Toutios, and S. S. Narayanan, "Semantic Edge Detection for Tracking Vocal Tract Air-Tissue Boundaries in Real-Time Magnetic Resonance Images," in *Interspeech 2017*, Aug. 2017, pp. 631–635. doi: 10.21437/Interspeech.2017-1580.

[129] G. James, D. Witten, T. Hastie, and R. Tibshirani, *An Introduction to Statistical Learning: with Applications in R*. Springer Science & Business Media, 2013.

[130] D. J. Corbin, A. R. Nassar, E. W. Reutzel, A. M. Beese, and P. Michaleris, "Effect of Substrate Thickness and Preheating on the Distortion of Laser Deposited Ti–6Al–4V," *Journal of Manufacturing Science and Engineering*, vol. 140, no. 061009, Mar. 2018, doi: 10.1115/1.4038890.

[131] "Microstructure simulations of Inconel 718 during selective laser melting using a phase field model | SpringerLink." https://link.springer.com/article/10.1007/s00170-018-2814-z (accessed Jan. 10, 2021).

[132] J. Romano, L. Ladani, and M. Sadowski, "Laser Additive Melting and Solidification of Inconel 718: Finite Element Simulation and Experiment," *JOM*, vol. 68, no. 3, pp. 967–977, Mar. 2016, doi: 10.1007/s11837-015-1765-1.

[133] D. A. Lesyk, S. Martinez, B. N. Mordyuk, V. V. Dzhemelinskyi, A. Lamikiz, and G. I. Prokopenko, "Post-processing of the Inconel 718 alloy parts fabricated by selective laser melting: Effects of mechanical surface treatments on surface topography, porosity, hardness and residual stress," *Surface and Coatings Technology*, vol. 381, p. 125136, Jan. 2020, doi: 10.1016/j.surfcoat.2019.125136.

[134] S. Y. Liu, H. Q. Li, C. X. Qin, R. Zong, and X. Y. Fang, "The effect of energy density on texture and mechanical anisotropy in selective laser melted Inconel 718," *Materials & Design*, vol. 191, p. 108642, Jun. 2020, doi: 10.1016/j.matdes.2020.108642.

[135] "Supersolidus Liquid Phase Sintering Modeling of Inconel 718 Superalloy | SpringerLink." https://link.springer.com/article/10.1007/s11661-015-3244-2 (accessed Jan. 10, 2021).

[136] E. A. Clark, R. Yeske, and H. K. Birnbaum, "The effect of hydrogen on the surface energy of nickel," *Metall Mater Trans A*, vol. 11, no. 11, pp. 1903–1908, Nov. 1980, doi: 10.1007/BF02655107.

[137] A. Gobal, "An Adaptive Discrete Element Method for Physical Modeling of the Selective Laser Sintering Process," UC Davis, 2017.

[138] X. Liu, C. L. Martin, G. Delette, and D. Bouvard, "Elasticity and strength of partially sintered ceramics," *Journal of the Mechanics and Physics of Solids*, vol. 58, no. 6, pp. 829–842, Jun. 2010, doi: 10.1016/j.jmps.2010.04.007.

[139] K. Bagi, "Stress and strain in granular assemblies," *Mechanics of Materials*, vol. 22, no. 3, pp. 165–177, Mar. 1996, doi: 10.1016/0167-6636(95)00044-5.

[140] K. Bagi, "Microstructural Stress Tensor of Granular Assemblies With Volume Forces," *J. Appl. Mech*, vol. 66, no. 4, pp. 934–936, Dec. 1999, doi: 10.1115/1.2791800.

[141] X. Liu and V. Shapiro, "Homogenization of material properties in additively manufactured structures," *Computer-Aided Design*, vol. 78, pp. 71–82, Sep. 2016, doi: 10.1016/j.cad.2016.05.017.

[142] C.-L. Zhang, J.-H. Luo, X.-S. Wei, and J. Wu, "In Defense of Fully Connected Layers in Visual Representation Transfer," in *Advances in Multimedia Information Processing* –

PCM 2017, Cham, 2018, pp. 807–817. doi: 10.1007/978-3-319-77383-4_79.

[143] A. Krizhevsky, I. Sutskever, and G. E. Hinton, "ImageNet Classification with Deep Convolutional Neural Networks," in *Advances in Neural Information Processing Systems 25*, F. Pereira, C. J. C. Burges, L. Bottou, and K. Q. Weinberger, Eds. Curran Associates, Inc., 2012, pp. 1097–1105. Accessed: Jun. 03, 2020. [Online]. Available: http://papers.nips.cc/paper/4824-imagenet-classification-with-deep-convolutional-neural-networks.pdf

[144] Y. Lecun, L. Bottou, Y. Bengio, and P. Haffner, "Gradient-based learning applied to document recognition," *Proceedings of the IEEE*, vol. 86, no. 11, pp. 2278–2324, Nov. 1998, doi: 10.1109/5.726791.

[145] K. Simonyan and A. Zisserman, "Very Deep Convolutional Networks for Large-Scale Image Recognition," *arXiv:1409.1556 [cs]*, Apr. 2015, Accessed: Jun. 04, 2020. [Online]. Available: http://arxiv.org/abs/1409.1556

[146] R. Singh, R. Rana, and S. K. Singh, "Performance Evaluation of VGG models in Detection of Wheat Rust," 2018. /paper/Performance-Evaluation-of-VGG-models-in-Detection-Singh-Rana/01c8aa86f8d424f52b92efd1870caa5061bf7d64 (accessed Jun. 05, 2020).

[147] S. B. Yeom, E.-S. Ha, M.-S. Kim, S. H. Jeong, S.-J. Hwang, and D. H. Choi, "Application of the Discrete Element Method for Manufacturing Process Simulation in the Pharmaceutical Industry," *Pharmaceutics*, vol. 11, no. 8, Art. no. 8, Aug. 2019, doi: 10.3390/pharmaceutics11080414.

[148] B. K. Mishra and C. V. R. Murty, "On the determination of contact parameters for realistic DEM simulations of ball mills," *Powder Technology*, vol. 115, no. 3, pp. 290–297,

Apr. 2001, doi: 10.1016/S0032-5910(00)00347-8.

[149] "An accurate and efficient tangential force–displacement model for elastic frictional contact in particle-flow simulations," *EDEM Simulation*. https://www.edemsimulation.com/papers/an-accurate-and-efficient-tangential-force-displacement-model-for-elastic-frictional-contact-in-particle-flow-simulations/ (accessed Jun. 04, 2021).

[150] L. Vu-Quoc and X. Zhang, "An elastoplastic contact force–displacement model in the normal direction: displacement–driven version," *Proceedings of the Royal Society of London. Series A: Mathematical, Physical and Engineering Sciences*, vol. 455, no. 1991, pp. 4013–4044, Nov. 1999, doi: 10.1098/rspa.1999.0488.

[151] L.-Y. Li, C.-Y. Wu, and C. Thornton, "A theoretical model for the contact of elastoplastic bodies," *Proceedings of the Institution of Mechanical Engineers, Part C: Journal of Mechanical Engineering Science*, vol. 216, no. 4, pp. 421–431, Apr. 2001, doi: 10.1243/0954406021525214.

[152] C. Thornton, "Coefficient of Restitution for Collinear Collisions of Elastic-Perfectly Plastic Spheres," *J. Appl. Mech*, vol. 64, no. 2, pp. 383–386, Jun. 1997, doi: 10.1115/1.2787319.

[153] A. Di Renzo and F. P. Di Maio, "Comparison of contact-force models for the simulation of collisions in DEM-based granular flow codes," *Chemical Engineering Science*, vol. 59, no. 3, pp. 525–541, Feb. 2004, doi: 10.1016/j.ces.2003.09.037.

[154] M. Boos and J. McPhee, "Volumetric Contact Dynamics Models and Experimental Validation of Normal Forces for Simple Geometries," Jun. 2012, pp. 275–284. doi: 10.1115/DETC2011-49016.

[155] K. L. Johnson and K. L. Johnson, *Contact Mechanics*. Cambridge University Press, 1987.

[156] R. Hill, B. Storåkers, and A. B. Zdunek, "A theoretical study of the Brinell hardness test," *Proceedings of the Royal Society of London. A. Mathematical and Physical Sciences*, vol. 423, no. 1865, pp. 301–330, Jun. 1989, doi: 10.1098/rspa.1989.0056.

[157] B. Storåkers, N. A. . Fleck, and R. M. McMeeking, "The viscoplastic compaction of composite powders," *Journal of the Mechanics and Physics of Solids*, vol. 47, no. 4, pp. 785–815, Feb. 1999, doi: 10.1016/S0022-5096(98)00076-3.

[158] M. R. Brake, "An analytical elastic-perfectly plastic contact model," *International Journal of Solids and Structures*, vol. 49, no. 22, pp. 3129–3141, Nov. 2012, doi: 10.1016/j.ijsolstr.2012.06.013.

[159] W. J. Stronge, A. R. Sofi, and B. Ravani, "Computing the composite coefficient of restitution for inelastic impact of dissimilar bodies," *International Journal of Impact Engineering*, vol. 133, p. 103333, Nov. 2019, doi: 10.1016/j.ijimpeng.2019.103333.

[160] J. Won, S. Kim, O. M. Kwon, Y.-C. Kim, and D. Kwon, "Evaluation of tensile yield strength of high-density polyethylene in flat-ended cylindrical indentation: An analytic approach based on the expanding cavity model," *Journal of Materials Research*, vol. 35, no. 2, pp. 206–214, Jan. 2020, doi: 10.1557/jmr.2019.387.

[161] R. Khelif, A. Chateauneuf, and K. Chaoui, "Statistical analysis of HDPE fatigue lifetime," *Meccanica*, vol. 43, no. 6, pp. 567–576, Dec. 2008, doi: 10.1007/s11012-008-9133-7.

[162] C. Gabriel and H. Münstedt, "Strain hardening of various polyolefins in uniaxial elongational flow," *Journal of Rheology*, vol. 47, no. 3, pp. 619–630, May 2003, doi: 10.1122/1.1567752.